

Precise FWER Control for Gaussian Related Fields: Riding the SuRF to continuous land - Part 1

Fabian J.E. Telschow¹, Samuel Davenport²

¹Department of Mathematics, Humboldt Universität zu Berlin

²Division of Biostatistics, University of California, San Diego

April 17, 2024

Abstract

The Gaussian Kinematic Formula (GKF) is a powerful and computationally efficient tool to perform statistical inference on random fields and became a well-established tool in the analysis of neuroimaging data. Using realistic error models, [Eklund et al. \[2016\]](#) recently showed that GKF based methods for *voxelwise inference* lead to conservative control of the familywise error rate (FWER) and to inflated false positive rates for cluster-size inference. In this series of articles we identify and resolve the main causes of these shortcomings in the traditional usage of the GKF for voxelwise inference. In particular applications of Random Field Theory have depended on the *good lattice assumption*, which is only reasonable when the data is sufficiently smooth. We address this here, allowing for valid inference under arbitrary applied smoothness and non-stationarity, for Gaussian and Gaussian related fields. We address the assumption of Gaussianity in Part 2, where we also demonstrate that our GKF based methodology is non-conservative under realistic error models.

1 Introduction

In experiments in neuroscience using functional Magnetic Resonance Imaging (fMRI) of the brain, data consists of 3D-images representing the time dynamics of the blood-oxygen-level dependence (BOLD). After an extensive pre-processing pipeline, including corrections for head motion and respiratory effects the time-series for each subject is combined into subject level maps (3D-images, typically consisting of coefficients of a linear model) via a first-level analysis step, see e.g., [Poldrack and Nichols \[2011\]](#) and the references therein. These high resolution images contain hundreds of thousands of voxels and allow for the detection of the locations of differences in %BOLD in the brain across different tasks and subjects. A major practical challenge, however, is the low signal-to-noise ratio which is often increased by convolving each subject level map with a smoothing kernel, typically an isotropic 3D-Gaussian kernel with Full Width at Half Maximum (FWHM) $\approx 4-8$ mm, i.e., $\approx 2-4$ voxels, [[Eklund et al., 2016](#), Supplementary material]. A standard statistical analysis to identify areas of activation in the brain is the mass-univariate approach which combines hypotheses tests at each voxel of a test statistic image \tilde{T} obtained from the smoothed subject level maps with a multiple testing procedure. A practical solution to the multiple testing of the thousands of voxels in the brain in terms of controlling the *family-wise error rate* (FWER) was pioneered in [Worsley et al. \[1992\]](#), [Friston et al. \[1994\]](#), [Worsley et al. \[1996\]](#) and is known as *Random Field Theory* (RFT) in the neuroimaging community. The key innovation was to use the *Gaussian Kinematic Formula*

(GKF) (e.g., Taylor [2006]) to approximate the probability that the maximum of a Gaussian random field with C^3 sample paths over a compact Whitney stratified (WS) manifold $\mathcal{M} \subset \mathbb{R}^D$, $D \in \mathbb{N}$, exceeds a given threshold. The accuracy of this approximation has been theoretically studied in [Taylor et al., 2005]. We refer to the setting from these papers, where \mathcal{M} can be either the brain or its surface, as *traditional RFT*. Originally assuming stationarity of the data, traditional RFT became a standard tool in the analysis of fMRI data, Worsley et al. [1996], because of its low computational costs. In the late 1990s it was the core inference methodology in standard software such as *Statistical Parametric Mapping*, [Friston et al.] and it is still the backbone of cluster-size and peak inference Friston et al. [1994], Chumbley and Friston [2009], Schwartzman and Telschow [2019]. However, in the early 2000s it was shown in Monte-Carlo-simulations that RFT for voxel-wise inference is very conservative [Nichols and Hayasaka, 2003], especially at the levels of applied smoothing used in applications. Therefore it has been superseded by time costly, yet accurate permutation tests, among others, [Nichols and Holmes, 2002, Winkler et al., 2016a,b]. Using resting state data combined with fake task designs the seminal article Eklund et al. [2016] showed that voxelwise RFT inference is conservative (see their Figure 1) which confirms the findings of [Nichols and Hayasaka, 2003] on a realistic data model. They also showed that cluster-size inference based on RFT can have inflated false positive rates. They argued that – in addition to the lack of smoothness– a lack of stationarity in real data is another major cause of their findings. Although these factors play a role in the conservativeness of voxel-wise inference using RFT we identify in this article and in Part 2 - Davenport et al. [2023] - the true causes and present an elegant solution. Here we assume that the data is Gaussian, while Part 2 generalizes our approach to non-Gaussian data and validates its performance using a large resting-state dataset from the UK Biobank [Alfaro-Almagro et al., 2018].

Traditional RFT assumes that an underlying continuous random field is approximated well by the random field observed on the voxel lattice, compare [Nichols and Hayasaka, 2003, p.430]. More precisely, it assumes $\max_{v \in \mathcal{V}} \tilde{T}(v) \approx \max_{s \in \mathcal{M}} \tilde{T}(s)$. We call this the *good lattice assumption* which was expressed, albeit less clearly, earlier in [Worsley et al., 1996]: “[...] the search region was regarded as a region with a smooth boundary defined at every point in 3-D. In practice only voxel data are available, and this will be regarded as a continuous image sampled on a lattice of equally spaced points. Thus a voxel is treated as a point in 3-D with zero volume, although it is often displayed on computer screens and in publications as a volume centered at that point.” As we shall argue, this view does not carefully distinguish between the *data* and the *atoms of a probabilistic model*.

(Raw) data is the information about nature which is extracted from measurement devices and is without exception currently discrete. In contrast, the atoms (or data objects¹) of probabilistic models used to describe data and perform statistical inference are functions, curves, images, shapes, trees or other mathematical objects [Wang and Marron, 2007, Marron and Alonso, 2014]. In our neuroimaging example, the data consists of the subject level maps obtained from the first level model observed on a discrete set \mathcal{V} of voxels which “belong” to the brain.² In traditional RFT the test statistic \tilde{T} used for inference is a random field over \mathcal{V} obtained from the smoothed data, while the atoms of RFT are random fields with twice differentiable sample paths over the brain, i.e., a Whitney stratified (WS) manifold \mathcal{M} . Historically, the good lattice assumption hides this mismatch between the data and the atoms of RFT. To

¹We favor the term atoms over data objects because this nomenclature better separates the two concepts.

²This is not “raw” data as it is the result of a pre-processing pipeline and some statistical modeling. It is another topic that complexity of today’s data often makes statistical modeling starting with raw data infeasible. But consistency along the data analysis pipeline should be guaranteed as much as feasible.

be independent of the good lattice assumption, Worsley [2005] and Taylor et al. [2007] propose voxel based methods under the (unrealistic) model that the data consists of a signal plus stationary Gaussian noise which has a separable covariance structure.

In this article we resolve the inconsistency between the data and the atoms of traditional RFT differently. Our key observation is that the smoothing operation which is used to increase the signal-to-noise ratio in the preprocessing naturally transforms the subject level maps (the data), into functions over a WS manifold $\mathcal{M} \supset \mathcal{V}$ (atoms of RFT). Thus, the test statistic \tilde{T} can be interpreted as a function over \mathcal{M} , too. This allows us to solve the two main problems of the good lattice assumption, i.e.,

- (i) $\max_{v \in \mathcal{V}} \tilde{T}(v) \leq \max_{s \in \mathcal{M}} \tilde{T}(s)$ for all $\mathcal{V} \subset \mathcal{M}$
- (ii) continuous quantities, e.g., derivatives, are replaced by voxel-based, discrete counterparts.

In particular, (i) is at the core of the conservativeness in traditional RFT as it implies

$$\mathbb{P}\left(\max_{v \in \mathcal{V}} \tilde{T}(v) > u_\alpha\right) \leq \mathbb{P}\left(\max_{x \in \mathcal{M}} \tilde{T}(x) > u_\alpha\right) \approx \alpha \quad (1)$$

for $u_\alpha \in \mathbb{R}$ being the α level threshold obtained from the GKF.

In order to resolve (i) and (ii) we interpret the smoothing step from pre-processing as transforming the data into functions over a WS manifold \mathcal{M} , i.e., atoms of RFT. More precisely, given an observed Gaussian random field X (“a subject level map” aka data) over a finite set $\mathcal{V} \subset \mathbb{R}^D$, $D \in \mathbb{N}$, a compact, D -dimensional WS manifold \mathcal{M} and a smoothing kernel function $K : \mathcal{V} \times \mathcal{M} \rightarrow \mathbb{R}$, we define the random field \tilde{X} (“a smoothed subject level map” aka atom of RFT) given by $\tilde{X}(s) = \sum_{v \in \mathcal{V}} X(v)K(v, s)$, $s \in \mathcal{M}$. We call \tilde{X} a *Super Resolution Field* (SuRF) since – given data X – it can be evaluated at any $s \in \mathcal{M}$. As many path properties of SuRFs are inherited from K , we shall show in Theorem 1 that the GKF holds for \tilde{T} (“a statistic depending on smoothed subject level maps” aka built from atoms of RFT) under mild conditions on K and X .

In order to perform inference using the GKF we must specify the domain \mathcal{M} . The latter has not been properly defined in the neuroimaging literature so far because of the reliance on the good lattice assumption. This leads to a further mismatch between theory and practice in traditional RFT as the GKF is not valid for random fields over discrete sets. We choose \mathcal{M} to be the *voxel manifold* $\mathcal{M}_{\mathcal{V}}$ which we define to be a disjoint union of D -dimensional hyperrectangles aligned with the coordinate axes and centered at the elements of \mathcal{V} . This is a natural way to define a D -dimensional WS manifold from \mathcal{V} , see Figure 6 in the supplementary material. The main benefit of using $\mathcal{M}_{\mathcal{V}}$ is that it simplifies the estimation of the Lipschitz Killing Curvatures (LKC) – the unknown parameters in the GKF. Moreover, the statistic $\max_{s \in \mathcal{M}_{\mathcal{V}}} \tilde{T}(s)$ can be well approximated using numerical optimizers, which allows us to resolve problem (i), the dominant factor in the observed conservativeness.

SuRFs also allow us to address problem (ii). In current software packages the LKCs are estimated from the random fields evaluated on \mathcal{V} assuming the good lattice assumption and stationarity (Forman et al. [1995], [Kiebel et al., 1999], Worsley et al. [1996]). These approaches use discrete approximations of the derivatives of \tilde{X} instead of the available true derivatives. Less widely used estimators drop the restrictive assumption of stationarity but still rely on discrete approximation of derivatives, these are the warping estimator [Taylor and Worsley, 2007], and the Hermite projection estimator (HPE) [Telschow et al., 2023].³ In Section 3.5 we propose

³In theory the HPE does not depend on discrete derivatives. However the HPE does requires the critical values of residual fields and the current implementation of it uses discrete derivatives to do so.

a consistent LKC estimator based on the explicitly available derivatives of a SuRF, which is computational fast as it requires only a minimal resolution increase to obtain accurate estimates of the LKCs in practice.

Inherent in any method that applies smoothing is that the resulting inference will only provide strong control of the FWER with respect to the smoothed signal. Since smoothing is regularly used in neuroimaging this affects a wide range of methods⁴. Widely cited articles such as [Nichols and Hayasaka \[2003\]](#) talk about FWER control in the strong sense but this is implicitly with respect to the smooth signal. In order to clarify this issue, we show in [Section 3.6](#) that kernel smoothing results in a FWER control which lies in between weak and strong control. In particular localization of a significant signal on the level of data is limited by the support of the kernel.

The article is structured as follows. In [Section 2](#) we define the notation. [Section 3](#) studies theoretical properties of SuRFs. In particular, [Section 3.6](#) explains in detail how voxelwise inference based on the GKF using SuRFs is carried out and provides an explanation of the type of the resulting FWER control. In [Section 4](#) we verify our findings using a simulation study. In particular, [Section 4.2](#) reports the results of the SuRF LKC estimates under different models and compares them to other published LKC estimators. Simulations which demonstrate that the SuRF framework avoids the conservativeness of traditional voxelwise RFT inference can be found in [Section 4.3](#). In [Section 5](#) we discuss our findings and review other potential applications of SuRFs. A Matlab implementation of the SuRF methodology is available in the RFTtoolbox [[Davenport and Telschow, 2023](#)]. Scripts reproducing our simulation results are available at <https://github.com/ftelschow/ConvolutionFieldsTheory>.

2 Notation and Definitions

In this section, we establish notation used in the article. We assume that $v \in \mathbb{R}^D$ is a column vector, i.e., we identify \mathbb{R}^D with $\mathbb{R}^{D \times 1}$. With \mathcal{M} we denote a D -dimensional, compact \mathcal{C}^2 -Whitney-stratified (WS) manifold isometrically embedded into a D -dimensional manifold $\overline{\mathcal{M}}$ without boundary. Recall that a WS manifold of dimension D is a space $\mathcal{M} = \bigcup_{d=1}^D \partial_d \mathcal{M}$ decomposed into strata where the stratum $\partial_d \mathcal{M} \subset \overline{\mathcal{M}}$ is a manifold of dimension d and all the strata are disjoint, i.e., $\partial_d \mathcal{M} \cap \partial_{d'} \mathcal{M} = \emptyset$ for all $d \neq d'$, compare [[Adler and Taylor, 2009](#), Chapter 8] for more details. A \mathcal{C}^2 -chart (which gives local \mathcal{C}^2 -coordinates) around $s \in \overline{\mathcal{M}}$ is given by a tuple $(\overline{U}, \overline{\phi})$ where $\overline{U} \subset \overline{\mathcal{M}}$ open, $s \in \overline{U}$ and $\overline{\phi} \in \mathcal{C}^2(\overline{U}, \overline{V})$ is a diffeomorphism onto an open set $\overline{V} \subset \mathbb{R}^D$. By the compactness of \mathcal{M} there exists a set of finitely many charts $(\overline{U}_\alpha, \overline{\phi}_\alpha)_{\alpha \in \{1, \dots, P\}}$ of \mathcal{M} , $P \in \mathbb{N}$, such that $\mathcal{M} \subset \bigcup_{\alpha=1}^P \overline{U}_\alpha$. This union is the only relevant part of $\overline{\mathcal{M}}$ since we are only interested in properties of \mathcal{M} . The surrounding manifold $\overline{\mathcal{M}}$ is only introduced for technical requirements in the formulation of the GKF.

We denote with $f_\alpha = f \circ \overline{\phi}_\alpha^{-1}$ the coordinate representation of f in the chart U_α and with ∇f_α the gradient of f_α , i.e., $\nabla f_\alpha(x) = \left(\frac{\partial f_\alpha}{\partial x_1}(x), \dots, \frac{\partial f_\alpha}{\partial x_D}(x) \right) \in \mathbb{R}^{1 \times D}$ for $x \in V_\alpha$, and with $\nabla^2 f_\alpha$ the Hessian of f_α , i.e., $\nabla^2 f_\alpha(x) \in \mathbb{R}^{D \times D}$ is the matrix with d - d' th entry $\frac{\partial^2 f_\alpha}{\partial x_d \partial x_{d'}}(x)$ for $x \in V_\alpha$. If the gradient ∇ or the Hessian ∇^2 is applied to a function with two arguments, then it is always assumed to be with respect to the first argument. We will use s, s' for points in \mathcal{M} or $\overline{\mathcal{M}}$ and x, y for points in local coordinates. For simplicity in notation, given $h \in C^1(\mathbb{R}^D)$

⁴Compare for example [[Lazar, 2008](#), e.g., pp.48-49] for detailed explanations why data analysis in neuroimage requires smoothing.

and a multi-index $\beta \in \mathbb{N}^d$, $d \leq D$, we write

$$\partial_\beta h(x) = \frac{\partial^d h(x)}{\partial x_{\beta_1}, \dots, \partial x_{\beta_d}}(x), \quad x \in \mathbb{R}^D. \quad (2)$$

If $h \in C^1(\mathbb{R}^D \times \mathbb{R}^D)$, we sometimes write $(\partial_\beta^x h)(x, y)$ for $(\partial_\beta h(\cdot, y))(x)$ evaluated at $(x, y) \in \mathbb{R}^D \times \mathbb{R}^D$. Note that "∂" also appears in our notation for the strata of a WS manifold. For a symmetric matrix $A \in \mathbb{R}^{D \times D}$, $D \in \mathbb{N}$, we define its *half-vectorization* as $\mathbb{V}(A) = (A_{11}, \dots, A_{D1}, A_{22}, \dots, A_{D2}, \dots, A_{D-1D-1}, A_{DD-1}, A_{DD})$ and the set $a \cdot \mathbb{Z}^D = \{x \in \mathbb{R}^D \mid x = (a_1 z_1, \dots, a_D z_D), z \in \mathbb{Z}^D\}$ for $D \in \mathbb{N}$ and any vector $a \in \mathbb{R}^D$ which has positive entries. We also assume throughout the article that \mathcal{V} is a finite, discrete set.

3 Theory

In this section we define Super-Resolution Fields (SuRFs), introduce some of their basic properties and show that they satisfy the Gaussian kinematic formula (GKF) under mild conditions. Moreover, we derive computable estimators of the Lipschitz Killing curvatures (LKC) of a SuRF defined over a voxel manifolds even if the data is non-stationary.

3.1 Super-resolution Fields

Definition 1. We call a map $K : \overline{\mathcal{M}} \times \mathcal{V} \rightarrow \mathbb{R}$ a *kernel*. We say it is continuous/differentiable, if $s \mapsto K(s, v)$ is continuous/differentiable for all $v \in \mathcal{V}$.

Remark 1. This kernel definition is broader than the standard one in statistics, where it is typically a function $k : \overline{\mathcal{M}} \rightarrow \mathbb{R}$ with a normalization property. The function k can be viewed as a kernel from $\overline{\mathcal{M}} \times \overline{\mathcal{M}} \rightarrow \mathbb{R}$ by setting $K(s, s') = k(s - s')$.

Definition 2. Let X be a \mathbb{R} -valued random field on \mathcal{V} with covariance function $\mathfrak{c}(u, v) = \text{Cov}[X(u), X(v)]$, $u, v \in \mathcal{V}$. For a kernel $K : \overline{\mathcal{M}} \times \mathcal{V} \rightarrow \mathbb{R}$ the random field over $\overline{\mathcal{M}}$,

$$\tilde{X}(s) = \sum_{v \in \mathcal{V}} K(s, v) X(v), \quad s \in \overline{\mathcal{M}}, \quad (3)$$

is termed a *Super-Resolution Field* (SuRF) linked to K and \mathcal{V} . For brevity, we will refer to it as $(\tilde{X}, X, K, \mathcal{V})$ or simply \tilde{X} when the context is evident regarding X , K , and \mathcal{V} .

Given a SuRF $(\tilde{X}, X, K, \mathcal{V})$ we call $(\tilde{X}, X, \tilde{K}, \mathcal{V})$ a *normalized SuRF* if

$$\tilde{K} : \overline{\mathcal{M}} \times \mathcal{V} \rightarrow \mathbb{R}, \quad (s, v) \mapsto \frac{K(s, v)}{\sqrt{\sum_{u \in \mathcal{V}} \sum_{v \in \mathcal{V}} K(s, u) K(s, v) \mathfrak{c}(u, v)}}.$$

Remark 2. Let \tilde{X} be a SuRF linked to K and $\mathbb{E}[X(v)] < \infty$ for all $v \in \mathcal{V}$. Then by linearity

$$\mathbb{E}[\tilde{X}(s)] = \sum_{v \in \mathcal{V}} K(s, v) \mathbb{E}[X(v)], \quad s \in \overline{\mathcal{M}}, \quad (4)$$

and if additionally $\mathbb{E}[X(v)^2] < \infty$ for all $v \in \mathcal{V}$ then

$$\text{Cov}[\tilde{X}(s), \tilde{X}(s')] = \sum_{u \in \mathcal{V}} \sum_{v \in \mathcal{V}} K(s, u) K(s', v) \mathfrak{c}(u, v) < \infty, \quad s, s' \in \overline{\mathcal{M}}. \quad (5)$$

The last formula explains the definition of the normalized SuRF, since it shows that any normalized SuRF satisfies $\text{Var}[\tilde{X}(s)] = 1$ for all $s \in \overline{\mathcal{M}}$.

Remark 3. Equation (5) is similar to an inner product, where $(\mathbf{c}(u, v))_{u, v \in \mathcal{V}}$ is the representing “matrix”. As such, we introduce, for all $s, s' \in \overline{\mathcal{M}}$, the simplifying abbreviations

$$\langle K_s, K_{s'} \rangle = \sum_{u, v \in \mathcal{V}} K(s, u)K(s', v)\mathbf{c}(u, v), \quad \|K_s\|^2 = \sum_{u, v \in \mathcal{V}} K(s, u)K(s, v)\mathbf{c}(u, v). \quad (6)$$

Remark 4. If $\mathcal{V} \subseteq \overline{\mathcal{M}}$ and $k : \overline{\mathcal{M}} \rightarrow \mathbb{R}$, then we call the SuRF obtained from the kernel given in Remark 1 a *convolution field*. Convolution fields appear naturally in many applications since convolving the observed data with a smoothing kernel is often a preprocessing step in signal processing or neuroimaging to improve the signal to noise ratio [Turin, 1960, Worsley et al., 2002].

SuRFs are random fields with nice properties as most path properties are directly inherited from the kernel K . This is theoretically advantageous, as one can often establish the assumptions of results like the GKF by imposing conditions like differentiability on the kernel K . The following proposition is self-evident but provided here for convenience.

Proposition 1. *Let $(\tilde{X}, X, K, \mathcal{V})$ be a SuRF and $k \geq 0$. If $K(\cdot, v) \in \mathcal{C}^k(\overline{\mathcal{M}})$ for all $v \in \mathcal{V}$, then \tilde{X} has sample paths of class \mathcal{C}^k .*

3.2 Gaussian Kinematic Formula for SuRFs

To demonstrate the benefit of thinking in terms of SuRFs we pose assumptions on a kernel K and the discrete field X such that the corresponding normalized SuRF \tilde{X} satisfies the assumptions of the GKF [Adler and Taylor, 2009, Theorem 12.4.1, 12.4.2]. Thus, we first state the assumptions on a random field f defined over $\overline{\mathcal{M}}$ such that the GKF over \mathcal{M} holds. Recall that f_α is the representation of f in the chart $(\overline{U}_\alpha, \overline{\phi}_\alpha)$ as introduced in Section 2. In this notation the GKF holds, if for all $\alpha \in \{1, \dots, P\}$ and $(\overline{U}_\alpha, \overline{\phi}_\alpha)$ from the atlas of $\overline{\mathcal{M}}$ we have that

(G1) f is a zero-mean, unit-variance and Gaussian on $\overline{\mathcal{M}}$ with a.s. \mathcal{C}^2 -sample paths.

(G2) $(\nabla f_\alpha(x), \mathbb{V}(\nabla^2 f_\alpha(x)))$ is non-degenerate for all $x \in \overline{\phi}_\alpha(\overline{U}_\alpha) \cap \mathcal{M}$.

(G3) There exist constants $\kappa, \gamma, \epsilon > 0$ such that for each $d, d' \in \{1, \dots, D\}$,

$$\mathbb{E} \left[\left(\partial_{dd'} f_\alpha(x) - \partial_{dd'} f_\alpha(y) \right)^2 \right] \leq \kappa \left| \log \|x - y\| \right|^{-1-\gamma},$$

for all $x, y \in \overline{\phi}_\alpha(\overline{U}_\alpha) \cap \mathcal{M}$ for which $|x - y| < \epsilon$.

Remark 5. Conditions **(G1)**-**(G3)** imply that the sample paths of f are almost surely Morse functions, compare [Adler and Taylor, 2009, Corollary 11.3.2.]. Moreover, by Lemma 1 from Davenport and Telschow [2022] these conditions do not depend on the particular choice of the \mathcal{C}^3 charts (U_α, ϕ_α) , $\alpha \in \{1, \dots, P\}$, but rather hold for all \mathcal{C}^3 charts (V, φ) of $\overline{\mathcal{M}}$.

Applying Proposition 1, **(G1)** holds for any normalized SuRF derived from a zero-mean Gaussian random field X on \mathcal{V} and a twice continuously differentiable kernel K . The next two propositions establish that Condition **(G3)** is satisfied for a SuRF with a \mathcal{C}^3 -kernel.

Proposition 2. *Let $\gamma \in (0, 1]$ and for all $v \in \mathcal{V}$ let $K_\alpha(\cdot, v)$ be γ -Hölder continuous for all $\alpha \in \{1, \dots, P\}$ with Hölder constants bounded above by $A > 0$ and $\mathbb{E}[X(v)^p] < \infty$, $p \in [1, \infty)$. Then \tilde{X} has almost surely \mathcal{L}^p -Hölder continuous paths, i.e.,*

$$|\tilde{X}_\alpha(x) - \tilde{X}_\alpha(y)| \leq L \|x - y\|^\gamma \quad (7)$$

for the charts $(\bar{U}_\alpha, \bar{\phi}_\alpha)$, $\alpha \in \{1, \dots, P\}$, in the atlas of $\bar{\mathcal{M}}$ covering \mathcal{M} , all $x, y \in \bar{\phi}(\bar{U}_\alpha) \cap \mathcal{M}$ and some random variable L with finite p -th moment.

Proposition 3. Let $K(\cdot, v) \in \mathcal{C}^1(\bar{\mathcal{M}})$ and $\mathbb{E}[X(v)^2] < \infty$ for all $v \in \mathcal{V}$. Then there exists a constant $\kappa > 0$ for $\alpha \in \{1, \dots, P\}$ such that

$$\mathbb{E} \left[\left(\tilde{X}_\alpha(x) - \tilde{X}_\alpha(y) \right)^2 \right] \leq \kappa \left| \log \|x - y\| \right|^{-2} \quad (8)$$

for all $x, y \in \bar{\phi}(\bar{U}_\alpha) \cap \mathcal{M}$ such that $0 < \|x - y\| < 1$.

Remark 6. Proposition 3 implies condition **(G3)** for a \mathcal{C}^3 -kernel K because each second order partial derivative of a normalized SuRF is a SuRF with continuous sample paths.

Definition 3. Given a set $\mathcal{W} \subset \mathbb{R}^D$, we say that functions $f_1, \dots, f_J : \mathcal{W} \rightarrow \mathbb{R}$ are \mathcal{W} -linearly independent if given constants $a_1, \dots, a_J \in \mathbb{R}$, the relation

$$\sum_{j=1}^J a_j f_j(w) = 0$$

holding for all $w \in \mathcal{W}$ implies that $a_j = 0$ for all $j \in \{1, \dots, J\}$.

The following propositions link the linear independence of functions $K_\alpha(x, \cdot)$ for $x \in \bar{\phi}_\alpha(\bar{U}_\alpha \cap \mathcal{M})$ with Condition **(G2)** for SuRFs. We demonstrate that the needed linear independence condition for achieving **(G2)** is satisfied, for example, by Gaussian kernels.

Proposition 4. Let $(\tilde{X}, X, K, \mathcal{V})$ be a SuRF with $K(\cdot, v) \in \mathcal{C}^2(\bar{\mathcal{M}})$ for all $v \in \mathcal{V}$ and \tilde{Z} be the corresponding normalized SuRF. For $\alpha \in \{1, \dots, P\}$ and $x \in \bar{\phi}_\alpha(\bar{U}_\alpha) \cap \mathcal{M}$ define $K_\alpha(x, \cdot) : \mathcal{V} \rightarrow \mathbb{R}$ by $v \mapsto K(\bar{\phi}_\alpha^{-1}(x), v)$ and set $\mathcal{V}_x = \{v \in \mathcal{V} : K_\alpha(x, v) \neq 0\}$. Assume that $K_\alpha(x, \cdot)$, $\partial_d^x K_\alpha(x, \cdot)$ and $\partial_{d'd''}^x K_\alpha(x, \cdot)$ for $d, d', d'' \in \{1, \dots, D\}$ with $1 \leq d' \leq d'' \leq D$ are \mathcal{V}_x -linearly independent and the random vector $(X(v) : v \in \mathcal{V}_x)$ is non-degenerate. Then

$$\left(\tilde{X}_\alpha(x), \nabla \tilde{X}_\alpha(x), \mathbb{V}(\nabla^2 \tilde{X}_\alpha(x)) \right) \text{ and } \left(\tilde{Z}_\alpha(x), \nabla \tilde{Z}_\alpha(x), \mathbb{V}(\nabla^2 \tilde{Z}_\alpha(x)) \right)$$

are non-degenerate Gaussian random vectors.

Proposition 5. Let $\tilde{D} = D + 1 + D(D + 1)/2$ and $\alpha \in \{1, \dots, P\}$. Taking the gradient and Hessian w.r.t. $x \in \bar{\phi}_\alpha(\bar{U}_\alpha \cap \mathcal{M})$ we define the vector valued functions

$$\mathbf{K}_{\alpha,x}(v) = \left(K_\alpha(x, v), \nabla K_\alpha(x, v), \mathbb{V}(\nabla^2 K_\alpha(x, v)) \right) \quad (9)$$

indexed by $x \in \bar{\phi}_\alpha(\bar{U}_\alpha \cap \mathcal{M})$. If for each $x \in \bar{\phi}_\alpha(\bar{U}_\alpha \cap \mathcal{M})$ there exist $v_1, \dots, v_{\tilde{D}} \in \mathcal{V}_x$ such that $\mathbf{K}_{\alpha,x}(v_1), \dots, \mathbf{K}_{\alpha,x}(v_{\tilde{D}})$ are linearly independent, then $K_\alpha(x, \cdot)$, $\partial_d^x K_\alpha(x, \cdot)$ and $\partial_{d'd''}^x K_\alpha(x, \cdot)$ for $d, d', d'' \in \{1, \dots, D\}$ with $1 \leq d' \leq d'' \leq D$ are \mathcal{V}_x linearly independent.

Remark 7. The results in Propositions 4 and 5 are stronger than **(G2)** as we want to emphasize that SuRFs often satisfy the assumptions of the expectation Metatheorem 11.2.1 from [Adler and Taylor \[2009\]](#), see Corollary 11.2.2 for the Gaussian version. However, our proofs show that **(G2)** follows already from the assumption that $\partial_d^x K(x, \cdot)$ and $\partial_{d'd''}^x K(x, \cdot)$ for $d \in \{1, \dots, D\}$ and $1 \leq d' \leq d'' \leq D$ is \mathcal{V}_x -linearly independent for all $x \in \bar{\phi}(\bar{U}_\alpha) \cap \mathcal{M}$ and $\alpha \in \{1, \dots, P\}$.

Proposition 6. Let $K(s, v) = e^{-(s-v)^T \Omega (s-v)/2}$, for some positive definite matrix $\Omega \in \mathbb{R}^{D \times D}$ be the D -dimensional Gaussian kernel. Assume that \mathcal{V} is a D -dimensional lattice which contains an element v such that

$$\left\{ v + \sum_{d=1}^D \lambda_d \gamma_d e_d : \gamma_d \in \{-1, 0, 1\} \right\} \subset \mathcal{V}$$

where $(e_d)_{1 \leq d \leq D}$ is the standard basis and $\lambda \in \mathbb{R}_{>0}^D$. Then $K(s, \cdot)$, $\partial_d^s K(s, \cdot)$ and $\partial_{d', d''}^s K(s, \cdot)$ for $d \in \{1, \dots, D\}$ and $1 \leq d' \leq d'' \leq D$ are \mathcal{V}_s -linearly independent for each $s \in \mathbb{R}^D$.

The above conditions allow us to consider the GKF for Gaussian related fields obtained from Gaussian SuRFs as a corollary to Theorem 12.4.2 from Adler and Taylor [2009]. We define $\mathcal{A}_u(f) = \{s \in \mathcal{M} : f(s) \geq u\}$ to be the excursion set of a random field f above the threshold u on \mathcal{M} and write $\chi_f(u)$ to denote the Euler characteristic (EC) of the excursion set $\mathcal{A}_u(f)$.

Theorem 1. Let $(\tilde{X}_1, X_1, K, \mathcal{V}), \dots, (\tilde{X}_N, X_N, K, \mathcal{V}) \sim (\tilde{X}, X, K, \mathcal{V})$ be i.i.d. SuRFs and $F \in \mathcal{C}^2(\overline{\mathcal{M}})$. Assume that X is a Gaussian field on \mathcal{V} with covariance function \mathfrak{c} and that for all $v \in \mathcal{V}$ it holds that $K(\cdot, v) \in \mathcal{C}^3(\overline{\mathcal{M}})$ and $\mathfrak{c}(v, v) > 0$. Furthermore, for all $\alpha \in \{1, \dots, P\}$ and $x \in \overline{\phi}(\overline{U}_\alpha) \cap \mathcal{M}$ assume that the random vector $(X(v) : v \in \mathcal{V}_x)$ is non-degenerate for the \mathcal{V}_x defined in Proposition 4 and that $\partial_d^x K_\alpha(x, \cdot)$ and $\partial_{d', d''}^x K_\alpha(x, \cdot)$ for $d \in \{1, \dots, D\}$ and $1 \leq d' \leq d'' \leq D$ are \mathcal{V}_x -linearly independent. Define a random field T such that $T(s) = F(\tilde{X}_1(s)/\|K_s\|, \dots, \tilde{X}_N(s)/\|K_s\|)$ for all $s \in \overline{\mathcal{M}}$. Then

$$\mathbb{E}[\chi_T(u)] = \sum_{d=0}^D \mathcal{L}_d \rho_d^T(u), \quad u \in \mathbb{R}, \quad (10)$$

where $\mathcal{L}_0, \dots, \mathcal{L}_D \in \mathbb{R}$ are the LKCs of $\overline{\mathcal{M}}$ endowed with the induced Riemannian metric from $\tilde{X}(s)/\|K_s\|$ and ρ_d^T 's are functions depending solely on the marginal distribution of T .

3.3 Voxel Manifolds

Until now we did not discuss what domain $\mathcal{M} \subset \overline{\mathcal{M}}$ we should choose for a SuRF derived from a kernel K and a discrete random field X on a finite grid \mathcal{V} . In the case that $\overline{\mathcal{M}}$ is a D -dimensional submanifold of \mathbb{R}^D and $\mathcal{V} \subset \mathbb{R}^D$ and $K(\cdot, v) : \mathbb{R}^D \rightarrow \mathbb{R}$, for each $v \in \mathcal{V}$, we propose to use a practical domain which we call the *voxel manifold associated with \mathcal{V}* .

Definition 4. Suppose that $\mathcal{V} \subset \mathbb{R}^D$ is a discrete set and define $\delta \in \mathbb{R}^D$ such that its d -th component is $\delta_d = \min \{|v_d - w_d| : v, w \in \mathcal{V}, v_d \neq w_d\}$. Moreover, let

$$\mathcal{B}_v(\delta) = \left\{ x \in \mathbb{R}^D \mid \max_{d \in \{1, \dots, D\}} |x_d - v_d| - \delta_d/2 \leq 0 \right\}. \quad (11)$$

Then the *voxel manifold associated with \mathcal{V}* is the set $\mathcal{M}_\mathcal{V} = \bigcup_{v \in \mathcal{V}} \mathcal{B}_v(\delta)$.

A voxel manifold is a stratified space, for example, for $D = 3$ by the three dimensional stratum is the union of all the open cubes $\text{int}(\mathcal{B}_v(\delta))$ with $v \in \mathcal{V}$, while the two dimensional, the one dimensional and the zero dimensional strata are the unions over all $v \in \mathcal{V}$ of all faces, edges and corners of the cubes $\mathcal{B}_v(\delta)$ respectively. In fact, a voxel manifold as the union of polyhedra is even a WS manifold [Adler and Taylor, 2009, p.187].

Remark 8. Figure I in [Worsley et al. \[1996\]](#) is somewhat suggestive of a voxel manifold. However they used in a different choice of domain, instead defining a cube by 8 neighbouring voxels while in $\mathcal{M}_{\mathcal{V}}$ each voxel v defines a cube. Crucially, they only used this choice of domain in order to estimate the intrinsic volumes while their test statistic is still $\max_{v \in \mathcal{V}} T(v)$, i.e. the maximum over the values that the test-statistic takes at the voxels.

Throughout the rest of this article we assume that $\mathcal{B}_v(\delta) \subset \text{supp}(K(\cdot, v))$ for all $v \in \mathcal{V}$ because otherwise **(G2)** cannot be true as the corresponding SuRF is zero on parts of $\mathcal{M}_{\mathcal{V}}$. This condition on the support, however, is usually satisfied as the kernel K is typically used to increase the signal-to-noise ratio through averaging observations at different $v \in \mathcal{V}$.

In Riemannian geometry most geometric quantities can be derived from the Riemannian metric and the Christoffel symbols. Using [Theorem 4](#) and [5](#) from [Appendix B.1](#) these quantities for the Riemannian metric induced by a normalized SuRF on $\overline{\mathcal{M}}$ can be written in terms of the inner products introduced in [\(6\)](#).

Proposition 7. For $\overline{\mathcal{M}} \subset \mathbb{R}^D$ the Riemannian metric $\mathbf{\Lambda}$ induced by a normalized SuRF expressed in the local coordinates induced by $\iota : \overline{\mathcal{M}} \hookrightarrow \mathbb{R}^D$ is given by

$$\Lambda_{dd'}(x) = \frac{\langle \partial_d K_x, \partial_{d'} K_x \rangle}{\|K_x\|^2} - \frac{\langle \partial_d K_x, K_x \rangle \langle K_x, \partial_{d'} K_x \rangle}{\|K_x\|^4} \quad (12)$$

and the Christoffel symbols of the first kind are

$$\begin{aligned} \Gamma_{kdd'}(x) &= \frac{\langle \partial_k \partial_d K_x, \partial_{d'} K_x \rangle}{\|K_x\|^2} - \frac{\langle \partial_k \partial_d K_x, K_x \rangle \langle K_x, \partial_{d'} K_x \rangle}{\|K_x\|^4} \\ &\quad - \frac{\langle \partial_k K_x, K_x \rangle \langle \partial_d K_x, \partial_{d'} K_x \rangle}{\|K_x\|^4} - \frac{\langle \partial_d K_x, K_x \rangle \langle \partial_k K_x, \partial_{d'} K_x \rangle}{\|K_x\|^4} \\ &\quad + 2 \frac{\langle \partial_k K_x, K_x \rangle \langle \partial_d K_x, K_x \rangle \langle K_x, \partial_{d'} K_x \rangle}{\|K_x\|^6} \end{aligned} \quad (13)$$

The advantage of using the voxel manifold domain for a SuRF is that the numerical implementation of geometric quantities is feasible and therefore estimators of the LKCs can be calculated efficiently, because all d -dimensional boundaries lie in hyperplanes parallel to the coordinate axes. It is helpful here that we can construct for any $x \in \mathcal{U}$ and a small open neighborhood $\mathcal{U} \ni x$ an orthonormal basis of $\mathcal{T}_x \mathcal{M}_{\mathcal{V}}$, $x \in \mathcal{M}_{\mathcal{V}} \cap \mathcal{U}$, such that a subset of this basis is an orthonormal frame of $\mathcal{T}_x \partial_d \mathcal{M}_{\mathcal{V}}$, $d \in \{1, \dots, D-1\}$, if $x \in \partial_d \mathcal{M}_{\mathcal{V}} \cap \mathcal{U}$. More concretely, for $D = 3$ the Gram-Schmidt procedure on the Euclidean basis e_1, e_2, e_3 yields the following orthonormal vector fields with respect to the Riemannian metric induced by a SuRF at $x \in \mathcal{M}_{\mathcal{V}}$ and $k, l, m \in \{1, 2, 3\}$ such that $k < l$ and $\{k, l, m\} = \{1, 2, 3\}$:

$$\begin{aligned} U_x &= \Lambda_{kk}^{-1/2}(x) e_k, \quad V_x = \frac{\Lambda_{kl}(x)}{\sqrt{c(x) \Lambda_{kk}(x)}} e_k - \sqrt{\frac{\Lambda_{kk}(x)}{c(x)}} e_l, \\ N_x &= \frac{\mathbf{\Lambda}^{-1}(x)}{\sqrt{e_m^T \mathbf{\Lambda}^{-1}(x) e_m}} e_m. \end{aligned} \quad (14)$$

Here $c(x) = \det(\mathbf{\Lambda}^I(x))$ for $I = (k, l)$ and U_x, V_x are a basis of $\mathcal{T}_x \mathcal{F}_I$, where \mathcal{F}_I is the subset of $\partial_2 \mathcal{M}_{\mathcal{V}}$ such that the coordinates with indices not contained in I are constant, and N_x is in the one dimensional vector space orthogonal to $\mathcal{T}_x \mathcal{F}_I$ with respect to $\mathbf{\Lambda}$.

3.4 LKCs of Voxel Manifolds

General formulas for the LKCs of WS manifolds can be found in [Adler and Taylor, 2009, Theorem 12.4.2] and formulas for WS manifolds of dimension $D \leq 3$ are given in Appendix B.2. Since voxel manifolds are embedded into \mathbb{R}^D and have a simple geometric structure, the highest two LKCs can be expressed as integrals of (sub-)determinants of the Riemannian metric $\mathbf{\Lambda}$, i.e.,

$$\mathcal{L}_D = \sum_{\nu \in \mathcal{V}} \int_{\mathcal{B}_\nu(\delta)} \sqrt{\det(\mathbf{\Lambda}(x))} dx, \quad \mathcal{L}_{D-1} = \sum_{I:|I|=D-1} \int_{\mathcal{F}_I} \sqrt{\det(\mathbf{\Lambda}^I(x))} dx^I.$$

Here I is any ordered subset of $\{1, \dots, D\}$, $dx^I = dx_{I_1} \dots dx_{I_{|I|}}$ and $\mathbf{\Lambda}^I(x)$ is the submatrix of $\mathbf{\Lambda}(x)$ consisting of the columns and rows given by the entries of I . Finally, \mathcal{F}_I is the subset of $\mathcal{M}_\mathcal{V} \setminus \partial_D \mathcal{M}_\mathcal{V}$ such that the coordinates with indices not contained in I are constant.

The LKCs $\mathcal{L}_1, \dots, \mathcal{L}_{D-2}$ of a D -dimensional voxel manifold with $D > 2$ are substantially harder to express explicitly, compare [Adler and Taylor, 2009, Theorem 12.4.2] and Theorem 6 in Appendix B.2 for 3-dimensional voxel manifolds.

3.5 SuRF Estimator for LKCs

Given a kernel $K : \mathcal{M}_\mathcal{V} \times \mathcal{V} \rightarrow \mathbb{R}$ and an i.i.d. sample X_1, \dots, X_N of a Gaussian random field X over \mathcal{V} , we obtain from formula (12) for the Riemannian metric $\mathbf{\Lambda}(x)$ the SuRF-Riemannian metric estimator

$$\hat{\Lambda}_{dd'}(x) = \frac{\text{Cov} \left[\partial_d \tilde{\mathbb{X}}(x), \partial_{d'} \tilde{\mathbb{X}}(x) \right]}{\text{Var} \left[\tilde{\mathbb{X}}(x) \right]} - \frac{\text{Cov} \left[\partial_d \tilde{\mathbb{X}}(x), \tilde{\mathbb{X}}(x) \right] \text{Cov} \left[\tilde{\mathbb{X}}(x), \partial_{d'} \tilde{\mathbb{X}}(x) \right]}{\text{Var} \left[\tilde{\mathbb{X}}(x) \right]^2}. \quad (15)$$

Here the variances and covariances are sample variances and covariances of the sample $\tilde{\mathbb{X}} = (\tilde{X}_1, \dots, \tilde{X}_N)$ and its derivatives $\partial_d \tilde{\mathbb{X}}(x)$. The latter can be computed from the derivatives of the kernel K , compare Proposition 1. Hence, (15) uses the exact derivatives of the sample fields. We denote with $\hat{\mathbf{\Lambda}}(x) \in \mathbb{R}^{D \times D}$, $x \in \mathcal{M}_\mathcal{V}$, the matrix with (d, d') -th entry $\hat{\Lambda}_{dd'}(x)$. To estimate the LKCs we evaluate $\hat{\mathbf{\Lambda}}(x)$ on a grid $\mathcal{M}_\mathcal{V}^{(r)} \subset \mathcal{M}_\mathcal{V}$ given by

$$\mathcal{M}_\mathcal{V}^{(r)} = \bigcup_{v \in \mathcal{V}} \mathcal{B}_v(\delta) \cap \left(v + \frac{\delta}{r+1} \cdot \mathbb{Z}^D \right). \quad (16)$$

Here $r \in \{2r' + 1 \mid r' \in \mathbb{N}\}$ is called the *added resolution*. The restriction to odd numbers greater zero is necessary to ensure that the boundary of $\mathcal{M}_\mathcal{V}$ is sampled. Consequentially, the *SuRF-LKC estimators with added resolution r* for \mathcal{L}_D and \mathcal{L}_{D-1} are given by

$$\hat{\mathcal{L}}_D^{(r)} = \sum_{x \in \mathcal{M}_\mathcal{V}^{(r)}} \sqrt{\det(\hat{\mathbf{\Lambda}}(x))} \prod_{d=1}^D \frac{\delta_d}{r+1}. \quad (17)$$

$$\hat{\mathcal{L}}_{D-1}^{(r)} = \sum_{|I|=D-1} \sum_{x \in \mathcal{F}_I^{(r)}} \sqrt{\det(\hat{\mathbf{\Lambda}}^I(x))} \prod_{i \in I} \frac{\delta_i}{r+1}.$$

Here $\mathcal{F}_I^{(r)} = \mathcal{F}_I \cap \mathcal{M}_\mathcal{V}^{(r)}$. These formulas are easy to implement and as r goes to infinity the numerical error in approximating the integral by a Riemann sum becomes arbitrary small. In the same fashion it is possible to obtain estimators $\hat{\mathcal{L}}_{D-d}^{(r)}$, $d \in \{1, \dots, D-2\}$, from Theorem 12.4.2 in Adler and Taylor [2009] and our formulas of the geometric quantities induced by a SuRF on $\mathcal{M}_\mathcal{V}$, compare Corollary 7 and Appendix B.2. In practice these estimators are tedious to implement and they are computationally costly, because even for a 3-dimensional voxel manifold we need for the Christoffel symbols 27 convolutions on top of the 9 convolutions required to estimate the Riemannian metric. Computing the Riemannian curvature tensor needs another 36 convolutions. A solution is to approximate the lower LKCs by their locally stationary counterparts, i.e., for $D = 3$ only the first integral in Theorem 6 remains:

$$\hat{\mathcal{L}}_1^{(r)} = \sum_{|I|=1} \sum_{v \in \mathcal{F}_I^{(r)}} \hat{\Theta}(v) \sqrt{\hat{\mathbf{A}}^I(v)} \frac{\delta_I}{r+1}. \quad (18)$$

Here $\hat{\Theta}$ is the plug-in estimate of Θ defined in Theorem 6.

Theorem 2. *Let K be the kernel of the SuRF and $d \in \{D-1, D\}$. Assume that $K(\cdot, v) \in \mathcal{C}^3$ for all $v \in \mathcal{V}$ and that $\mathbb{E}[X(v)] < \infty$ for all $v \in \mathcal{V}$. Then*

$$\lim_{r \rightarrow \infty} \mathbb{E} \left[\hat{\mathcal{L}}_d^{(r)} \right] = \mathbb{E} \left[\lim_{r \rightarrow \infty} \hat{\mathcal{L}}_d^{(r)} \right] = \mathcal{L}_d.$$

Theorem 3. *Let $d \in \{D-1, D\}$, $K(\cdot, v) \in \mathcal{C}^3(\overline{\mathcal{M}})$ and $\mathbb{E}[X(v)^2] < \infty$ for $v \in \mathcal{V}$. Then*

$$\lim_{N \rightarrow \infty} \lim_{r \rightarrow \infty} \hat{\mathcal{L}}_d^{(r)} = \lim_{r \rightarrow \infty} \lim_{N \rightarrow \infty} \hat{\mathcal{L}}_d^{(r)} = \mathcal{L}_d. \quad (19)$$

Remark 9. We expect that a similar result can be derived for the plugin estimator \mathcal{L}_1 resulting from Theorem 6 where also the $\Gamma_{kdd'}$'s from (13) and the Riemannian curvature, Appendix B.1, are estimated using the corresponding sample covariances. This result could be established along the same lines as the consistency in [Telschow et al., 2023, Section 3], but we leave this for future work since, currently, implementing this estimator seems infeasible.

3.6 FWER Control Using SuRFs

In this section we illustrate how the GKF is used to construct a test controlling the family-wise error rate (FWER) which dates back to Worsley et al. [1992] and combine this approach with SuRFs in order to improve the power of RFT based voxelwise inference. We illustrate this on the problem of detecting areas of non-zero signal μ , given an *i.i.d.* sample $X_1, \dots, X_N \sim X$, in a signal plus noise model $X(v) = \mu(v) + \epsilon(v)$ for $v \in \mathcal{V}$ and ϵ a zero-mean random field. The same approach, however, can be applied to the linear model, e.g., Supplementary of Telschow et al. [2023], and other probabilistic models for which there is a GKF, e.g., Worsley [1994], Taylor and Worsley [2007, 2008].

Let $\tilde{X}_1, \dots, \tilde{X}_N$ denote a sample of SuRFs over $\mathcal{M}_\mathcal{V}$ derived from random fields X_1, \dots, X_N over \mathcal{V} .⁵ Assume the setting of Theorem 1 and define $F : \mathbb{R}^N \rightarrow \mathbb{R}$ by

$$F(a_1, \dots, a_N) = \frac{1}{\sqrt{N}} \sum_{i=1}^N a_i \left(\frac{1}{N-1} \sum_{i=1}^N \left(a_i - \frac{1}{N} \sum_{i=1}^N a_i \right)^2 \right)^{-1/2}$$

⁵Technically, stating the GKF requires the SuRFs to be defined on a D -dimensional, compact manifold without boundary $\overline{\mathcal{M}_\mathcal{V}} \supset \mathcal{M}_\mathcal{V}$

for $(a_1, \dots, a_N) \in \mathbb{R}^N$. Let $\mu(v) = \mathbb{E}[X(v)]$ for $v \in \mathcal{V}$ and for all $x \in \mathcal{M}_{\mathcal{V}}$, let

$$\tilde{\mu}(x) = \sum_{v \in \mathcal{V}} K(x, v) \mu(v).$$

Due to the invariance of F to scaling, for $x \in \mathcal{M}_{\mathcal{V}}$, we can write

$$\tilde{T}(x) := F(\tilde{X}_1(x)/\|K_x\|, \dots, \tilde{X}_N(x)/\|K_x\|) = \frac{\sqrt{N} \hat{\mu}_N(x)}{\hat{\sigma}_N(x)} \quad (20)$$

where $\hat{\mu}_N(x) = \frac{1}{N} \sum_{i=1}^N \tilde{X}_i(x)$ and $\hat{\sigma}_N(x) = \left(\frac{1}{N-1} \sum_{i=1}^N (\tilde{X}_i(x) - \hat{\mu}_N(x))^2 \right)^{1/2}$.

Our goal is to construct based on \tilde{T} a multiple hypothesis test for the hypotheses

$$\mathbf{H}_0^x : \tilde{\mu}(x) \leq 0 \quad \text{vs.} \quad \mathbf{H}_1^x : \tilde{\mu}(x) > 0 \quad x \in \mathcal{M}_{\mathcal{V}} \quad (21)$$

which controls the FWER in the strong sense at a significance level $\alpha \in (0, 1)$.⁶ Denote with $\mathcal{H}_0 = \{x \in \mathcal{M}_{\mathcal{V}} \mid \tilde{\mu}(x) \leq 0\} \subseteq \mathcal{M}_{\mathcal{V}}$ the set of true null hypotheses and consider the test that rejects \mathbf{H}_0^x , $x \in \mathcal{M}_{\mathcal{V}}$, whenever $\tilde{T}(x) > u_\alpha$. Then its FWER at $u \in \mathbb{R}$ is

$$\text{FWER}_{\tilde{T}}(u) = \mathbb{P} \left(\sup_{x \in \mathcal{H}_0} \tilde{T}(x) > u \right).$$

Defining $\tilde{T}_0 = \sqrt{N}(\hat{\mu}_N(x) - \tilde{\mu}(x))/\hat{\sigma}_N(x)$, then any u_α satisfying

$$\mathbb{P} \left(\max_{x \in \mathcal{M}_{\mathcal{V}}} \tilde{T}_0(x) > u_\alpha \right) \leq \alpha$$

for $\alpha \in (0, 1)$, controls the FWER in the strong sense at the level α because

$$\text{FWER}_{\tilde{T}}(u_\alpha) \leq \mathbb{P} \left(\max_{x \in \mathcal{M}_{\mathcal{V}}} \tilde{T}_0(x) > u_\alpha \right) \leq \alpha$$

for all $\mathcal{H}_0 \subseteq \mathcal{M}_{\mathcal{V}}$ and $\tilde{T}_0(x) = \tilde{T}(x)$ for all $x \in \mathcal{H}_0$. To find such a threshold u_α we use the EEC heuristic [Taylor et al. \[2005\]](#) to the excursion probability. In particular, letting $M_u(\tilde{T}_0)$ be the number of local maxima of \tilde{T}_0 over $\mathcal{M}_{\mathcal{V}}$ that lie above the level u and $\chi_{\tilde{T}_0}(u)$ be the EC of the excursion set $\{x \in \mathcal{M}_{\mathcal{V}} \mid \tilde{T}_0(x) > u\}$ we have that

$$\mathbb{P} \left(\max_{x \in \mathcal{M}_{\mathcal{V}}} \tilde{T}_0(x) > u \right) \leq \mathbb{E}[M_u(\tilde{T}_0)] \approx \mathbb{E} \left[\chi_{\tilde{T}_0}(u) \right] = \sum_{d=0}^D \mathcal{L}_d \rho_d^{\tilde{T}_0}(u). \quad (22)$$

Here $\rho_d^{\tilde{T}_0}$ are the EC densities of a (centered) t -field given, compare [[Taylor and Worsley, 2007](#), p.915]. In order to control the FWER in the strong sense to a level $\alpha \in (0, 1)$, we find the largest u_α such that $\sum_{d=0}^D \hat{\mathcal{L}}_d \rho_d^T(u_\alpha) = \alpha$ using the $\hat{\mathcal{L}}_d$'s from [Section 3.5](#). At high thresholds u_α the number of local maxima is either zero or one and so $\mathbb{E} \left[\chi_{\tilde{T}_0}(u_\alpha) \right]$ is an extremely good approximation to $\mathbb{E}[M_{u_\alpha}(\tilde{T}_0)]$. Lower values of α yield higher thresholds u_α . At a typical value $\alpha \leq 0.05$, we expect the approximation in [\(22\)](#) to be accurate.

Traditional RFT inference in neuroimaging [[Worsley et al., 1992, 1996](#), [Taylor and Worsley, 2007](#)] uses the same framework but only evaluates the fields on the lattice \mathcal{V} and uses the LKC

⁶The two-sided hypothesis can be treated similarly.

estimators given in Forman et al. [1995], Kiebel et al. [1999] or Taylor and Worsley [2007] which are based on discrete derivatives. More precisely, for each $n \in \{1, \dots, N\}$ it takes data X_n on a lattice \mathcal{V} (corresponding to the centers of voxels making up the brain), smoothes it with a kernel K to obtain $\{\tilde{X}_n(v) : v \in \mathcal{V}\}$ and rejects all $v \in \mathcal{V}$ such that $\tilde{T}(v) > u_\alpha$ where u_α is obtained from the GKF approximation such that $\mathbb{P}(\max_{s \in \mathcal{M}} \tilde{T}_0(s) > u_\alpha) \approx \alpha$. Here $\mathcal{M} \subset \mathbb{R}^3$ represents for example the brain, but has never been defined precisely in the literature as it probably was assumed to be unnecessary by the good lattice assumption. By construction this leads to valid, but conservative inference since $\max_{v \in \mathcal{V}} \tilde{T}_0(s) \leq \max_{s \in \mathcal{M}} \tilde{T}_0(s)$ and u_α approximates the tails of the distribution of $\max_{s \in \mathcal{M}} \tilde{T}_0(s)$ at level α and not the tails of the distribution of $\max_{v \in \mathcal{V}} \tilde{T}_0(v)$. SuRFs allow to remove this conservativeness by specifying \mathcal{M} to be the voxel manifold $\mathcal{M}_\mathcal{V}$ and testing $\tilde{T}(x) > u_\alpha$ for all $x \in \mathcal{M}_\mathcal{V}$ meaning that u_α approximates the quantiles of the test statistic. Consequentially, our SuRF framework has strong FWER control over $\mathcal{M}_\mathcal{V}$ at level α up to the approximation in (22) and thus has a higher power than traditional RFT.

Effect Localization In the discussed framework as often in applications the discrete data has been smoothed before carrying out statistical inference. Therefore precise localization of significant effects, i.e., finding $x \in \mathcal{M}_\mathcal{V}$ such that $\tilde{\mu}(x) \neq 0$, is only possible for the smoothed signal; yet weaker localization results for the $v \in \mathcal{V}$ such that $\mu(v) \neq 0$ hold.⁷ The key observation is that, if $K(x, v) \geq 0$ for all $x \in \mathcal{M}_\mathcal{V}$ and all $v \in \mathcal{V}$, it holds that

$$\tilde{\mu}(x) > 0 \iff \exists v \in \mathcal{V} \cap \text{supp}(K(x, \cdot)) : \mu(v) > 0. \quad (23)$$

Thus, if we reject \mathbf{H}_0^x we can conclude by (23) that there is at least one $v \in \mathcal{V} \cap \text{supp}(K(x, \cdot))$ such that $\mu(v) > 0$ and the strong control on the hypotheses (21) yields

$$\begin{aligned} \mathbb{P}\left(\{x' \in \mathcal{M}_\mathcal{V} \mid \mathbf{H}_0^{x'} \text{ is rejected}\} \subseteq \mathcal{M}_\mathcal{V} \setminus \mathcal{H}_0\right) &= 1 - \mathbb{P}\left(\exists x \in \mathcal{H}_0 : \mathbf{H}_0^x \text{ is rejected}\right) \\ &\geq 1 - \alpha. \end{aligned}$$

Consequentially, $\tilde{T}(x) > u_\alpha$ implies that the probability of incorrectly claiming that $\mu(v) > 0$ for a $v \in \mathcal{V} \cap \text{supp}(K(x, \cdot))$ is at most α . This is a weaker form of FWER control than controlling it in the strong sense, but stronger than controlling it in the weak sense as long as $\text{supp}(K(x, \cdot)) \neq \mathcal{M}_\mathcal{V}$ for at least one $x \in \mathcal{M}_\mathcal{V}$.

Remark 10. Losing strong control with respect to μ due to smoothing the data is natural in applications such as fMRI. Smoothing is needed to increase the low signal-to-noise ratio and it is even debatable whether it is plausible to talk about the BOLD signal at a single voxel in a realistic fMRI experiment as the analyzed BOLD signal at v is a distorted version of the observed data due to an extensive preprocessing pipeline which includes, among other aspects, motion correction and warping to a standardized brain.

4 Simulations

In this section we compare using simulations the performance of the SuRF estimator of the LKCs from Section 3.5 to existing LKC estimators; namely, the Hermite projection estimator (HP) and its bootstrap improvement (bHP) from [Telschow et al., 2023] and the LKC estimators developed for stationary processes from Kiebel et al. [1999] and Forman et al. [1995] which are

⁷Our arguments carry over to tests controlling the FWER in the strong sense w.r.t. the smoothed signal, for example, permutation tests in fMRI as they are typically applied to smoothed data.

used in established software, e.g., SPM and FSL. We abbreviate the latter two estimators as *Kie* and *For* respectively. We do not compare to the warping estimator [Taylor and Worsley \[2007\]](#) since the estimates, although computed differently, are almost identical to the estimates of the bHP, see [\[Telschow et al., 2023\]](#).

Our second set of simulations show that the FWER control of our SuRF framework is not conservative for Gaussian data, while the traditional approach implemented in software such as SPM and FSL is conservative. In part 2 [Davenport et al. \[2023\]](#) we extend our method to non-Gaussian data and demonstrate that it accurately controls the FWER even on a gold-standard data set consisting of 7.000 resting state experiments from the UK Biobank.

4.1 Simulation Setup

In our simulations we consider the data to be samples of the Gaussian random field $\{X(v) : v \in \mathcal{V}\}$ where $\mathcal{V} \subset \mathbb{R}^D$ and the $X(v)$'s are i.i.d. $\mathcal{N}(0, 1)$ distributed. To transform X into a SuRF we smooth this discrete data by using the isotropic Gaussian kernel

$$K_f(x, v) = e^{-\frac{4 \log(2) \|x-v\|^2}{f^2}}, \quad f \in \{1, 2, \dots, 6\}, \quad (24)$$

which we parametrize by its full width at half maximum (FWHM) f as it is common in neuroimaging. The performance of different LKC estimators is compared on a standardized almost stationary SuRF and a standardized non-stationary SuRF, which we define below.

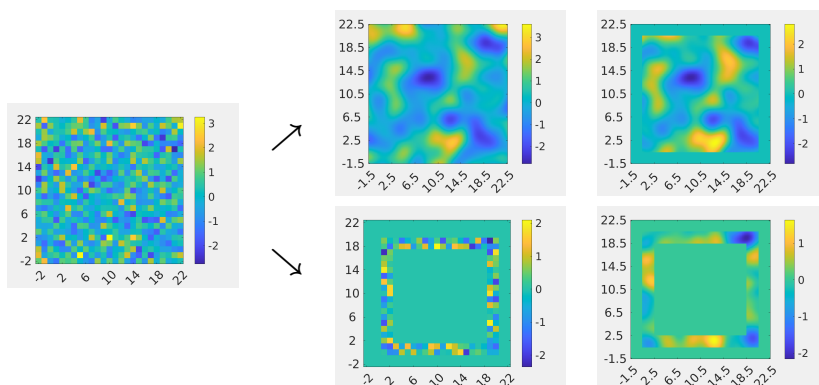


Figure 1: Illustration of generating an almost stationary or non-stationary SuRF from a white noise field on a grid using K_3 . The almost stationary field results from a convolution with the kernel K_3 before restricting the domain of the field. This circumvents boundary effects (top row). The non-stationary field (bottom row) results from first restricting to \mathcal{V}_2 and then convolving with the kernel K_3 . The edge effects produces a non-stationary field.

The advantage of starting from the field X which is i.i.d. on the lattice is that we can determine the theoretical LKCs for the normalized almost stationary and the normalized non-stationary SuRF quickly with high precision on a computer since the double sum in the Riemannian metric induced by the SuRF reduces to a single sum due to the lack of correlation, compare Proposition 7 and equation (6).

For the almost stationary simulations, for $D \in \{1, 2, 3\}$, $a \geq 0$, we take $\mathcal{V} = \mathcal{V}_D^a \subset \mathbb{R}^D$, where $\mathcal{V}_1^a = [1 - a, 100 + a] \cap \mathbb{Z}$, $\mathcal{V}_2^a = [1 - a, 20 + a]^2 \cap \mathbb{Z}^2$ and $\mathcal{V}_3^a = [1 - a, 20 + a]^3 \cap \mathbb{Z}^3$. The almost stationary SuRF is given by $(\tilde{X}, X, K_f, \mathcal{V}_D^a)$ with $a = \sqrt{2}f/\sqrt{\log(2)}$ and \tilde{X} where we choose $\mathcal{M}_{\mathcal{V}_D^0}$ to be the domain of \tilde{X} . We expand \mathcal{V}_D^0 by a in each direction and restrict \tilde{X} to the voxel

manifold $\mathcal{M}_{\mathcal{V}_D^0}$ to remove boundary effects which allows a comparison with LKC estimators for stationary fields. We call this SuRF almost stationary because it is a stationary field on \mathcal{V}_D^0 , but non-stationary on $\mathcal{M}_{\mathcal{V}_D^0}$. However, for f larger than ≈ 2 the LKCs of this field are almost identical to the LKCs of a stationary, unit variance Gaussian random field defined on $\mathcal{M}_{\mathcal{V}_D^0}$ with the covariance function $c(s, s') = K_f(s, s')$ with $s, s' \in \mathcal{M}_{\mathcal{V}_D^0}$. This can be verified with the RFTtoolbox [Davenport and Telschow \[2023\]](#) as the theoretical LKCs of such fields can be approximated with high precision, see [Appendix A.4](#), and is also supported by our observation in [Davenport et al. \[2023\]](#) that the SuRF LKC estimators yield precise FWHM estimates even at $f \approx 2.5$ where state-of-the-art methods are biased. The LKCs for stationary, unit-variance random fields over convex domains are well known [Worsley et al. \[1996\]](#) and smoothing white noise on a grid with a Gaussian kernel is the typical way that LKC estimators and the FWER have been validated in the past [[Nichols and Hayasaka, 2003](#), [Hayasaka and Nichols, 2003](#), [Taylor et al., 2007](#)]. As data in practice is non-stationary, we consider also simulations involving non-stationarity SuRFs. We simulate them by deliberately not correcting for boundary effects when smoothing the white noise field on the grid, i.e., we use $\mathcal{V}_D = \mathcal{V}_D^0$ for $D \in \{1, 2, 3\}$ with

$$\begin{aligned}\mathcal{V}_1 &= ([1, 100] \cap \mathbb{Z}) \setminus \{2, 4, 8, 9, 11, 15, 20, 21, 22, 40, \dots, 45, 60, 62, 64, 65, 98, \dots, 100\} \\ \mathcal{V}_2 &= \{x \in \mathbb{R}^2 \mid x_1 \in \{1, 2, 19, 20\} \vee x_2 \in \{1, 2, 19, 20\}\} \cap [1, 20]^2 \\ \mathcal{V}_3 &= \{x \in \mathbb{R}^3 \mid x_1 \in \{1, 2, 19, 20\} \vee x_2 \in \{1, 2, 19, 20\} \vee x_3 \in \{1, 2, 19, 20\}\} \cap [1, 20]^3\end{aligned}$$

and use $\mathcal{M}_{\mathcal{V}_D}$ as the domain of the SuRFs. The boundary effect produces a non-stationary SuRF as the weighted average is over a variable number of voxels depending on $s \in \mathcal{M}_{\mathcal{V}_D}$. An illustration of the considered sample fields for $D = 2$ is illustrated in [Figure 1](#).

In each considered simulation settings, given a sample size $N \in \mathbb{N}$, we generate SuRFs $\tilde{X}_1, \dots, \tilde{X}_N$ of SuRFs from $X_1, \dots, X_N \sim X$ as described above.

4.2 Results of the LKC Estimation

For resolutions $r \in \{1, 3, 5\}$ and $D = 2$ we compare the SuRF LKC estimator, see [Section 3.5](#), to the HP, bHP, Kiebel and Forman estimator obtained from samples of SuRFs evaluated on the grids with added resolution r . The results for $D = 1, 2$ are qualitatively similar, see [Appendix A](#). In each setting, we run 1000 simulations in which we generate $N \in \{20, 50, 100\}$ SuRFs, compare [Section 4.1](#), and estimate the LKCs from these fields.

[Figure 2](#) shows boxplots of the LKC estimates for $f = 3$ and varying sample sizes $N \in \{20, 50, 100\}$ in the almost stationary setting. [Figure 3](#) contains the same results for the non-stationary setting. At all resolutions the SuRF estimator seems to be unbiased and has a lower variance than the other estimators. Only the bHP estimator is comparable efficient, however, it has a small bias at resolution $r = 1$. The HP estimator has a similar bias and a much larger variance, compare also [Telschow et al. \[2023\]](#). The Kiebel and Forman estimators are biased for our non-stationary SuRF example and the almost stationary SuRF for the small value $f = 3$ which is typical in neuroimaging. The latter is known in the literature, see e.g., [Kiebel et al. \[1999\]](#). The dependence of the LKC estimates on the smoothing bandwidth f for $D = 2$ can be found in [Figures 10-13](#) in [Appendix A](#). Here only the SuRF estimator correctly estimates the LKCs for all $f \in \{1, \dots, 6\}$. Moreover, only in the case $f = 1$ a resolution increase of $r \geq 3$ is necessary to have unbiased estimates. Remarkably, even for FWHM $f = 2$ a resolution increase of $r = 1$ seems to be sufficient for unbiased estimation using the SuRF estimator. Additionally, the SuRF estimator is 10 times faster to compute than its only reliable competitor the bHP estimator, see [Table 1](#). Here we compared the average computation time of the SuRF, the

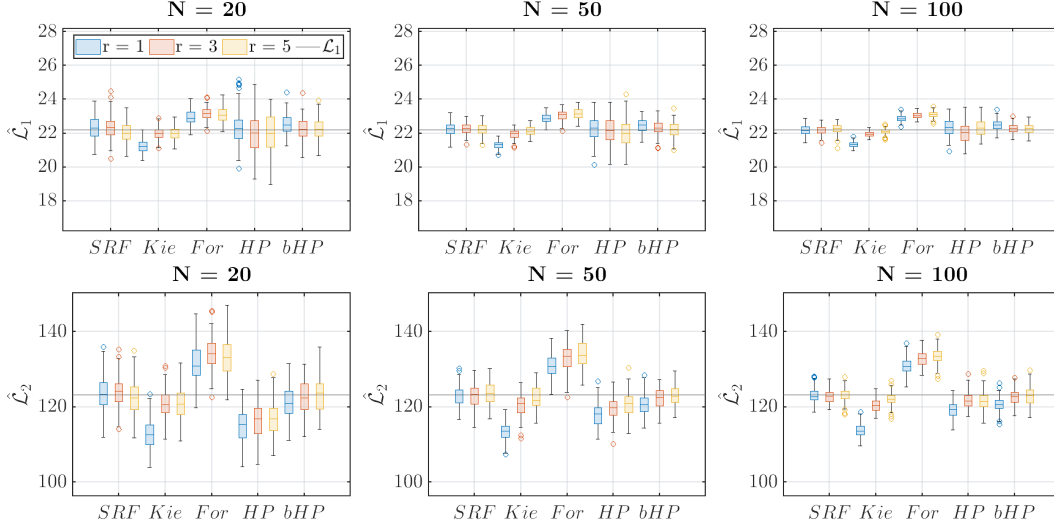


Figure 2: 2D Simulation results for estimation of the LKCs of the almost stationary SuRF described in Section 4.1. The smoothing bandwidth is $f = 3$.

bHPE and the Kiebel estimator on the stationary box example with $f = 3$ and $N = 100$ at different added resolution.

4.3 Results of the FWER Simulation

We now verify that our SuRF framework yields a non-conservative control of the FWER. To do so we determine the FWER of the one-sample t -test for a sample of Gaussian SuRFs generated as in Section 4.1 using the methodology described in Section 3.6. In each simulation setting, for $1 \leq b \leq B$ and $N \in \{20, 50, 100\}$ we obtain t -fields $T_{N,b,r}$ of resolution $r \in \{0, 1, \infty\}$. Here $r = 0$ corresponds to the traditional RFT approach, i.e., $T_{N,b,0}$ is the test statistic described in Section 3.6 evaluated on the lattice \mathcal{V} on which the original data is observed. Similarly, the case $r = 1$ corresponds to $T_{N,b,1}$ being the test statistic evaluated on $\mathcal{M}_{\mathcal{V}}^{(1)}$, compare (16). The case $r = \infty$ means the test statistic $T_{N,b,\infty}$ is a SuRF defined on $\mathcal{M}_{\mathcal{V}}$. We evaluate the FWER in this case by using numerical optimization (in particular sequential quadratic programming, Nocedal and Wright [2006]), initialized at the largest peaks of $T_{N,b,1}$ to find the global maximum of $T_{N,b,\infty}$ over $\mathcal{M}_{\mathcal{V}}$. The LKCs are estimated as described in Section 3.5 using added resolution $r = 1$ which is justified by Section 4.2. The threshold $\hat{u}_{N,b}$ which controls the FWER at a level $\alpha = 0.05$ is obtained as described in Section 3.6. For $r \in \{0, 1, \infty\}$ and $\mathcal{M}_{\mathcal{V}}^{(0)} = \mathcal{V}$ and

r	SuRF			bHPE			Kiebel		
	1	3	5	1	3	5	1	3	5
$D = 1$	0.06	0.05	0.05	7.01	13.35	16.13	4	0.03	0.04
$D = 2$	0.28	0.66	1.66	19.96	30.67	46.67	0.11	0.42	0.97
$D = 3$	18.22	80.45	239.30	196.44	-	-	8.24	47.90	151.75

Table 1: Computation time of LKC estimators in the stationary box example ($N = 100$, $f = 3$). We show averages in seconds of 100 runs of the estimators. The times for resolution increases beyond $r = 1$ and $D = 3$ of the bHPE is not reported as they are very long.

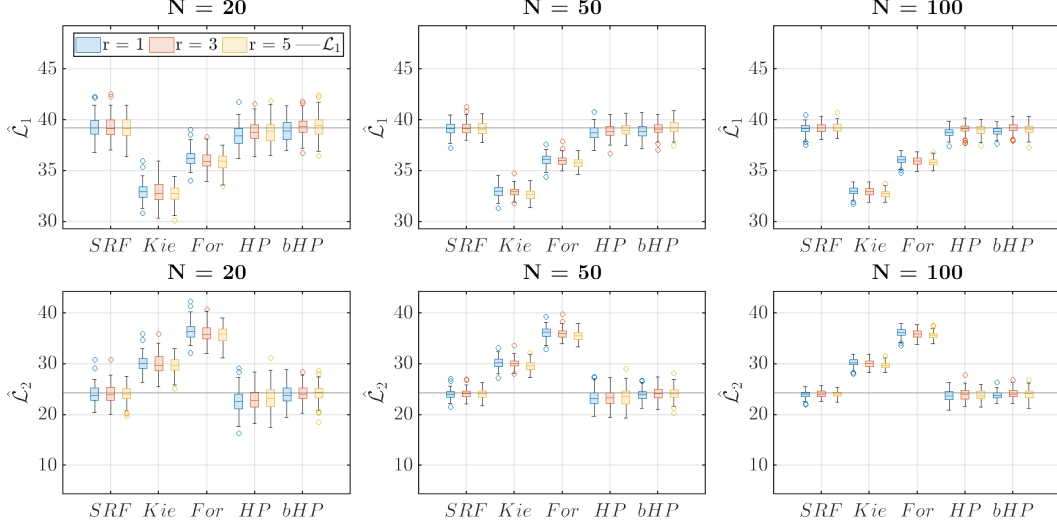


Figure 3: 2D Simulation results for estimation of the LKCs of the non-stationary SuRF described in Section 4.1. The smoothing bandwidth is $f = 3$.

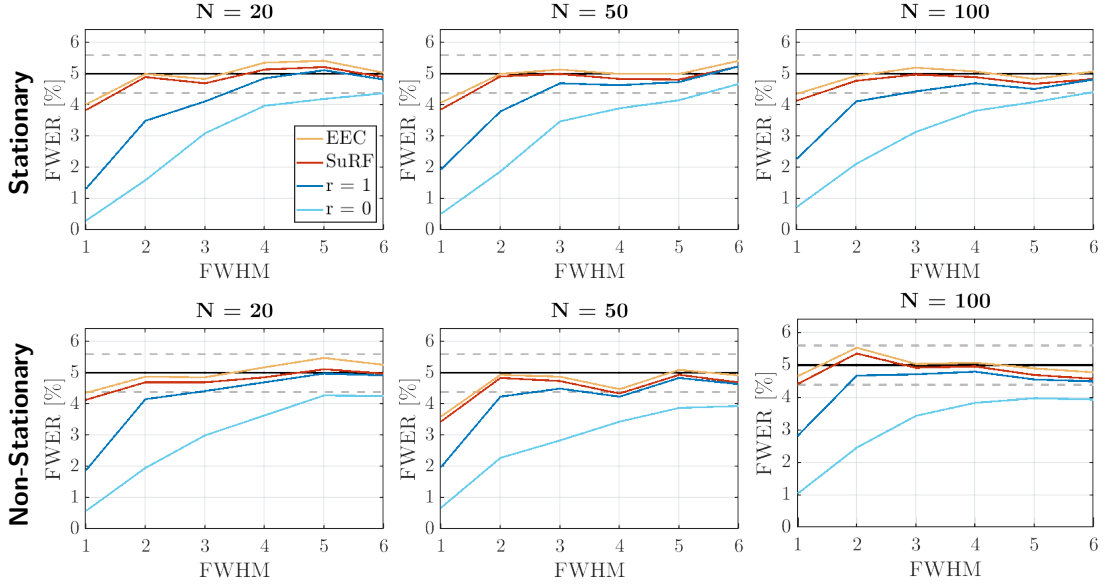


Figure 4: FWER results for the almost-stationary (top row) and non-stationary (bottom row) settings for $D = 2$.

$\mathcal{M}_\nu^{(\infty)} = \mathcal{M}_\nu$, the FWER is then estimated by evaluating

$$\frac{1}{B} \sum_{b=1}^B \mathbb{1} \left[\sup_{s \in \mathcal{M}_\nu^{(r)}} T_{N,b,r}(s) > \hat{u}_{N,b} \right],$$

In each simulation we also count the number of local maxima $l_{N,b,r}$ of $T_{N,b,r}$ on $\mathcal{M}_\nu^{(r)}$ exceeding the level $\hat{u}_{N,b}$ as it is a good approximation of the EC of the excursion set for $\alpha \approx 0.05$. The resulting estimate $\widehat{\text{EEC}} = \frac{1}{B} \sum_{b=1}^B l_{N,b,r}$ is plotted in yellow in our figures. The fact, that $\widehat{\text{EEC}}$

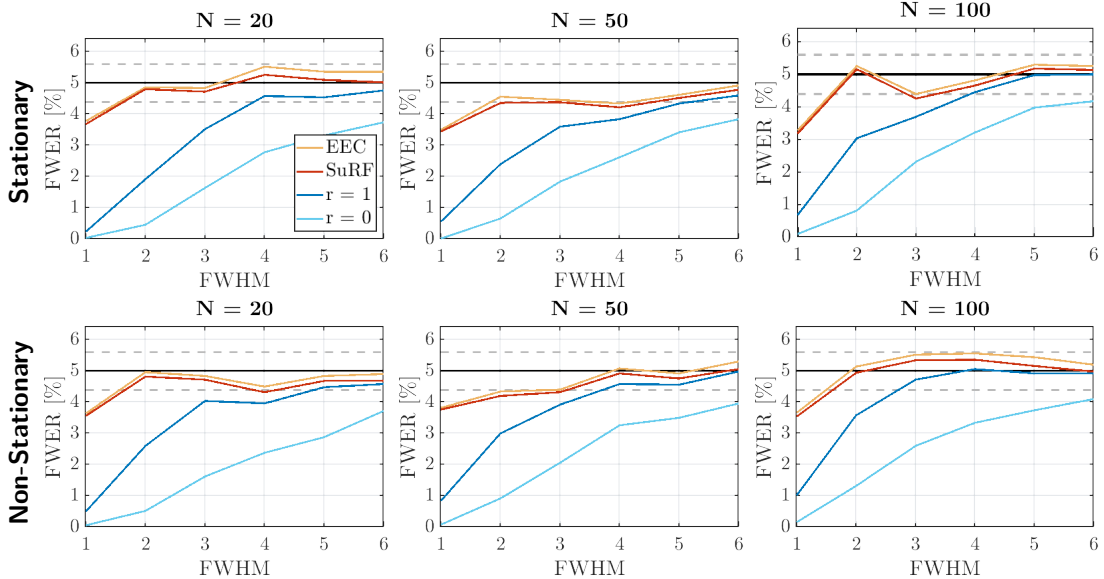


Figure 5: FWER results for the almost-stationary (top row) and non-stationary (bottom row) settings for $D = 3$.

is close to the FWER obtained for $r = \infty$, is a good indicator that the EEC heuristic used in 3.6 to estimate $\hat{u}_{N,b}$ is valid.

The results of our simulations for $D = 2, 3$ are shown in Figures 4 and 5 respectively. They reproduce the well-known observation that the traditional ($r = 0$) approach is conservative. This is more severe at low smoothness levels, but even at FWHM $f = 6$, evaluating the random fields on the original lattice yields a conservative FWER. This effect is slightly more pronounced in 3D. Moving from the original ($r = 0$) lattice to the resolution 1 lattice already reduces the conservativeness which demonstrates that the main cause of the conservativeness is the mismatch between the discreteness of the data and modeling it as a random field over a manifold. For $r = \infty$ the FWER is close to the nominal level $\alpha = 0.05$ and only slightly smaller than the estimated EEC. The less accurate FWER for FWHM $f = 1$ could be partially caused by the biased LKC estimates as we used added resolution 1, compare Figures 10-13 in Appendix A.

5 Discussion

In this article we have shown how to resolve the conservativeness of voxelwise inference using RFT (Nichols and Hayasaka [2003], Taylor et al. [2007], Eklund et al. [2016]). Our solution is inspired by the rigorous distinction between data of an experiment and atoms of a probabilistic model, which helps to identify the main problems of traditional RFT for Gaussian data: (i) the test statistic is evaluated only on a discrete set given by the data although the atoms of RFT are random fields over a WS manifold and (ii) continuous quantities are replaced by discrete approximations. Here we proposed using kernel smoothers as ferrymen transferring discrete data into random fields over a WS manifold (the atoms of RFT) and showed in simulations that this view enables accurate control of the FWER at a given significance level. Although our SuRF methodology is tailored to Gaussian related fields, this assumption can be relaxed. As discussed in Nardi et al. [2008], Telschow and Schwartzman [2022] the GKF approximates

the EEC of the excursion sets of the test statistic \tilde{T} well, if \tilde{T} only is asymptotically Gaussian. Because the SuRF LKC estimates are consistent so long as derivatives of the sample covariance of the residuals converge uniformly to the derivatives of the covariance function of the limiting field, compare Telschow et al. [2023], our SuRF methodology remains asymptotically valid even under non-Gaussianity. However, as the sample size required to deal with the non-Gaussianity of fMRI data is large, we extend in Part 2, i.e., Davenport et al. [2023], our SuRF based voxelwise inference using RFT to non-Gaussian data and demonstrate its non-conservativeness using a large resting state validation.

The importance of our work for neuroimaging is twofold. Firstly, our GKF based method is computationally faster than resampling based inference such as permutation tests which control the FWER at level α over the grid \mathcal{V} at the cost of a high computational burden. Secondly, solving the conservativeness that has long caused power problems for voxelwise inference using RFT is a first step towards identifying and solving the problems of false positive rates in cluster-size inference (Eklund et al. [2016]) as it also relies on the GKF and applies continuous theory to smoothed fields evaluated on the voxel lattice [Friston et al., 1994].

As the estimator for \mathcal{L}_1 in 3D using Theorem 6 is difficult to implement, we proposed a local stationary approximation which consists of the first integral in (40). Even if the fields are highly non-stationary using this approximation does not have a large effect on voxelwise inference as the estimate \hat{u}_α from the EEC is primarily driven by $\hat{\mathcal{L}}_2$ and $\hat{\mathcal{L}}_3$. This can be seen for example for real fMRI data using the supplementary material of Telschow et al. [2023]. Here $u_{0.95} \approx 4.2$ which is typical for neuroimaging data. Thus, $\rho_3^{\tilde{T}}(u_\alpha)/\rho_1^{\tilde{T}}(u_\alpha) \approx 2.6$ and $\rho_2^{\tilde{T}}(u_\alpha)/\rho_1^{\tilde{T}}(u_\alpha) \approx 1.6$ for sample size 50. Moreover, typically $\mathcal{L}_1 \ll \mathcal{L}_3$. To obtain intuition on why this holds, consider the case where the atoms arise as stationary random fields with the square exponential covariance function with bandwidth parameter h over a convex WS manifold \mathcal{M} . In this case \mathcal{L}_3 is the volume of \mathcal{M} divided by h^3 , \mathcal{L}_2 is half the surface area of \mathcal{M} divided by h^2 and \mathcal{L}_1 is twice the diameter of \mathcal{M} divided by h [Worsley et al., Table 2].⁸ That the local stationary approximation of \mathcal{L}_1 does not influence the false positive rate can additionally be seen from Figure 5 and our simulations in Part 2.

The careful distinction between data and atoms and the practical problems (i) and (ii) are relevant in a number of further applications. For example, any functional data method involving smoothing via basis functions or kernel smoothers, and for which the coverage of simultaneous confidence bands or the family-wise error rate of tests is reported, can benefit from our SuRF reasoning. A concrete example is Davenport et al. [2022]. Here confidence regions for peaks of the signal of random fields over bounded open domains of \mathbb{R}^D are developed and convolution fields are used to localize peaks of activation in fMRI and MEG. In fact, MEG is a natural domain in which our SuRF reasoning applies, because the power spectrum is a convolution field, see the Supplementary material of Davenport et al. [2022] for details. Another potential application of the SuRF reasoning are coverage probability excursion (CoPE) sets. CoPE sets provide confidence sets for the excursion above a value $c \in \mathbb{R}$ of a real-valued target function defined over a domain in \mathbb{R}^D , $D > 0$, from noisy data, [Sommerfeld et al., 2018, Bowring et al., 2019, 2021, Maullin-Sapey et al., 2023]. These papers found in simulations that the empirical coverage of CoPE sets is larger than the specified coverage, but converges to the correct coverage probability as the domain is sufficiently densely sampled. Theoretically, this has been explained in Theorem 1.b) from [Sommerfeld et al., 2018] and is illustrated in Figure 3 of Bowring et al.

⁸Note that in Table 2 the FWHM needs to be transformed into a bandwidth by multiplication with $\sqrt{4\log(2)}/2\pi$ to transform resels –a concept from Worsley et al. [1996] designed for isotropic, stationary processes– into LKCs, compare our discussion in the Supplementary of Part 2.

[2019]. SuRFs provide a practical means of overcoming this overcoverage.

Acknowledgments

F.T. is funded by the Deutsche Forschungsgemeinschaft (DFG) under Excellence Strategy The Berlin Mathematics Research Center MATH+ (EXC-2046/1, project ID:390685689). F.T. and S.D. were partially supported by NIH grant R01EB026859. S.D. was partially supported by NIH grant R01MH128923. We thank Armin Schwartzman for generous funding and discussions on this topic – especially for suggesting the simplified notation (6), Henrik Schumacher for helpful discussions on Riemannian geometry and spotting that the term involving the Riemannian curvature tensor in (39) is not zero and Thomas E. Nichols for suggesting the term *Super Resolution field* (SuRF) which fits well the institution F.T. was employed at when he started this topic.

References

- Anders Eklund, Thomas E Nichols, and Hans Knutsson. Cluster failure: Why fMRI inferences for spatial extent have inflated false-positive rates. *Proceedings of the national academy of sciences*, 113(28):7900–7905, 2016.
- Russell Poldrack and Thomas E. Nichols. *Handbook of functional MRI data analysis*, volume 4. 2011.
- K. J. Worsley et al. A three-dimensional statistical analysis for CBF activation studies in human brain. *Journal of cerebral blood flow and metabolism.*, 12(6):900–18, 1992.
- Karl Friston et al. Assessing the significance of focal activations using their spatial extent. *Human Brain Mapping*, 1:214–220, 1994.
- Keith J Worsley et al. A unified statistical approach for determining significant signals in images of cerebral activation. *Human brain mapping*, 4(1):58–73, 1996.
- Jonathan Taylor. A Gaussian kinematic formula. *The Annals of Probability*, 34(1):122–158, 2006.
- Jonathan Taylor, Akimichi Takemura, and Robert J. Adler. Validity of the expected Euler characteristic heuristic. *Annals of Probability*, 33(4):1362–1396, 2005.
- K.J. Friston, John T Ashburner, Stefan J Kiebel, Thomas E. Nichols, and William D Penny. *Statistical Parametric Mapping*.
- Justin R Chumbley and Karl J Friston. False discovery rate revisited: FDR and topological inference using Gaussian random fields. *Neuroimage*, 44(1):62–70, 2009.
- Armin Schwartzman and Fabian Telschow. Peak p-values and false discovery rate inference in neuroimaging. *NeuroImage*, 197:402–413, 2019.
- Thomas E. Nichols and Satoru Hayasaka. Controlling the familywise error rate in functional neuroimaging: A comparative review. *Statistical Methods in Medical Research*, 12(5):419–446, 2003.

- Thomas E Nichols and Andrew P Holmes. Nonparametric permutation tests for functional neuroimaging: a primer with examples. *Human brain mapping*, 15(1):1–25, 2002.
- Anderson M. Winkler et al. Non-parametric combination and related permutation tests for neuroimaging. *Human Brain Mapping*, 37(4):1486–1511, 2016a.
- Anderson M. Winkler et al. Faster permutation inference in brain imaging. *NeuroImage*, 141: 502–516, 2016b.
- Samuel Davenport et al. Robust FWER control in neuroimaging using Random Field Theory: Riding the SuRF to continuous land - Part 2. *arXiv preprint arXiv:2312.10849*, 2023.
- Alfaro-Almagro et al. Image processing and quality control for the first 10,000 brain imaging datasets from uk biobank. *Neuroimage*, 166:400–424, 2018.
- Haonan Wang and JS Marron. Object oriented data analysis: Sets of trees. *The Annals of Statistics*, 35(5):1849–1873, 2007.
- J Steve Marron and Andrés M Alonso. Overview of object oriented data analysis. *Biometrical Journal*, 56(5):732–753, 2014.
- K. J. Worsley. An improved theoretical P value for SPMs based on discrete local maxima. *NeuroImage*, 28(4):1056–1062, 2005.
- J. E. Taylor, K. J. Worsley, and F. Gosselin. Maxima of discretely sampled random fields, with an application to 'bubbles'. *Biometrika*, 94(1):1–18, 2007.
- Steven D. Forman et al. Improved Assessment of Significant Activation in Functional Magnetic Resonance Imaging (fMRI): Use of a Cluster-Size Threshold. *Magnetic Resonance in Medicine*, 33(5):636–647, 1995.
- Stefan J. Kiebel et al. Robust Smoothness Estimation in Statistical Parametric Maps Using Standardized Residuals from the General Linear Model. *NeuroImage*, 10(6):756–766, 1999.
- Jonathan E Taylor and Keith J. Worsley. Detecting Sparse Signals in Random Fields, With an Application to Brain Mapping. *Journal of the American Statistical Association*, 102(479): 913–928, 2007.
- Fabian JE Telschow et al. Estimation of expected Euler characteristic curves of nonstationary smooth random fields. *Ann. Statist.*, 51(5):2272–2297, 2023.
- Nicole Lazar. *The statistical analysis of functional MRI data*. Springer Science & Business Media, New York, 2008.
- Samuel Davenport and Fabian Telschow. RFTtoolbox, 2023. URL <https://github.com/sjdavenport/RFTtoolbox>.
- Robert J Adler and Jonathan E Taylor. *Random Fields and Geometry*. Springer Science & Business Media, New York, 2009.
- George Turin. An introduction to matched filters. *IRE transactions on Information theory*, 6(3):311–329, 1960.

- K. J. Worsley, C.H. Liao, J. Aston, V. Petre, G.H. Duncan, F. Morales, and A.C. Evans. A General Statistical Analysis for fMRI Data. *NeuroImage*, 15(1):1–15, 2002.
- Samuel Davenport and Fabian JE Telschow. On the finiteness of second moments of the number of critical points of Gaussian random fields. *arXiv preprint arXiv:2201.01591*, 2022.
- Keith J Worsley. Local maxima and the expected Euler characteristic of excursion sets of χ^2 , F and t fields. *Advances in Applied Probability*, 26(1):13–42, 1994.
- J. E. Taylor and K. J. Worsley. Random fields of multivariate test statistics, with applications to shape analysis. *Annals of Statistics*, 36(1):1–27, 2008.
- Satoru Hayasaka and Thomas E. Nichols. Validating cluster size inference: Random field and permutation methods. *NeuroImage*, 20(4):2343–2356, 2003.
- Jorge Nocedal and Stephen J Wright. Quadratic programming. *Numerical optimization*, pages 448–492, 2006.
- Yuval Nardi, David O Siegmund, and Benjamin Yakir. The distribution of maxima of approximately Gaussian random fields. 2008.
- Fabian JE Telschow and Armin Schwartzman. Simultaneous confidence bands for functional data using the Gaussian kinematic formula. *Journal of Statistical Planning and Inference*, 216:70–94, 2022.
- K. J. Worsley, Jonathan E. Taylor, Francesco Tomaiuolo, and Jason Lerch. *NeuroImage*, pages 189–195.
- Samuel Davenport, Thomas E Nichols, and Armin Schwarzman. Confidence regions for the location of peaks of a smooth random field. *arXiv preprint arXiv:2208.00251*, 2022.
- Max Sommerfeld, Stephan Sain, and Armin Schwartzman. Confidence regions for spatial excursion sets from repeated random field observations, with an application to climate. *Journal of the American Statistical Association*, 113(523):1327–1340, 2018.
- Alexander Bowring, Fabian Telschow, Armin Schwartzman, and Thomas E Nichols. Spatial confidence sets for raw effect size images. *NeuroImage*, 203:116187, 2019.
- Alexander Bowring, Fabian JE Telschow, Armin Schwartzman, and Thomas E Nichols. Confidence sets for Cohen’s d effect size images. *NeuroImage*, 226:117477, 2021.
- T Maullin-Sapey, A Schwartzman, and TE Nichols. Spatial confidence regions for combinations of excursion sets in image analysis. *Journal of the Royal Statistical Society: Statistical Methodology Series B*, 2023.
- Jan Magnus and Heinz Neudecker. The elimination matrix: some lemmas and applications. *SIAM Journal on Algebraic Discrete Methods*, pages 422–449, 1980.
- Kantilal Varichand Mardia, John T Kent, and John M Bibby. Multivariate analysis. *Probability and mathematical statistics*, 1979.

Appendix

A Additional Figures, Simulation Results and Tables

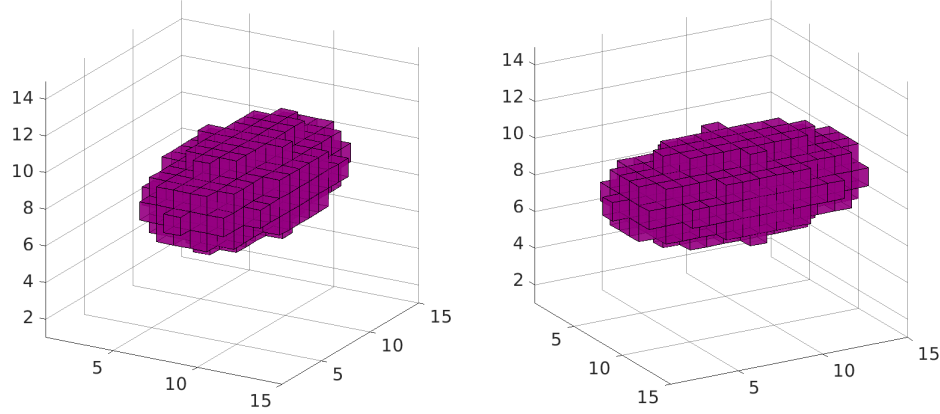


Figure 6: An example of a voxel manifold viewed from different angles.

A.1 LKC estimation for $D = 1$

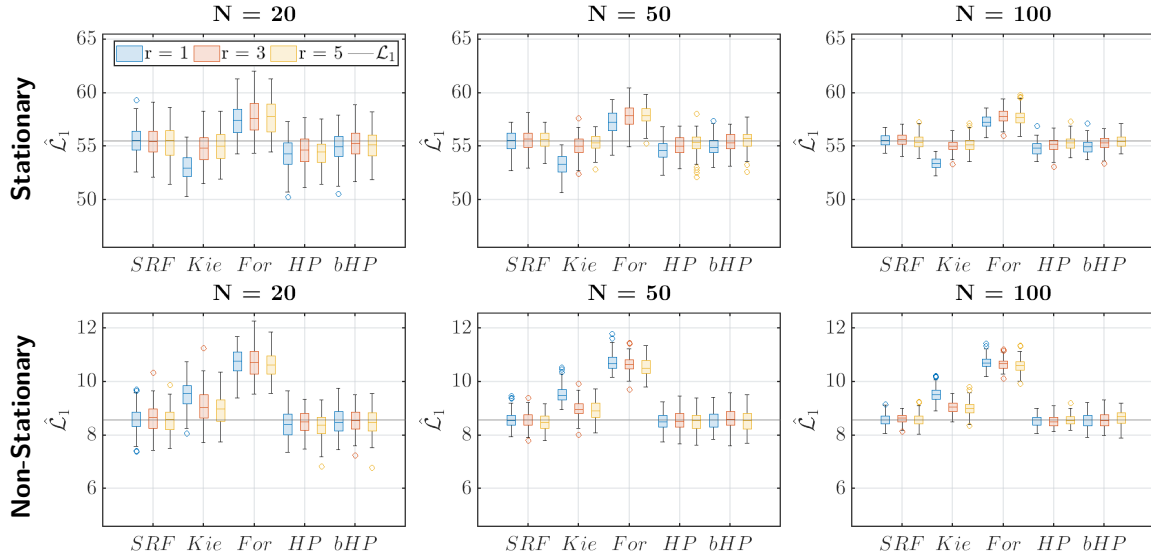


Figure 7: 1D Simulation results of estimation of the LKCs of the two SuRFs derived from the stationary box example and the non-stationary sphere example. The FWHM is $f = 3$.

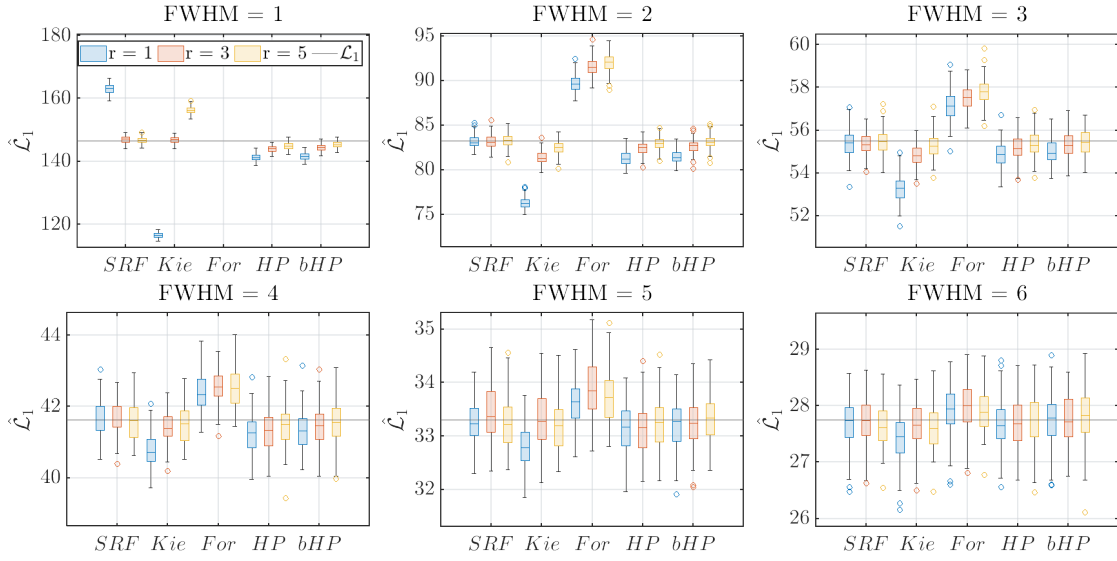


Figure 8: 1D Simulation results of estimation of the LKCs of SuRFs derived from the stationary box example. The results show the dependence of the LKC estimation on the FWHM used in the smoothing kernel for sample size $N = 100$.

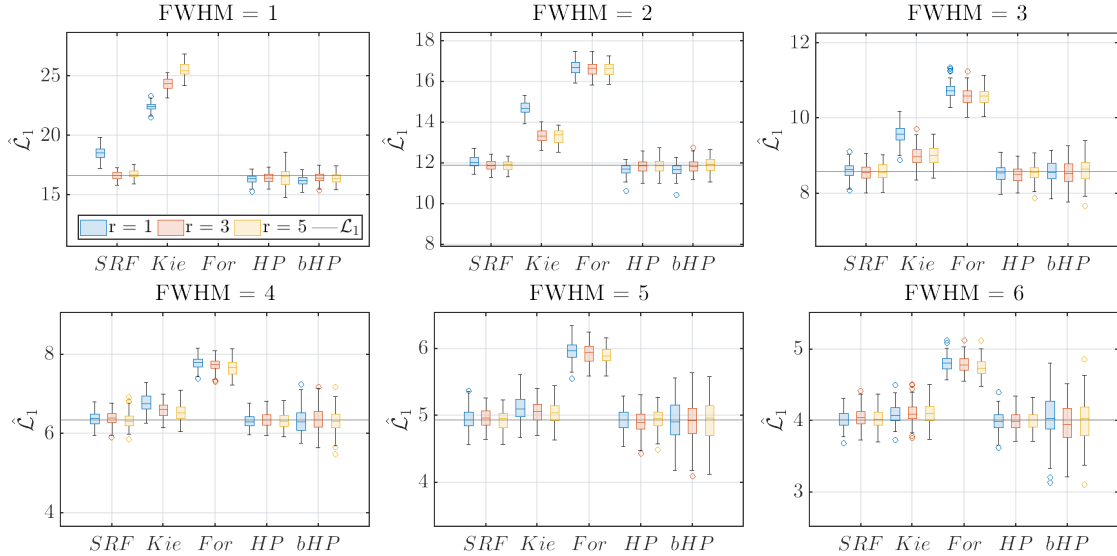


Figure 9: 1D Simulation results of estimation of the LKCs of SuRFs derived from the non-stationary sphere example. The results show the dependence of the LKC estimation on the FWHM used in the smoothing kernel for sample size $N = 100$.

A.2 LKC estimation for $D = 2$

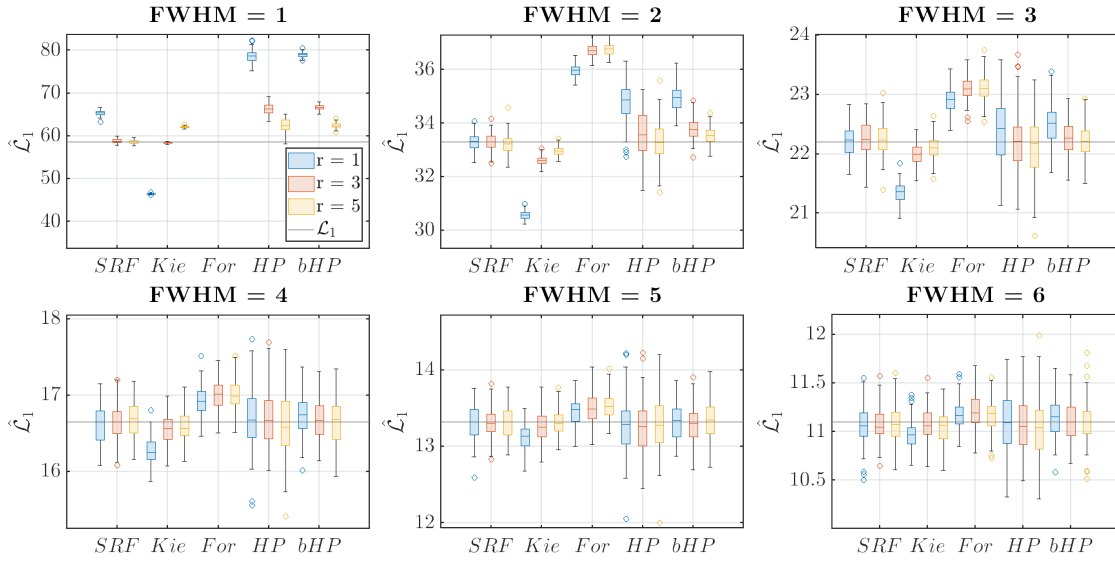


Figure 10: 2D Simulation results for estimation of the LKCs of the almost stationary SuRF described in Section 4.1. The figures show the dependence of the LKC estimation on the smoothing bandwidth f for sample size $N = 100$.

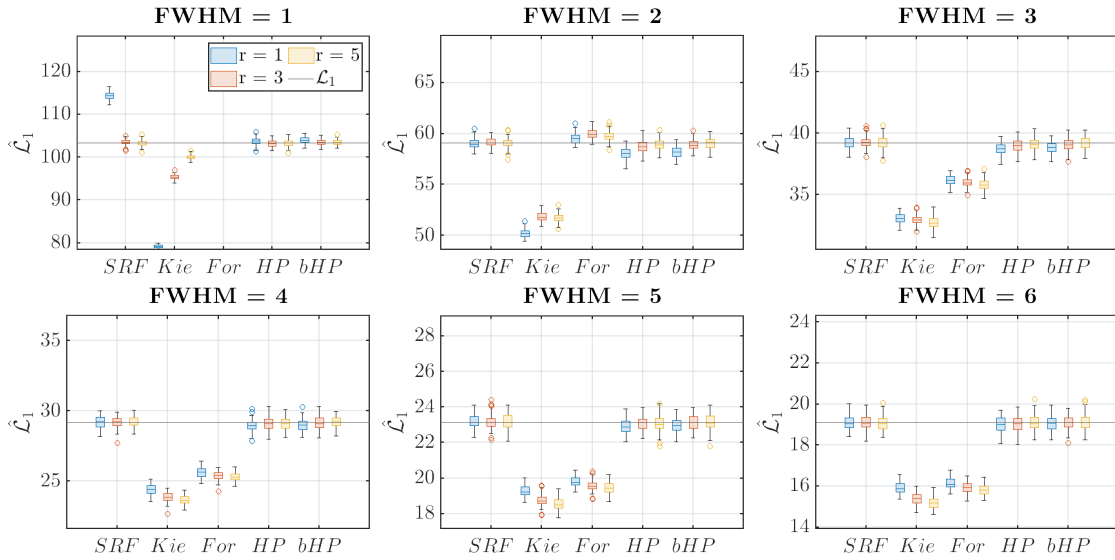


Figure 11: 2D Simulation results of estimation of the LKCs of SuRFs derived from the non-stationary sphere example. The results show the dependence of the LKC estimation on the FWHM used in the smoothing kernel for sample size $N = 100$.

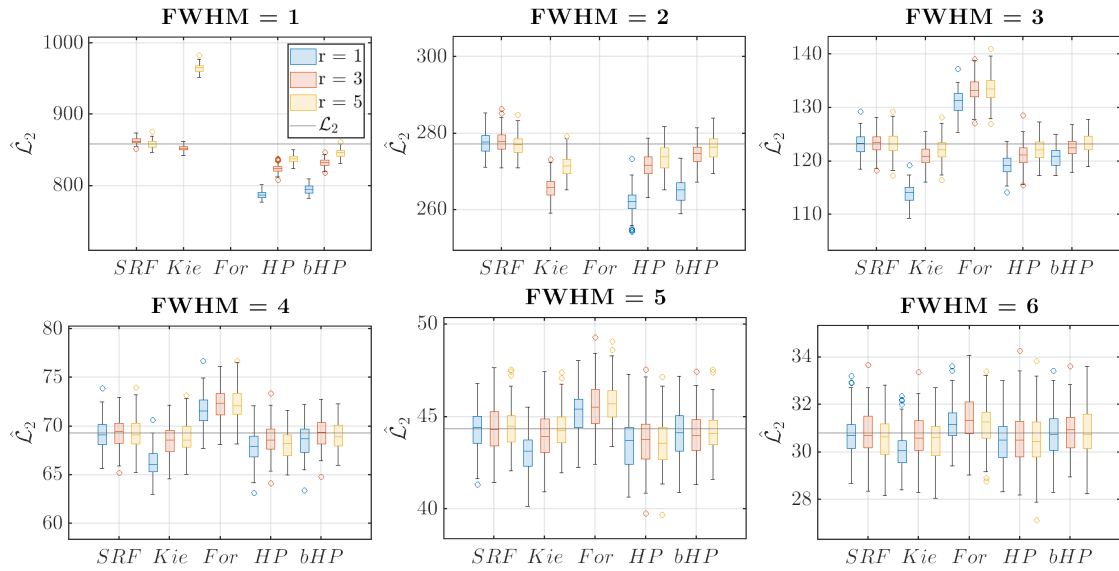


Figure 12: 2D Simulation results for estimation of the LKCs of SuRFs derived from the stationary box example. The results show the dependence of the LKC estimation on the FWHM used in the smoothing kernel for sample size $N = 100$.

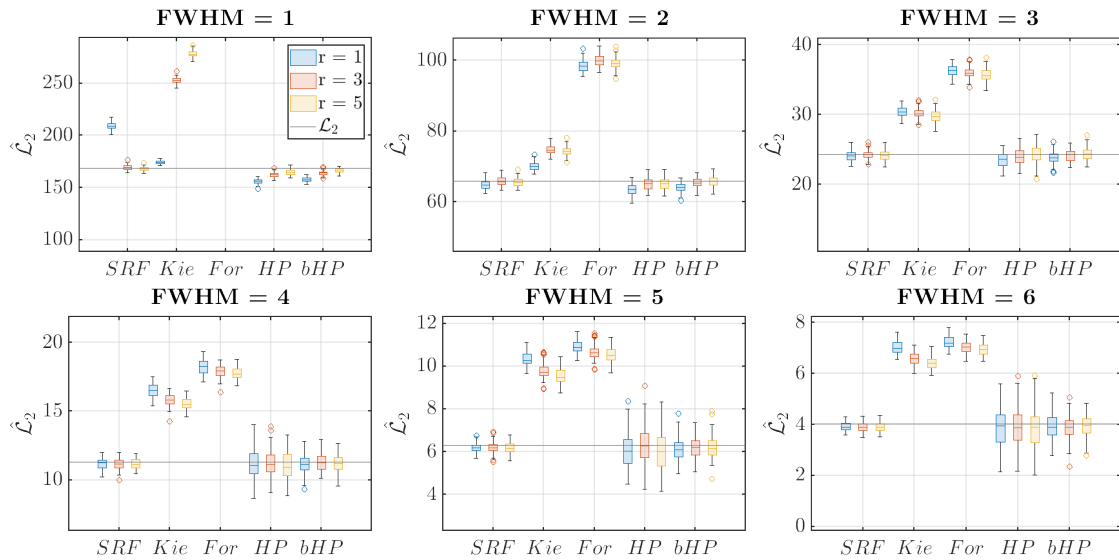


Figure 13: 2D Simulation results for the estimation of the LKCs of SuRFs in the non-stationary setting. The results show the dependence of the LKC estimation on the FWHM used in the smoothing kernel for sample size $N = 100$.

A.3 LKC estimation for $D = 3$

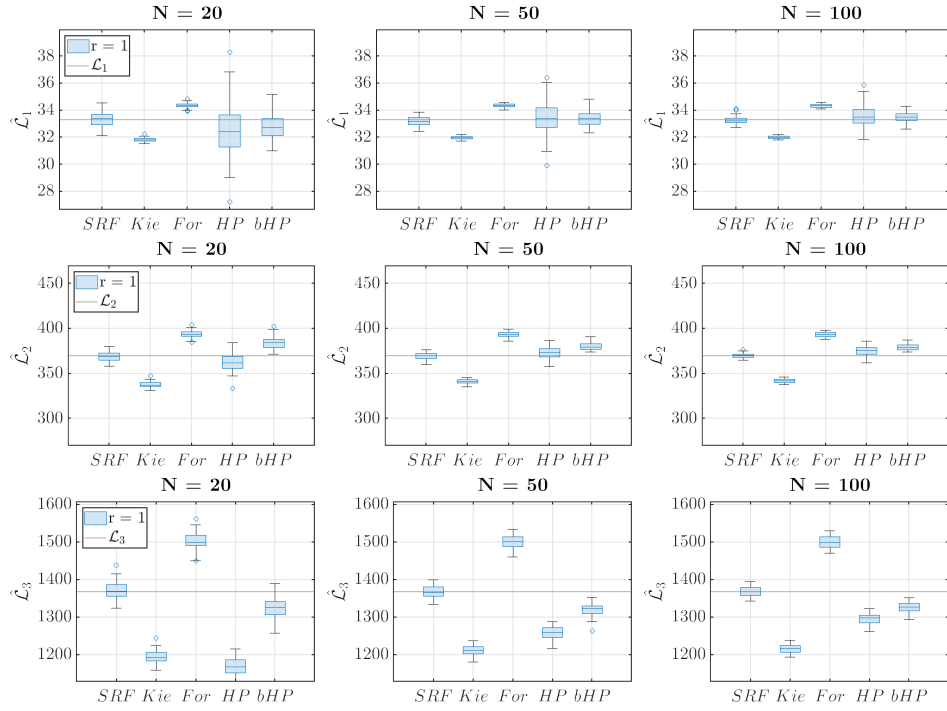


Figure 14: 3D Simulation results of estimation of the LKCs of the SuRFs derived from the stationary box example. The FWHM is $f = 3$.

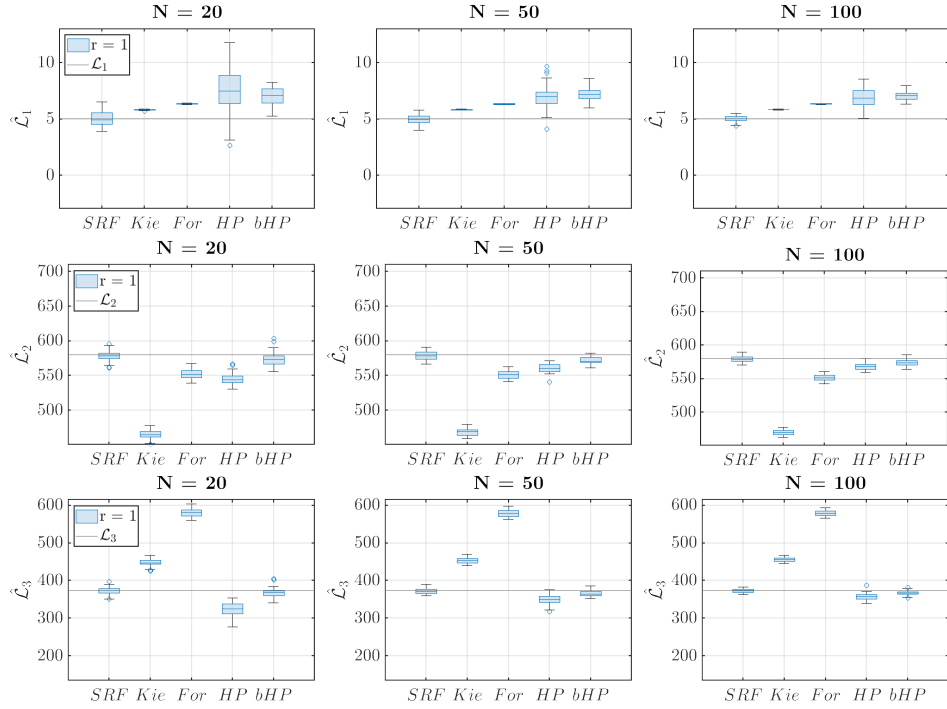


Figure 15: 3D Simulation results of estimation of the LKCs of the two SuRFs derived from the non-stationary sphere example. The FWHM is $f = 3$. Note that the theoretical value for \mathcal{L}_1 is the theoretical value for the locally stationary \mathcal{L}_1 . The true value for \mathcal{L}_1 is currently infeasible to obtain.

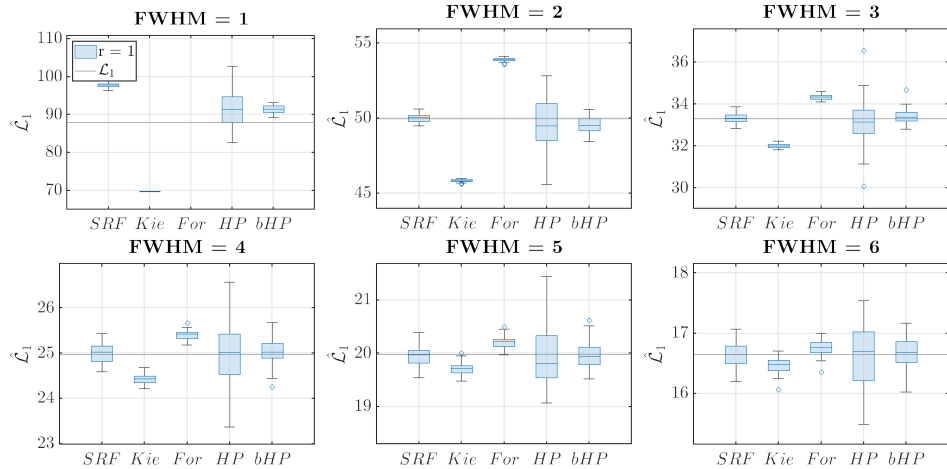


Figure 16: 3D Simulation results of estimation of the LKCs of SuRFs derived from the almost stationary box example. The results show the dependence of the LKC estimation on the FWHM used in the smoothing kernel for sample size $N = 100$.

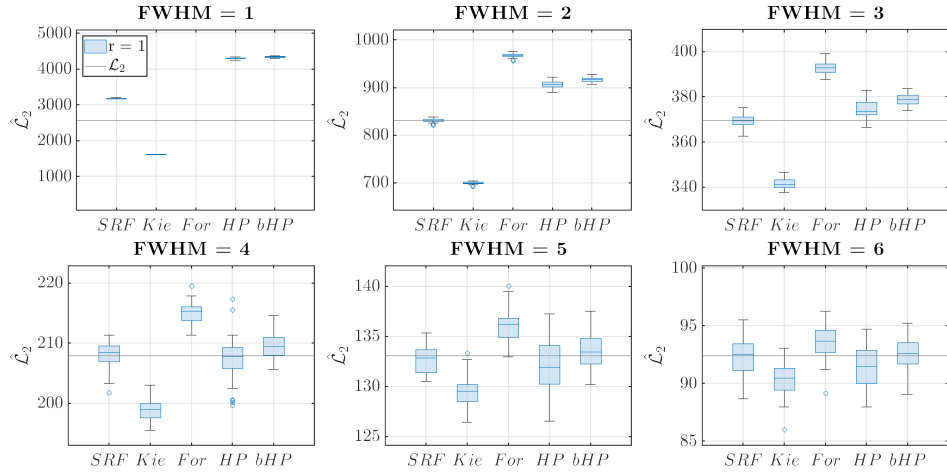


Figure 17: 3D Simulation results of estimation of the LKC of SuRFs derived from the almost stationary box example. The results show the dependence of the LKC estimation on the FWHM used in the smoothing kernel for sample size $N = 100$.

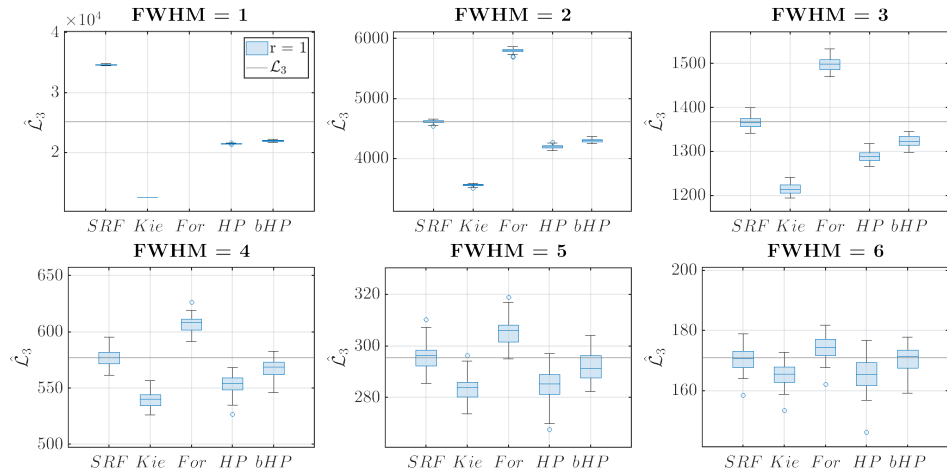


Figure 18: 3D Simulation results of estimation of the LKC of SuRFs derived from the almost-stationary sphere example. The results show the dependence of the LKC estimation on the FWHM used in the smoothing kernel for sample size $N = 100$.

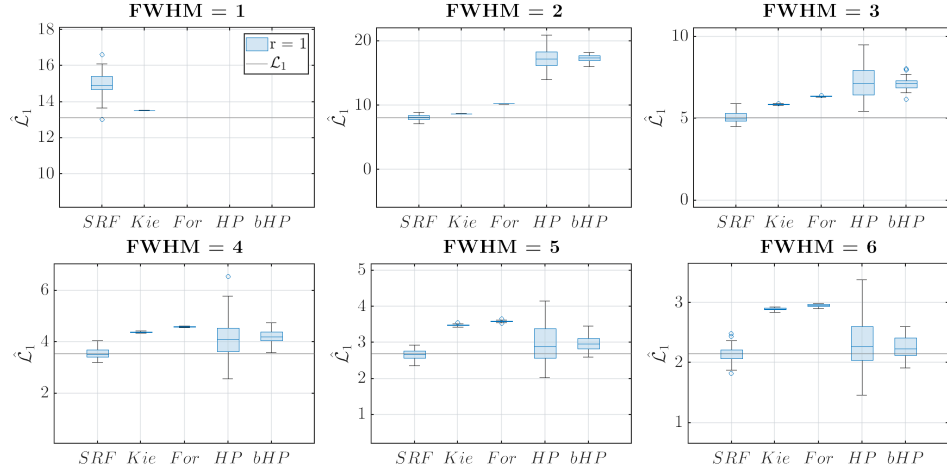


Figure 19: 3D Simulation results of estimation of the LKCs of SuRFs derived from the non-stationary sphere example. The results show the dependence of the LKC estimation on the FWHM used in the smoothing kernel for sample size $N = 100$. Note that the theoretical value for \mathcal{L}_1 is the theoretical value for the locally stationary \mathcal{L}_1 . The true value for \mathcal{L}_1 is currently infeasible to obtain.

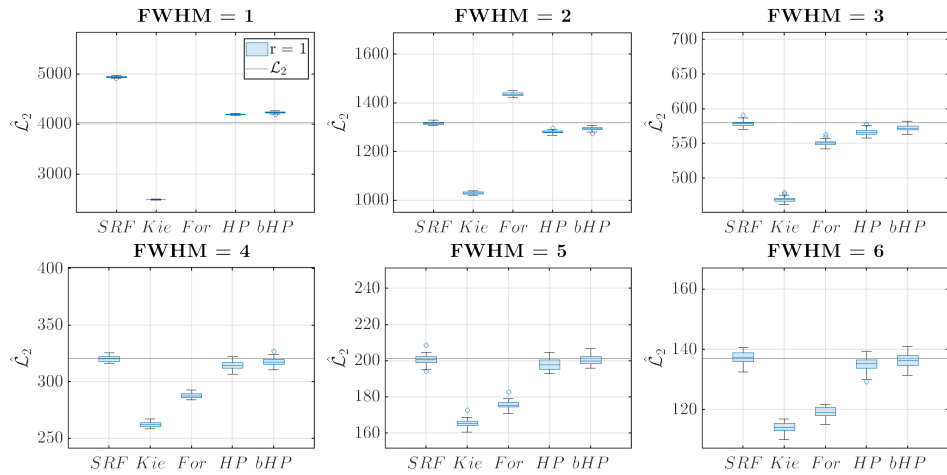


Figure 20: 3D Simulation results of estimation of the LKCs of SuRFs derived from the non-stationary sphere example. The results show the dependence of the LKC estimation on the FWHM used in the smoothing kernel for sample size $N = 100$.

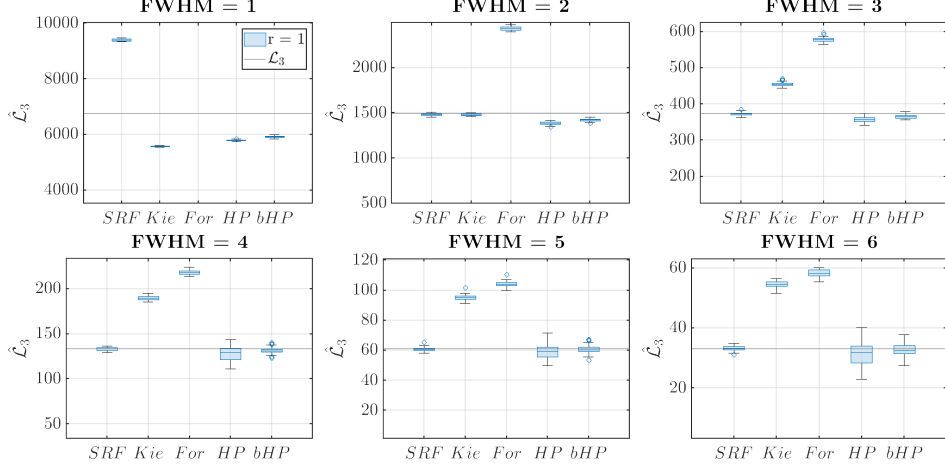


Figure 21: 3D Simulation results of estimation of the LKCs of SuRFs derived from the non-stationary sphere example. The results show the dependence of the LKC estimation on the FWHM used in the smoothing kernel for sample size $N = 100$.

A.4 Comparison of the LKCs of the Almost Stationary Box Example and its Stationary Counterpart

Here we give an example of approximating the theoretical LKCs (up to an arbitrary resolution increase to approximate the integrals) for the special case of a normalized SuRF which is derived from a random vector $(X(v) : v \in \mathcal{V})$ satisfying $X(v_1)$ being independent of $X(v_2)$ for all $v_1 \neq v_2 \in \mathcal{V}$. Because of the mutual independence of the entries of X in this case we obtain

$$\text{Cov} \left[\tilde{X}(x), \tilde{X}(x') \right] = \sum_{v \in \mathcal{V}} K(x, v) K(x', v), \quad x, x' \in \mathcal{M}_{\mathcal{V}}.$$

and thus the Riemannian metric (12) induced by the normalized SuRF of X is

$$\Lambda_{dd'}(x) = \frac{\sum_{v \in \mathcal{V}} \partial_d K(x, v) \partial_{d'} K(x, v)}{\sum_{v \in \mathcal{V}} K(x, v)^2} - \frac{\sum_{v \in \mathcal{V}} K(x, v) \partial_d K(x, v) \sum_{v \in \mathcal{V}} K(x, v) \partial_{d'} K(x, v)}{(\sum_{v \in \mathcal{V}} K(x, v)^2)^2}. \quad (25)$$

Replacing $\hat{\mathbf{\Lambda}}$ in (17) by $\mathbf{\Lambda}(x) \in \mathbb{R}^{D \times D}$ with (d, d') th entry given by (25), we can approximate the LKCs of the normalized SuRF of X up to arbitrary precision on a computer. We implemented this in the function `LKC_wncfield_theory()` from the RFTtoolbox [Davenport and Telschow \[2023\]](#).

We can use this function to demonstrate that the LKCs from the almost stationary box example derived from the Gaussian Kernel (24) for $f > 0$, are essentially the same as the LKCs of the zero-mean Gaussian field with covariance function $\mathbf{c}_f(x, y) = \exp(-4 \log(2)|x - y|^2/f^2)$ provided that f is larger than ≈ 2.5 . We denote the correlation function of the almost stationary box example with $\tilde{\mathbf{c}}_f(x, y)$.

We compare the resulting LKCs to the LKCs of the random field with covariance function

$\mathbf{c}_f(x, y)$ over a convex domain $S \subset \mathbb{R}^D$, $D \in \{1, 2, 3\}$, which are given by

$$\begin{aligned}
 D = 1: \quad \mathcal{L}_1 &= \frac{\text{vol}(S)}{\sqrt{4 \log(2)} f} \\
 D = 2: \quad \mathcal{L}_1 &= \frac{\text{vol}(\partial S)}{2\sqrt{4 \log(2)} f}, \quad \mathcal{L}_2 = \frac{\text{vol}(S)}{4 \log(2) f^2} \\
 D = 3: \quad \mathcal{L}_1 &= \frac{2 \text{Diameter}(S)}{\sqrt{4 \log(2)} f}, \quad \mathcal{L}_2 = \frac{\text{vol}(\partial S)}{2 \cdot 4 \log(2) f^2}, \quad \mathcal{L}_3 = \frac{\text{vol}(S)}{f^3 (4 \log(2))^{3/2}},
 \end{aligned}$$

compare for example [Telschow et al. \[2023\]](#) and in particular Table 2 from [Worsley et al.](#) for $D = 3$. To approximate the theoretical LKCs of the almost stationary field we use an added resolution of 11 for $D \in \{1, 2\}$ and for the sake of computation time only an added resolution of 7 for $D = 3$. The results are presented in Tables [2-4](#).

$D = 1$	f	1	1.5	2	2.5	3	3.5	4
\mathcal{L}_1	\tilde{c}_f	146.52	110.41	83.25	66.60	55.50	47.57	41.63
	c_f	166.51	111.01	83.26	66.60	55.50	47.57	41.63

Table 2: Comparison of the theoretical LKCs for different smoothing bandwidths between the almost stationary box example for $D = 1$, which has the covariance function \tilde{c}_f , and the zero-mean stationary Gaussian field having covariance \tilde{c}_f over the domains specified in Section 4.1 of the main manuscript.

$D = 2$	f	1	1.5	2	2.5	3	3.5	4
\mathcal{L}_1	\tilde{c}_f	58.61	44.16	33.30	26.64	22.20	19.03	16.65
	c_f	66.60	44.40	33.30	26.64	22.20	19.03	16.65
\mathcal{L}_2	\tilde{c}_f	858.72	487.59	277.24	177.45	123.23	90.53	69.31
	c_f	1109.00	492.90	277.26	177.45	123.23	90.53	69.31

Table 3: Comparison of the theoretical LKCs for different smoothing bandwidths between the almost stationary box example for $D = 2$, which has the covariance function \tilde{c}_f , and the zero-mean stationary Gaussian field having covariance \tilde{c}_f over the domains specified in Section 4.1 of the main manuscript.

$D = 3$	f	1	1.5	2	2.5	3	3.5	4
\mathcal{L}_1	\tilde{c}_f	87.91	66.24	49.95	39.96	33.30	28.54	24.98
	c_f	99.91	66.60	49.95	39.96	33.30	28.54	24.98
\mathcal{L}_2	\tilde{c}_f	2576.13	1462.77	831.72	532.34	369.68	271.60	207.94
	c_f	3327.11	1478.71	831.78	532.34	369.68	271.6	207.94
\mathcal{L}_3	\tilde{c}_f	25163.37	10766.66	4616.20	2363.73	1367.90	861.42	577.08
	c_f	36933.30	10943.20	4616.66	2363.73	1367.90	861.42	577.08

Table 4: Comparison of the theoretical LKCs for different smoothing bandwidths between the almost stationary box example for $D = 3$, which has the covariance function \tilde{c}_f , and the zero-mean stationary Gaussian field having covariance \tilde{c}_f over the domains specified in Section 4.1 of the main manuscript.

B LKCs induced by a normalized field

B.1 Induced Riemannian metric of a normalized random field

The most important quantity for the Gaussian Kinematic formula is the Riemannian metric induced by a random field. It is the backbone of the GKF for Gaussian related fields developed in Taylor [2006].

In this section f denotes a zero-mean random field with almost surely continuously, differentiable sample paths over the domain $\overline{\mathcal{M}}$ and we call the random field $f/\sqrt{\text{Var}[f]}$ the normalized field derived from f . Recall that a vector field $V \in \mathcal{T}\overline{\mathcal{M}}$ can be interpreted as a first order differential operator, i.e., for all $h \in C^1(\overline{\mathcal{M}})$ the expression $Vh : \overline{\mathcal{M}} \rightarrow \mathbb{R}, s \mapsto (Vh)(s)$ defines a function in $C(\overline{\mathcal{M}})$. This can be made precise by taking a local chart $\varphi : \overline{\mathcal{M}} \supseteq \mathcal{U} \rightarrow \varphi(\mathcal{U}) = \mathcal{W} \subset \mathbb{R}^D$ of $\overline{\mathcal{M}}$ with inverse $\psi = \varphi^{-1}$. The vector field V in local coordinates (\mathcal{U}, φ) can be written as

$$V = \sum_{d=1}^D V_d \partial_d, \quad V_1, \dots, V_D \in C(\mathcal{W}) \quad (26)$$

where ∂_d is the vector field on \mathcal{W} defined by

$$\partial_d(h \circ \psi)(x) = \frac{\partial h \circ \psi}{\partial x_d}(x) = \partial_d^x h(\psi(x)), \quad d = 1, \dots, D \quad (27)$$

where $h \in C(\mathcal{U})$ and $x \in \varphi(\mathcal{U})$.

Definition 5. Let $V, W \in \mathcal{T}\overline{\mathcal{M}}$ be differentiable vector fields and f unit-variance random field over a manifold $\overline{\mathcal{M}}$ with almost surely differentiable sample paths. Then

$$\bar{\Lambda}_s(V, W) = \text{Cov}[Vf(s), Wf(s)], \quad s \in \overline{\mathcal{M}}, \quad (28)$$

is called the *induced Riemannian metric of f* on $\overline{\mathcal{M}}$. In local coordinates at a point $z \in \mathcal{W}$ it is represented by

$$\begin{aligned} \bar{\Lambda}_z(V, W) &= \sum_{d, d'=1}^D V_d W_{d'} \partial_d^x \partial_{d'}^y \text{Cov}[f(\psi(x)), f(\psi(y))] \Big|_{(x,y)=(z,z)} \\ &= \sum_{d, d'=1}^D V_d W_{d'} \text{Cov} \left[\partial_d^x f(\psi(x)) \Big|_{x=z}, \partial_{d'}^y f(\psi(y)) \Big|_{y=z} \right]. \end{aligned} \quad (29)$$

Here $V_1, \dots, V_D, W_1, \dots, W_D \in C(\mathcal{W})$ are the coordinate coefficients representing the vector fields V and W .

Remark 11. Assumption **(G2)** from the main manuscript ensures that this is a Riemannian metric on $\overline{\mathcal{M}}$.

Since the vector fields $\partial_d, d = 1, \dots, D$, form a basis of $\mathcal{T}\mathcal{U}$ the Riemannian metric induced by the random field f can be written in local coordinates as the $D \times D$ matrix having components

$$\bar{\Lambda}_{dd'}(z) = \text{Cov} \left[\partial_d^x f(\psi(x)) \Big|_{x=z}, \partial_{d'}^y f(\psi(y)) \Big|_{y=z} \right] \quad (30)$$

For simplicity in what follows, we establish the following alternative notations suppressing the dependencies on f :

$$\text{Cov}[\partial_d^x f(x), f(y)] = \langle \partial_d^x, 1_y \rangle, \quad \text{Cov}[\partial_d^x f(x), \partial_{d'}^y f(y)] = \langle \partial_d^x, \partial_{d'}^y \rangle. \quad (31)$$

Similarly, $\|1_x\|^2 = \text{Var}[f(x)]$ and $\|\partial_d^x\|^2 = \text{Var}[\partial_d^x f(x)]$.

Theorem 4. *The Riemannian metric on $\overline{\mathcal{M}}$ induced by a normalized random field is given in local coordinates by*

$$\bar{\Lambda}_{dd'}(x) = \frac{\langle \partial_d^x, \partial_{d'}^x \rangle}{\|1_x\|} - \frac{\langle \partial_d^x, 1_x \rangle \langle \partial_{d'}^x, 1_x \rangle}{\|1_x\|^2}. \quad (32)$$

The computation of Lipschitz-Killing curvatures requires the shape operator and the Riemannian curvature. Therefore, the next theorem computes the Christoffel symbols of the first kind, which can be used to express these quantities in local coordinates. This is because most fundamental geometric quantities such as the covariant derivative and the Riemannian curvature are functions of the Christoffel symbols and their derivatives.

Theorem 5. *The Christoffel symbols $\bar{\Gamma}_{kdd'}$, $k, d, d' \in \{1, \dots, D\}$ of the first kind of the induced Riemannian metric by a normalized field are given by*

$$\begin{aligned} \bar{\Gamma}_{kdd'}(x) = & \frac{\langle \partial_k^x \partial_d^x, \partial_{d'}^x \rangle}{\|1_x\|} - \frac{\langle \partial_k^x \partial_d^x, 1_x \rangle \langle \partial_{d'}^x, 1_x \rangle}{\|1_x\|^2} - \frac{\langle \partial_k^x, \partial_{d'}^x \rangle \langle \partial_d^x, 1_x \rangle}{\|1_x\|^2} \\ & - \frac{\langle \partial_k^x, 1_x \rangle \langle \partial_d^x, \partial_{d'}^x \rangle}{\|1_x\|^2} + 2 \frac{\langle \partial_k^x, 1_x \rangle \langle \partial_d^x, f_x \rangle \langle \partial_{d'}^x, 1_x \rangle}{\|1_x\|^3}. \end{aligned} \quad (33)$$

In terms of Christoffel symbols the covariant derivative $\bar{\nabla}$ on $\overline{\mathcal{M}}$ is expressed in the local chart φ by

$$\bar{\nabla}_{\partial_d} \partial_{d'} = \sum_{h=1}^D \sum_{h'=1}^D \bar{\Lambda}^{hh'} \bar{\Gamma}_{dd'h'} \partial_h = \bar{\Lambda}^{-1} (\bar{\Gamma}_{dd'1}, \dots, \bar{\Gamma}_{dd'D})^T.$$

Here $\bar{\Lambda}^{dd'}$ denotes the (d, d') -entry of the inverse of $\bar{\Lambda}$ in the coordinates (\mathcal{U}, φ) . This formula can be used to extend the covariant derivative to any vector field, i.e.,

$$\bar{\nabla}_V W = \sum_{d=1}^D \sum_{d'=1}^D V_d \bar{\nabla}_{\partial_d} W_{d'} \partial_{d'} = \sum_{d=1}^D \sum_{d'=1}^D V_d \left(\partial_d(W_{d'}) \partial_{d'} + W_{d'} \bar{\nabla}_{\partial_d} \partial_{d'} \right). \quad (34)$$

In particular, if all $\Gamma_{dd'd''} = 0$, $d, d', d'' \in \{1, \dots, D\}$, then

$$\bar{\nabla}_V W = \sum_{d=1}^D \sum_{d'=1}^D V_d \partial_d(W_{d'}) \partial_{d'}. \quad (35)$$

This happens, if $\bar{\Lambda}(s) = \bar{\Lambda}(s')$ for all $s, s' \in \overline{\mathcal{M}}$.

The last geometric quantity required to compute LKCs is the Riemannian curvature tensor \bar{R} . The curvature tensor has in local coordinates the entries

$$\bar{R}_{lkdd'}^\varphi = \partial_l \bar{\Gamma}_{kdd'} - \partial_k \bar{\Gamma}_{ldd'} + \sum_{m,n=1}^D (\bar{\Gamma}_{ldm} \bar{\Lambda}^{mn} \bar{\Gamma}_{kd'n} - \bar{\Gamma}_{kdm} \bar{\Lambda}^{mn} \bar{\Gamma}_{ld'n}) \quad (36)$$

for $i, j, k, l \in \{1, \dots, D\}$, compare [Adler and Taylor, 2009, eq. (7.7.4)]. By now, we derived almost all quantities to state the Riemannian curvature tensor in local coordinates. The missing quantities are the derivatives of the Christoffel symbols which can be found in the next Lemma.

Lemma 1. *The difference of the derivatives of Christoffel symbols in the Riemannian curvature tensor (36) of a normalized field can be expressed as:*

$$\begin{aligned}
& \partial_l \bar{\Gamma}_{kdd'}(x) - \partial_k \bar{\Gamma}_{ldd'}(x) \\
&= \frac{\langle \partial_k^x \partial_d^x, \partial_l^x \partial_{d'}^x \rangle - \langle \partial_l^x \partial_d^x, \partial_k^x \partial_{d'}^x \rangle}{\|1_x\|} \\
&\quad - \|1_x\|^{-2} \left(\langle \partial_l^x, 1_x \rangle \langle \partial_k^x \partial_d^x, \partial_{d'}^x \rangle - \langle \partial_k^x, 1_x \rangle \langle \partial_l^x \partial_d^x, \partial_{d'}^x \rangle \right. \\
&\quad \quad + \langle \partial_k^x \partial_d^x, \partial_l^x \rangle \langle \partial_{d'}^x, 1_x \rangle - \langle \partial_l^x \partial_d^x, \partial_k^x \rangle \langle \partial_{d'}^x, 1_x \rangle \\
&\quad \quad + \langle \partial_k^x \partial_d^x, 1_x \rangle \langle \partial_l^x \partial_{d'}^x, 1_x \rangle - \langle \partial_l^x \partial_d^x, 1_x \rangle \langle \partial_k^x \partial_{d'}^x, 1_x \rangle \\
&\quad \quad + \langle \partial_k^x, 1_x \rangle \langle \partial_l^x \partial_{d'}^x, \partial_d^x \rangle - \langle \partial_l^x, 1_x \rangle \langle \partial_k^x \partial_{d'}^x, \partial_d^x \rangle \\
&\quad \quad + \langle \partial_l^x, \partial_d^x \rangle \langle \partial_k^x, \partial_{d'}^x \rangle - \langle \partial_k^x, \partial_d^x \rangle \langle \partial_l^x, \partial_{d'}^x \rangle \\
&\quad \quad + \langle \partial_l^x, \partial_d^x \rangle \langle \partial_k^x, \partial_{d'}^x \rangle - \langle \partial_k^x, \partial_d^x \rangle \langle \partial_l^x, \partial_{d'}^x \rangle \\
&\quad \quad + \langle \partial_k^x, \partial_l^x \partial_{d'}^x \rangle \langle \partial_d^x, 1_x \rangle - \langle \partial_l^x, \partial_k^x \partial_{d'}^x \rangle \langle \partial_d^x, 1_x \rangle \Big) \\
&\quad + 2\|1_x\|^{-3} \left(\langle \partial_l^x, 1_x \rangle \langle \partial_k^x \partial_d^x, 1_x \rangle \langle \partial_{d'}^x, 1_x \rangle - \langle \partial_k^x, 1_x \rangle \langle \partial_l^x \partial_d^x, 1_x \rangle \langle \partial_{d'}^x, 1_x \rangle \right. \\
&\quad \quad + \langle \partial_k^x, 1_x \rangle \langle \partial_d^x, \partial_l^x \rangle \langle \partial_{d'}^x, 1_x \rangle - \langle \partial_l^x, 1_x \rangle \langle \partial_d^x, \partial_k^x \rangle \langle \partial_{d'}^x, 1_x \rangle \\
&\quad \quad + \langle \partial_k^x, 1_x \rangle \langle \partial_d^x, 1_x \rangle \langle \partial_l^x \partial_{d'}^x, 1_x \rangle - \langle \partial_l^x, 1_x \rangle \langle \partial_d^x, 1_x \rangle \langle \partial_k^x \partial_{d'}^x, 1_x \rangle \\
&\quad \quad \left. + \langle \partial_l^x, 1_x \rangle \langle \partial_d^x, 1_x \rangle \langle \partial_k^x, \partial_{d'}^x \rangle - \langle \partial_k^x, 1_x \rangle \langle \partial_d^x, 1_x \rangle \langle \partial_l^x, \partial_{d'}^x \rangle \right)
\end{aligned}$$

Proof. Simple, but lengthy computation. □

To compute the first LKC \mathcal{L}_1 for a 3-dimensional manifold the trace of the Riemannian tensor is needed which in the coordinates (\mathcal{U}, φ) can be expressed in terms of the entries of the inverse of the square root of the Riemannian metric and the Riemannian tensor as

$$\begin{aligned}
\text{tr}(\bar{R}) = \sum_{i,j,k,l=1}^3 \bar{R}_{ijkl}^\varphi \left(\frac{\bar{\Lambda}_{1i}^{-1/2} \bar{\Lambda}_{1j}^{-1/2} \bar{\Lambda}_{1k}^{-1/2} \bar{\Lambda}_{1l}^{-1/2}}{2} \right. \\
+ \frac{\bar{\Lambda}_{2i}^{-1/2} \bar{\Lambda}_{2j}^{-1/2} \bar{\Lambda}_{2k}^{-1/2} \bar{\Lambda}_{2l}^{-1/2}}{2} \\
+ \frac{\bar{\Lambda}_{3i}^{-1/2} \bar{\Lambda}_{3j}^{-1/2} \bar{\Lambda}_{3k}^{-1/2} \bar{\Lambda}_{3l}^{-1/2}}{2} \\
+ \bar{\Lambda}_{1i}^{-1/2} \bar{\Lambda}_{2j}^{-1/2} \bar{\Lambda}_{1k}^{-1/2} \bar{\Lambda}_{2l}^{-1/2} \\
+ \bar{\Lambda}_{1i}^{-1/2} \bar{\Lambda}_{3j}^{-1/2} \bar{\Lambda}_{1k}^{-1/2} \bar{\Lambda}_{3l}^{-1/2} \\
\left. + \bar{\Lambda}_{2i}^{-1/2} \bar{\Lambda}_{3j}^{-1/2} \bar{\Lambda}_{2k}^{-1/2} \bar{\Lambda}_{3l}^{-1/2} \right). \tag{37}
\end{aligned}$$

B.2 Definition of LKCs

Lipschitz Killing Curvatures $\mathcal{L}_1, \dots, \mathcal{L}_D$ are the intrinsic volumes of a compact D -dimensional Whitney stratified (WS) manifold $(\mathcal{M}, \underline{\Lambda})$ isometrically embedded into $(\bar{\mathcal{M}}, \bar{\Lambda})$. Here Λ and $\bar{\Lambda}$ denote Riemannian metrics of \mathcal{M} and $\bar{\mathcal{M}}$. They are related by $\bar{\Lambda} \circ \iota = \Lambda$ where $\iota : \mathcal{M} \rightarrow \bar{\mathcal{M}}$ is the embedding and hence \mathcal{M} is isometrically embedded into $\bar{\mathcal{M}}$. In this section we make the

formula for the LKCs [Adler and Taylor, 2009, Definition 10.7.2] of an at most 3-dimensional WS manifold more explicit. From the definition of the LKCs it is easy to deduce

$$\mathcal{L}_{D-1} = \text{vol}_{D-1}(\partial_{D-1}\mathcal{M}) \quad \text{and} \quad \mathcal{L}_D = \text{vol}_D(\partial_D\mathcal{M}). \quad (38)$$

Here $\partial_d\mathcal{M}$ denotes the d -dimensional stratum of \mathcal{M} and the volume is the volume of the Riemannian manifold $(\partial_d\mathcal{M}, \Lambda|_{\partial_d\mathcal{M}})$ where $\Lambda|_{\partial_d\mathcal{M}}$ is the restriction of Λ to $\partial_d\mathcal{M}$.

For a 3-dimensional manifold it remains to compute \mathcal{L}_1 , which we derive from [Adler and Taylor, 2009, Definition 10.7.2] and some geometric computations in the next proposition.

Proposition 8. *Let $(\overline{\mathcal{M}}, \overline{\Lambda})$ be a closed Riemannian manifold of dimension 3 and $\mathcal{M} \subset \overline{\mathcal{M}}$ be a compact WS manifold of dimension 3 isometrically embedded into $\overline{\mathcal{M}}$. Then*

$$\begin{aligned} \mathcal{L}_1 &= \frac{1}{2\pi} \int_{\partial_1\mathcal{M}} \int_{\mathbb{S}(\mathcal{T}_s\partial_1\mathcal{M}^\perp)} \alpha(v) \mathcal{H}_1(dv) \mathcal{H}_1(ds) \\ &\quad + \frac{1}{2\pi} \int_{\partial_2\mathcal{M}} \overline{\Lambda} \left(\overline{\nabla}_{U_s} U_s + \overline{\nabla}_{V_s} V_s, N_s \right) \mathcal{H}_2(ds) \\ &\quad - \frac{1}{2\pi} \int_{\partial_3\mathcal{M}} \text{Tr}^{\mathcal{T}_s\partial_3\mathcal{M}}(\overline{R}) \mathcal{H}_3(ds) \end{aligned} \quad (39)$$

Here $\mathcal{H}_1(dv)$ is the volume form induced on the sphere

$$\mathbb{S}(\mathcal{T}_s\partial_1\mathcal{M}^\perp) = \{v \in \mathcal{T}_s\overline{\mathcal{M}} \mid \overline{\Lambda}(v, v) = 1 \wedge \overline{\Lambda}(v, w) = 0 \text{ for } w \in \mathcal{T}_s\partial_1\mathcal{M}\}$$

by $\overline{\Lambda}$ and $\mathcal{H}_d(ds)$ the volume form of $\partial_d\mathcal{M}$. Moreover, $\alpha(v)$ denotes the normal Morse index given in [Adler and Taylor, 2009, Scn 9.2.1] and U, V, N is a piecewise differentiable vector field on $\partial_2\mathcal{M}$ such that U_s, V_s form an orthonormal basis for $\mathcal{T}_s\partial_2\mathcal{M}$ for all $s \in \partial_2\mathcal{M}$ and N is outward pointing normal vector field.

Remark 12. In the special case that the metric $\overline{\Lambda}$ is constant, it holds that

$$\begin{aligned} \mathcal{L}_1 &= \frac{1}{2\pi} \int_{\partial_1\mathcal{M}} \int_{\mathbb{S}(\mathcal{T}_s\partial_1\mathcal{M}^\perp)} \alpha(v) \mathcal{H}_1(dv) \mathcal{H}_1(ds) \\ &\quad + \frac{1}{2\pi} \int_{\partial_2\mathcal{M}} \overline{\Lambda} \left(\overline{\nabla}_{U_s} U_s + \overline{\nabla}_{V_s} V_s, N_s \right) \mathcal{H}_2(ds), \end{aligned}$$

since the curvature tensor \overline{R} vanishes. If $\mathcal{M} = \mathcal{M}_\mathcal{V}$ is a voxel manifold than even

$$\mathcal{L}_1 = \frac{1}{2\pi} \int_{\partial_1\mathcal{M}} \int_{\mathbb{S}(\mathcal{T}_s\partial_1\mathcal{M}^\perp)} \alpha(v) \mathcal{H}_1(dv) \mathcal{H}_1(ds),$$

as $\nabla_{U_s} U_s = \nabla_{V_s} V_s = 0$ on $\partial_2\mathcal{M}$ by (35) and $\overline{\Lambda}$ being constant.

Using the above Theorem we can now derive an expression for \mathcal{L}_1 of a 3-dimensional voxel manifold.

Theorem 6. Let \mathcal{M}_γ be a 3-dimensional voxel manifold. Then

$$\begin{aligned}
\mathcal{L}_1 &= \frac{1}{2\pi} \sum_{|I|=1} \int_{\mathcal{F}_I} \Theta(x) \sqrt{\det(\Lambda^I(x))} dx^I \\
&+ \frac{1}{2\pi} \sum_{|I|=2} \int_{\mathcal{F}_I} \left[(U_{I_1}(x)^2 + V_{I_1}(x)^2) N^T(x) \begin{pmatrix} \Gamma_{I_1 I_1 1}(x) \\ \Gamma_{I_1 I_1 2}(x) \\ \Gamma_{I_1 I_1 3}(x) \end{pmatrix} \right. \\
&\quad \left. + \sum_{k=1}^2 V_{I_k}(x) V_{I_2}(x) N^T(x) \begin{pmatrix} \Gamma_{I_k I_2 1}(x) \\ \Gamma_{I_k I_2 2}(x) \\ \Gamma_{I_k I_2 3}(x) \end{pmatrix} \right] \sqrt{\det(\Lambda^I(x))} dx^I \\
&- \frac{1}{2\pi} \sum_{v \in \mathcal{V}} \int_{\mathcal{B}_v(\delta)} \text{Tr}(R(x)) \sqrt{\det(\Lambda(x))} dx
\end{aligned} \tag{40}$$

Here $\text{Tr}(R(x))$ is the trace of the Riemannian curvature tensor and

$$\Theta(x) = \begin{cases} \pi - \beta(x), & \text{if } x \text{ belongs to a convex edge} \\ -2\beta(x), & \text{if } x \text{ belongs to a double convex edge,} \\ \beta(x) - \pi, & \text{if } x \text{ belongs to a concave edge} \end{cases}$$

compare Appendix B.1 and especially (37). Here $\beta(x)$ is defined using the crossproduct $V_x \times N_x = (m_1^I(x), m_2^I(x), m_3^I(x))$ of the elements of the ONB from (14) with $k = I$ by

$$\beta(x) = \arccos \left(\frac{m_2(x)m_3(x)}{\sqrt{m_2^2(x) + m_1^2(x)} \sqrt{m_3^2(x) + m_1^2(x)}} \right).$$

The different types of edges are visualized in Figure 22.

C Proofs of Results in the Appendix

C.1 Proof of Theorem 4

Proof. Interchanging expectation and derivatives yields

$$\begin{aligned}
\bar{\Lambda}_{dd'}(z) &= \partial_d^x \partial_{d'}^y \frac{\text{Cov}[f_x, f_y]}{\|1_x\| \|1_y\|} \Big|_{(x,y)=(z,z)} \\
&= \frac{\langle \partial_d^x, \partial_{d'}^y \rangle}{\|1_x\| \|1_y\|} - \frac{\langle \partial_d^x, 1_y \rangle \langle 1_y, \partial_{d'}^y \rangle}{\|1_x\| \|1_y\|^3} \\
&\quad - \frac{\langle \partial_d^x, 1_x \rangle \langle 1_x, \partial_{d'}^y \rangle}{\|1_x\|^3 \|1_y\|} + \frac{\langle 1_x, 1_y \rangle \langle \partial_d^x, 1_x \rangle \langle 1_y, \partial_{d'}^y \rangle}{\|1_x\|^3 \|1_y\|^3} \Big|_{(x,y)=(z,z)} \\
&= \frac{\langle \partial_d^z, \partial_{d'}^z \rangle}{\|1_z\|^2} - \frac{\langle \partial_d^z, 1_z \rangle \langle 1_z, \partial_{d'}^z \rangle}{\|1_z\|^4}
\end{aligned} \tag{41}$$

□

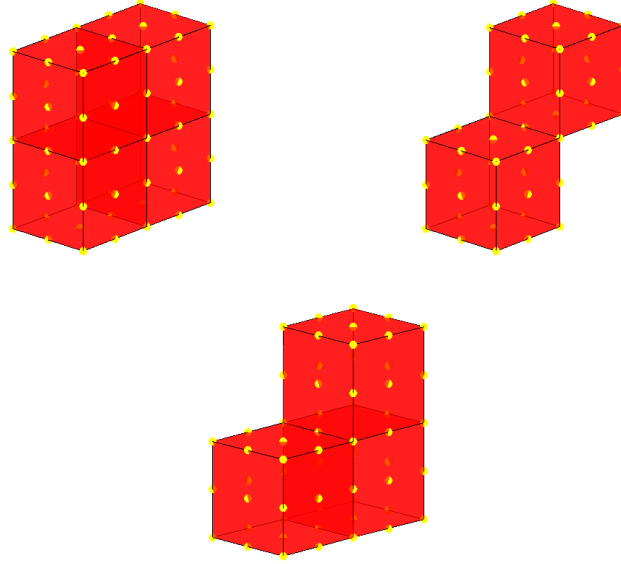


Figure 22: Visualization of the different types of edges appearing in a voxel manifold. In the left voxel manifold all edges are convex. The edge where the two cubes of the voxel manifold in the center are touching is a double convex edge and the same edge in the voxel manifold on the right is a concave edge since a third cube is added.

C.2 Proof of Theorem 5

Proof. From the definition of the Christoffel symbols one can derive that

$$\Gamma_{kdd'}(z) = \frac{\partial^3 \tilde{c}(x, y)}{\partial x_k \partial x_d \partial y_{d'}} \Big|_{(x, y) = (z, z)}, \quad (42)$$

see also [Adler and Taylor, 2009, eq. 12.2.17]. Here $\tilde{c}(x, y) = \frac{\text{Cov}[f_x, f_y]}{\sqrt{\text{Cov}[f_x, f_x]}\sqrt{\text{Cov}[f_y, f_y]}}$. Thus, by simply taking another derivate of (41), we obtain

$$\begin{aligned}
\Gamma_{kdd'}(z) &= \partial_k^x \partial_d^x \partial_{d'}^y \frac{\text{Cov}[f_x, f_y]}{\sqrt{\|1_x\| \|1_y\|}} \Big|_{(x,y)=(z,z)} \\
&= \frac{\langle \partial_k^x \partial_d^x, \partial_{d'}^x \rangle}{\|1_x\|^2} - \frac{\langle \partial_k^x, 1_x \rangle \langle \partial_d^x, \partial_{d'}^x \rangle}{\|1_x\|^4} - \partial_k^x \frac{\langle \partial_d^x, 1_y \rangle \langle 1_y, \partial_{d'}^y \rangle}{\|1_x\| \|1_y\|^3} \\
&\quad - \partial_k^x \frac{\langle \partial_d^x, 1_x \rangle \langle 1_x, \partial_{d'}^y \rangle}{\|1_x\|^3 \|1_y\|} + \partial_k^x \frac{\langle 1_x, 1_y \rangle \langle \partial_d^x, 1_x \rangle \langle 1_y, \partial_{d'}^y \rangle}{\|1_x\|^3 \|1_y\|^3} \Big|_{(x,y)=(z,z)} \\
&= \frac{\langle \partial_k^z \partial_d^z, \partial_{d'}^z \rangle}{\|1_z\|^2} - \frac{\langle \partial_k^z, 1_z \rangle \langle \partial_d^z, \partial_{d'}^z \rangle}{\|1_z\|^4} - \frac{\langle \partial_k^z \partial_d^z, 1_z \rangle \langle 1_z, \partial_{d'}^z \rangle}{\|1_z\|^4} \\
&\quad + \frac{\langle \partial_k^z, 1_z \rangle \langle \partial_d^z, 1_z \rangle \langle 1_z, \partial_{d'}^z \rangle}{\|1_z\|^6} - \frac{\langle \partial_k^z \partial_d^z, 1_z \rangle \langle 1_z, \partial_{d'}^z \rangle + \langle \partial_d^z, \partial_k^z \rangle \langle 1_z, \partial_{d'}^z \rangle}{\|1_z\|^4} \\
&\quad - \frac{\langle \partial_d^z, 1_z \rangle \langle \partial_k^z, \partial_{d'}^z \rangle}{\|1_z\|^4} + 3 \frac{\langle \partial_k^z, 1_z \rangle \langle \partial_d^z, 1_z \rangle \langle 1_z, \partial_{d'}^z \rangle}{\|1_z\|^6} \\
&\quad + \frac{\langle \partial_k^z, 1_z \rangle \langle \partial_d^z, 1_z \rangle \langle 1_z, \partial_{d'}^z \rangle}{\|1_z\|^6} + \frac{\langle \partial_k^z \partial_d^z, 1_z \rangle \langle 1_z, \partial_{d'}^z \rangle}{\|1_z\|^4} + \frac{\langle \partial_d^z, \partial_k^z \rangle \langle 1_z, \partial_{d'}^z \rangle}{\|1_z\|^4} \\
&\quad - 3 \frac{\langle \partial_k^z, 1_z \rangle \langle \partial_d^z, 1_z \rangle \langle 1_z, \partial_{d'}^z \rangle}{\|1_z\|^6} \\
&= \frac{\langle \partial_k^z \partial_d^z, \partial_{d'}^z \rangle}{\|1_z\|^2} - \frac{\langle \partial_k^z, 1_z \rangle \langle \partial_d^z, \partial_{d'}^z \rangle}{\|1_z\|^4} - \frac{\langle \partial_k^z \partial_d^z, 1_z \rangle \langle 1_z, \partial_{d'}^z \rangle}{\|1_z\|^4} \\
&\quad - \frac{\langle \partial_d^z, 1_z \rangle \langle \partial_k^z, \partial_{d'}^z \rangle}{\|1_z\|^4} + 2 \frac{\langle \partial_k^z, 1_z \rangle \langle \partial_d^z, 1_z \rangle \langle 1_z, \partial_{d'}^z \rangle}{\|1_z\|^6}
\end{aligned}$$

□

C.3 Proof of Proposition 8

Proof. Using $D - d' = D'$ we have that the LKCs of a WS manifold \mathcal{M} are defined by

$$\begin{aligned}
\mathcal{L}_d &= \sum_{d'=d}^D \frac{1}{(2\pi)^{\frac{d'-d}{2}}} \sum_{l=0}^{\lfloor \frac{d'-d}{2} \rfloor} \frac{(-1)^l C(D', d-d'-2l)}{l!(d-d'-2l)!} \\
&\quad \times \int_{\partial_{d'} \mathcal{M}} \int_{\mathbb{S}(\mathcal{T}_s \partial_{d'} \mathcal{M}^\perp)} \text{Tr} \mathcal{T}_s \partial_{d'} \mathcal{M} \left(R^l S_{\nu_{D'}}^{d'-d-2l} \right) \alpha(\nu_{D'}) \mathcal{H}_{-1}(d\nu_{D'}) \mathcal{H}_{d'}(ds),
\end{aligned} \tag{43}$$

compare [Adler and Taylor, 2009, Definition 10.7.2]. This formula requires further explanations. The constant $C(m, i)$ is defined in [Adler and Taylor, 2009, eq. (10.5.1), p.233], i.e.,

$$C(m, i) = \begin{cases} \frac{(2\pi)^{\frac{i}{2}}}{s_{m+i}}, & m+i > 0, \\ 1, & m=0 \end{cases} \quad \text{with} \quad s_m = \frac{2\pi^{m/2}}{\Gamma(m/2)}, \tag{44}$$

which implies $C(m, 0) = \Gamma(m/2)/2/\pi^{m/2}$. Moreover, \mathcal{H}_{D-d-1} is the volume form on $\mathbb{S}(\mathcal{T}_s \partial_d \mathcal{M}^\perp)$ and \mathcal{H}_d the volume form of $\partial_d \mathcal{M}$. R denotes the Riemannian curvature tensor of the different

strata on \mathcal{M} depending on the strata the integral integrates over. In particular, note that $\bar{R} = R$ for $\partial_3\mathcal{M}$.

From this \mathcal{L}_1 simplifies to

$$\begin{aligned}
\mathcal{L}_1 &= C(3, 0) \int_{\partial_1\mathcal{M}} \int_{S(\mathcal{T}_s\partial_1\mathcal{M}^\perp)} \mathrm{Tr}^{\mathcal{T}_s\partial_1\mathcal{M}} \left(R^0 S_{\nu_2}^0 \right) \alpha(\nu_2) \mathcal{H}_1(d\nu_2) \mathcal{H}_1(ds) \\
&\quad + \frac{C(1, 1)}{\sqrt{2\pi}} \int_{\partial_2\mathcal{M}} \int_{S(\mathcal{T}_s\partial_2\mathcal{M}^\perp)} \mathrm{Tr}^{\mathcal{T}_s\partial_2\mathcal{M}} \left(R^0 S_{\nu_1}^1 \right) \alpha(\nu_1) \mathcal{H}_0(d\nu_1) \mathcal{H}_2(ds) \\
&\quad + \frac{C(0, 2)}{4\pi} \int_{\partial_3\mathcal{M}} \int_{S(\mathbb{O})} \mathrm{Tr}^{\mathcal{T}_s\partial_3\mathcal{M}} \left(R^0 S_{\nu_0}^2 \right) \alpha(\nu_0) \mathcal{H}_{-1}(d\nu_0) \mathcal{H}_3(ds) \\
&\quad - \frac{C(0, 0)}{2\pi} \int_{\partial_3\mathcal{M}} \int_{S(\mathbb{O})} \mathrm{Tr}^{\mathcal{T}_s\partial_3\mathcal{M}} \left(R^1 S_{\nu_0}^0 \right) \alpha(\nu_0) \mathcal{H}_{-1}(d\nu_0) \mathcal{H}_3(ds) \\
&= \frac{1}{2\pi} \int_{\partial_1\mathcal{M}} \int_{S(\mathcal{T}_s\partial_1\mathcal{M}^\perp)} \alpha(\nu_2) \mathcal{H}_1(d\nu_2) \mathcal{H}_1(ds) \\
&\quad + \frac{1}{2\pi} \int_{\partial_2\mathcal{M}} \int_{S(\mathcal{T}_s\partial_2\mathcal{M}^\perp)} \mathrm{Tr}^{\mathcal{T}_s\partial_2\mathcal{M}} \left(1 \cdot S_{\nu_1}^1 \right) \alpha(\nu_1) \mathcal{H}_0(d\nu_1) \mathcal{H}_2(ds) \\
&\quad + \frac{1}{4\pi} \int_{\partial_3\mathcal{M}} \mathrm{Tr}^{\mathcal{T}_s\partial_3\mathcal{M}} \left(1 \cdot S_{\mathbb{O}}^2 \right) \mathcal{H}_3(ds) \\
&\quad - \frac{1}{2\pi} \int_{\partial_3\mathcal{M}} \mathrm{Tr}^{\mathcal{T}_s\partial_3\mathcal{M}} \left(R^1 S_{\mathbb{O}}^0 \right) \mathcal{H}_3(ds)
\end{aligned}$$

This can be further simplified as follows:

$$\begin{aligned}
\mathcal{L}_1 &= \frac{1}{2\pi} \int_{\partial_1\mathcal{M}} \int_{S(\mathcal{T}_s\partial_1\mathcal{M}^\perp)} \alpha(\nu_2) \mathcal{H}_1(d\nu_2) \mathcal{H}_1(ds) \\
&\quad + \frac{1}{2\pi} \int_{\partial_2\mathcal{M}} \int_{S(\mathcal{T}_s\partial_2\mathcal{M}^\perp)} \mathrm{Tr}^{\mathcal{T}_s\partial_2\mathcal{M}} \left(S_{\nu_1}^1 \right) \alpha(\nu_1) \mathcal{H}_0(d\nu_1) \mathcal{H}_2(ds) \\
&\quad - \frac{1}{2\pi} \int_{\partial_3\mathcal{M}} \mathrm{Tr}^{\mathcal{T}_s\partial_3\mathcal{M}} (\bar{R}) \mathcal{H}_3(ds) \\
&= \frac{1}{2\pi} \int_{\partial_1\mathcal{M}} \int_{S(\mathcal{T}_s\partial_1\mathcal{M}^\perp)} \alpha(\nu_2) \mathcal{H}_1(d\nu_2) \mathcal{H}_1(ds) \\
&\quad + \frac{1}{2\pi} \int_{\partial_2\mathcal{M}} g(\bar{\nabla}_{e_1(s)} e_1(s), \tilde{\nu}(s)) + g(\bar{\nabla}_{e_2(s)} e_2(s), \tilde{\nu}(s)) \mathcal{H}_2(ds) \\
&\quad - \frac{1}{2\pi} \int_{\partial_3\mathcal{M}} \mathrm{Tr}^{\mathcal{T}_s\partial_3\mathcal{M}} (\bar{R}) \mathcal{H}_3(ds) \\
&= \frac{1}{2\pi} \int_{\partial_1\mathcal{M}} \int_{S(\mathcal{T}_s\partial_1\mathcal{M}^\perp)} \alpha(\nu_2) \mathcal{H}_1(d\nu_2) \mathcal{H}_1(ds) \\
&\quad + \frac{1}{2\pi} \int_{\partial_2\mathcal{M}} g(\bar{\nabla}_{e_1(s)} e_1(s) + \bar{\nabla}_{e_2(s)} e_2(s), \tilde{\nu}(s)) \mathcal{H}_2(ds) \\
&\quad - \frac{1}{2\pi} \int_{\partial_3\mathcal{M}} \mathrm{Tr}^{\mathcal{T}_s\partial_3\mathcal{M}} (\bar{R}) \mathcal{H}_3(ds)
\end{aligned}$$

Here $\tilde{\nu}(s)$ is the inward pointing normal at x in $\partial_2\mathcal{M}$ and $e_1(s), e_2(s)$ an orthonormal basis of $\mathcal{T}_s\partial_2\mathcal{M}$ and used Remark (10.5.2) [Adler and Taylor, 2009, p.233], i.e.,

$$S_{\mathbb{O}}^j = \begin{cases} 1, & j = 0, \\ 0, & \text{otherwise} \end{cases}. \quad (45)$$

□

D Proofs of the Results in the Main Manuscript

D.1 Proof of Proposition 2

Proof. Define $q = p/(p - 1)$ if $p > 1$ and $q = \infty$ if $p = 1$. Using the triangle inequality and Hölder's inequality yields for the charts $(\bar{U}_\alpha, \bar{\varphi}_\alpha)$, $\alpha \in \{1, \dots, P\}$, in the atlas of $\bar{\mathcal{M}}$ covering \mathcal{M} , all $x, y \in \bar{\varphi}(\bar{U}_\alpha) \cap \mathcal{M}$ that

$$\begin{aligned} |\tilde{X}_\alpha(x) - \tilde{X}_\alpha(y)| &= \left| \sum_{v \in \mathcal{V}} \left(K(\bar{\varphi}_\alpha^{-1}(x), v) - K(\bar{\varphi}_\alpha^{-1}(y), v) \right) X(v) \right| \\ &\leq \sqrt[q]{\sum_{v \in \mathcal{V}} \left| K(\bar{\varphi}_\alpha^{-1}(x), v) - K(\bar{\varphi}_\alpha^{-1}(y), v) \right|^q} \sqrt[p]{\sum_{v \in \mathcal{V}} X(v)^p} \\ &\leq \sqrt[q]{\sum_{v \in \mathcal{V}} A^q} \sqrt[p]{\sum_{v \in \mathcal{V}} X(v)^p} \|x - y\|^\gamma \\ &\leq L \|x - y\|^\gamma. \end{aligned}$$

Here A bounds the Hölder constants of $K(\bar{\varphi}_\alpha^{-1}(\cdot), v)$, for all $\alpha \in \{1, \dots, P\}$ and all $v \in \mathcal{V}$ from above, and $L = |\mathcal{V}| A \sqrt[q]{\sum_{v \in \mathcal{V}} X(v)^p}$. If $p = 1$ then the statement with the q -th root is the maximum over \mathcal{V} instead of the q -norm. The result follows as by assumption $\mathbb{E}[L^p]$ is finite. □

D.2 Proof of Proposition 3

Proof. The functions $K(\bar{\varphi}_\alpha^{-1}(\cdot), v)$ are Lipschitz continuous for each $v \in \mathcal{V}$ since they are \mathcal{C}^1 and $\bar{\mathcal{M}}$ is compact. Because \mathcal{V} is finite and $\alpha \in \{1, \dots, P\}$, there exists an $M > 0$ that bounds all the Lipschitz constants of the functions $K(\bar{\varphi}_\alpha^{-1}(\cdot), v)$. Thus, applying Proposition 2 with $p = 2$ and $\gamma = 1$ yields for the charts $(\bar{U}_\alpha, \bar{\varphi}_\alpha)$, $\alpha \in \{1, \dots, P\}$, in the atlas of $\bar{\mathcal{M}}$ covering \mathcal{M} , all $x, y \in \bar{\varphi}(\bar{U}_\alpha) \cap \mathcal{M}$ such that $0 < \|x - y\| < 1$ that

$$\mathbb{E} \left[\left(\tilde{X}_\alpha(x) - \tilde{X}_\alpha(y) \right)^2 \right] \leq \mathbb{E} [L^2 \|x - y\|^2] = \mathbb{E} [L^2] \|x - y\|^2.$$

The claim follows since $x^2 \leq (\log |x|)^{-2}$ for $0 < x < 1$. □

D.3 Proof of Proposition 4

Proof. As the property is local, we can w.l.o.g. assume that \mathcal{M} is a compact domain in \mathbb{R}^D and drop the chart notation for simplicity. Given $x \in \mathcal{M}$, suppose that there exist sets of real constants a, a_i, a_{jk}, c ($1 \leq i \leq D, 1 \leq j \leq k \leq D$) such that

$$a\tilde{X}(s) + \sum_{i=1}^D a_i \tilde{X}_i(s) + \sum_{1 \leq j \leq k \leq D} a_{jk} \tilde{X}_{jk}(s) = c,$$

which implies that

$$\begin{aligned} a \sum_{v \in \mathcal{V}_s} K(s, v) X(v) + \sum_{i=1}^D a_i \sum_{v \in \mathcal{V}_s} \partial_i^s K(s, v) X(v) \\ + \sum_{1 \leq j \leq k \leq D} a_{jk} \sum_{v \in \mathcal{V}_s} \partial_{jk}^s K(s, v) X(v) = c. \end{aligned}$$

Non-degeneracy of $(X(v) : v \in \mathcal{V}_s)$ then implies that for all $v \in \mathcal{V}_s$

$$aK(s, v) + \sum_{i=1}^D a_i \partial_i^s K(s, v) + \sum_{1 \leq j \leq k \leq D} a_{jk} \partial_{jk}^s K(s, v) = 0,$$

which by the linear independence constraint implies that the constants are all zero. This proves non-degeneracy of $(Y(s), \nabla Y(s), (\nabla^2 Y(s)))$.

For the normalized field $\tilde{X}/\sqrt{\text{Var}[\tilde{X}]} = \tilde{X}/\sigma$, we note that

$$\nabla \frac{X}{\sigma} = \frac{\nabla X}{\sigma} - \frac{X \nabla \sigma}{\sigma^2} = \frac{\nabla X}{\sigma} - \frac{\nabla \sigma}{\sigma} \left(\frac{X}{\sigma} \right)$$

and

$$\nabla^2 \frac{X}{\sigma} = \frac{\nabla^2 X}{\sigma} - \frac{2(\nabla X)^T (\nabla \sigma)}{\sigma^2} - \frac{X \nabla^2 \sigma}{\sigma^2} + \frac{2(\nabla \sigma)^T (\nabla \sigma) X}{\sigma^3}.$$

Hence we can transform $(X(s), \nabla X(s), \mathbb{V}(\nabla^2 X(s)))$ into $(Z(s), \nabla Z(s), \mathbb{V}(\nabla^2 Z(s)))$ using an invertible matrix. Thus, $(Z(s), \nabla Z(s), \mathbb{V}(\nabla^2 Z(s)))$ is non-degenerate by Lemma A.2 from [Davenport and Telschow \[2022\]](#). \square

D.4 Proof of Proposition 6

D.4.1 Establishing non-degeneracy of the isotropic kernel and its derivatives under linear transformations

Lemma 2. *Suppose that \mathcal{V} satisfies the conditions of Proposition 6 and let $K^* = e^{-\|s-v\|^T/2}$ be the D -dimensional isotropic Gaussian kernel. Then given constants c, a_i, a_{jk} (for $1 \leq i \leq D$ and $1 \leq j \leq k \leq D$), $s \in \mathbb{R}^D$ and an invertible symmetric matrix $\Omega' \in \mathbb{R}^{D \times D}$ such that*

$$\begin{aligned} cK^*(\Omega' s, \Omega' v) + \sum_{j=1}^D a_j \partial_j^x K^*(\Omega' s, \Omega' v) \\ + \sum_{1 \leq j \leq k \leq D} a_{jk} \partial_{jk}^x K^*(\Omega' s, \Omega' v) = 0, \end{aligned} \tag{46}$$

for all $v \in \mathcal{V}$ then $c = a_i = a_{jk} = 0$ for $1 \leq i \leq D$ and $1 \leq j \leq k \leq D$.

Proof. For all $v \in \mathcal{V}$, letting $s^* = \Omega' s$ and dividing (46) by $e^{-\|s-v\|^2/2}$, it follows that

$$\begin{aligned} c + \sum_{j=1}^D a_j \left(s_j^* - \sum_{l=1}^D \Omega'_{jl} v_l \right) \\ + \sum_{1 \leq j \leq k \leq D} a_{jk} \left(\left(s_j^* - \sum_{l=1}^D \Omega'_{jl} v_l \right) \left(s_k^* - \sum_{l=1}^D \Omega'_{kl} v_l \right) - \delta_{jk} \right) = 0. \end{aligned}$$

In particular,

$$\begin{aligned}
& c + \sum_{j=1}^D a_j \left(s_j^* - \sum_{l=1}^D \Omega'_{jl} v_l \right) \\
& + \sum_{1 \leq j, k \leq D} a'_{jk} \left(\left(s_j^* - \sum_{l=1}^D \Omega'_{jl} v_l \right) \left(s_k^* - \sum_{l=1}^D \Omega'_{kl} v_l \right) - \delta_{jk} \right) = 0.
\end{aligned} \tag{47}$$

where $a'_{jk} = a_{jk}/2$, $j \neq k$ and $a'_{jj} = a_{jj}$.

For $i \in \{1, \dots, D\}$, fixing $(v_1, \dots, v_{i-1}, v_{i+1}, \dots, v_D)$, we can view (47) as a quadratic in v_i . As such the only way that it can have more than two distinct solutions is if where the coefficient of v_i^2 is zero, i.e.,

$$\sum_{1 \leq j, k \leq D} a'_{jk} \Omega'_{ji} \Omega'_{ki} = (\Omega' A' \Omega')_{ii} = 0. \tag{48}$$

Similarly the coefficient of v_i must be zero, i.e.,

$$\sum_{j=1}^D a_j \Omega'_{ji} + \sum_{j,k} \Omega'_{ji} \left(s_k^* - \sum_{m \neq i} \Omega'_{km} v_m \right) + \sum_{j,k} \left(s_k^* - \sum_{l \neq i} \Omega'_{jl} v_l \right) \Omega'_{ki} = 0. \tag{49}$$

Now allowing v_n to vary for some $n \neq i$, by the same logic, the coefficient of v_n in (49) is equal to zero, i.e.,

$$\sum_{j,k} a'_{jk} \Omega'_{ji} \Omega'_{kn} + \sum_{j,k} a'_{jk} \Omega'_{jn} \Omega'_{ki} = (\Omega' A' \Omega')_{in} + (\Omega' A' \Omega')_{ni} = 2(\Omega' A' \Omega')_{in} = 0.$$

As such $(\Omega' A' \Omega')_{in} = (\Omega' A' \Omega')_{ni} = 0$ for all $i \neq n$. Combining this with (48), it follows that $\Omega' A' \Omega' = 0$. In particular $A' = 0$ as Ω' is invertible. Thus, the remaining linear equation in v_i from (47) can only have more than one solution if

$$\sum_j a_j \Omega'_{ji} = 0.$$

Therefore $(\Omega' a)_i = 0$, where $a = (a_1, \dots, a_D)^T$. Since this holds for all i and Ω' is invertible, we obtain $a = 0$. Finally this implies that $c = 0$. \square

D.4.2 Establishing Proposition 6

Proof. We can write $K(s, v) = K^*(\Sigma^{-1/2}s, \Sigma^{-1/2}v)$ where $K^* = e^{-\|s-v\|^2/2}$ is the isotropic Gaussian kernel. Arguing as in proof of Lemma 1 of [Davenport and Telschow \[2022\]](#) (taking $\phi(s) = \Sigma^{-1/2}s$ and φ to be the identity in their notation), for each $s \in S$ we have

$$\mathbb{V}(\nabla^2 K(s, v)) = L(\Sigma^{1/2} \otimes \Sigma^{1/2}) R \mathbb{V}(\nabla^2 K^*(\Sigma^{-1/2}s, \Sigma^{-1/2}v))$$

where ∇^2 as usual always denotes the Hessian with respect to the first argument and $L \in \mathbb{R}^{D(D+1)/2 \times D^2}$ is the elimination matrix and $R \in \mathbb{R}^{D^2 \times D(D+1)/2}$ is the duplication matrix, the precise definitions of which can be found in [Magnus and Neudecker \[1980\]](#). The matrix $L(\Sigma^{1/2} \otimes \Sigma^{1/2})R$ is invertible by Lemma 4.4.iv of [Magnus and Neudecker \[1980\]](#), and the fact that $\Sigma^{1/2}$ is invertible.

Moreover $\nabla K(\Sigma^{-1/2}s, v) = \Sigma^{-1/2}\nabla K^*(\Sigma^{-1/2}s, \Sigma^{-1/2}v)$. As such there is an invertible linear transformation between the vector

$$\left(K(s, v), \nabla K(s, v), \mathbb{V}(\nabla^2 K(s, v))\right)$$

and the vector

$$\left(K^*(\Sigma^{-1/2}s, \Sigma^{-1/2}v), \nabla K^*(\Sigma^{-1/2}s, \Sigma^{-1/2}v), \mathbb{V}(\nabla^2 K^*(\Sigma^{-1/2}s, \Sigma^{-1/2}v))\right).$$

In particular if there exists constants c, a_d, a_{kl} such that $1 \leq d \leq D$ and $1 \leq k \leq l \leq D$ (with at least one of them being non-zero) such that

$$cK(s, v) + \sum_{d=1}^D a_d \partial_d^s K(s, v) + \sum_{1 \leq k \leq l \leq D} a_{kl} \partial_{kl}^s K(s, v) = 0, \quad (50)$$

then there existing corresponding constants (c^*, a_d^*, a_{kl}^*) (with at least one of them being non-zero) such that

$$\begin{aligned} c^* K^*(\Sigma^{-1/2}s, \Sigma^{-1/2}v) + \sum_{d=1}^D a_d^* \partial_d^s K^*(\Sigma^{-1/2}s, \Sigma^{-1/2}v) \\ + \sum_{1 \leq k \leq l \leq D} a_{kl}^* \partial_{kl}^s K^*(\Sigma^{-1/2}s, \Sigma^{-1/2}v) = 0. \end{aligned} \quad (51)$$

Applying Lemma 2 yields a contradiction and thus establishes the result. \square

D.5 Proof of Proposition 7

Proof. Note that for a SuRF $(\tilde{X}, X, K, \mathcal{V})$ we obtain the following identity

$$\langle \partial_d K_s, K_{s'} \rangle = \text{Cov} \left[\partial_d^s \tilde{X}(s), \tilde{X}(s') \right] = \langle \partial_d^s, 1_{s'} \rangle. \quad (52)$$

Hence the result for a normalized SuRF is a Corollary of Theorem 4. \square

D.6 Proof of Theorem 1

Proof. In order to apply Theorem 12.4.2 from Adler and Taylor [2009] we need to prove that the assumptions **(G1)**-**(G3)** hold. The assumption that \tilde{X}_α is Gaussian with almost surely C^2 -sample paths clearly holds by the assumption that X is a Gaussian field on \mathcal{V} and $K(\cdot, v) \in C^3(\overline{\mathcal{M}})$ for all $v \in \mathcal{V}$. The non-degeneracy condition follows from Proposition 4. The last assumption that there is an $\epsilon > 0$ such that

$$\mathbb{E} \left[\left(\partial_{dd'} \tilde{X}_\alpha(x) - \partial_{dd'} \tilde{X}_\alpha(y) \right)^2 \right] \leq K | \log \|x - y\| |^{-(1+\gamma)}$$

for some $K > 0$, all $d, d' \in \{1, \dots, D\}$ and for the charts $(\overline{U}_\alpha, \overline{\varphi}_\alpha)$, $\alpha \in \{1, \dots, P\}$, in the atlas of $\overline{\mathcal{M}}$ covering \mathcal{M} , all $x, y \in \overline{\varphi}(\overline{U}_\alpha) \cap \mathcal{M}$ such that $|x - y| < \epsilon$ is established in Proposition 3. \square

D.7 Proof of Theorem 6

Computation of $\Theta(x) = \int_{\mathbb{S}(\mathcal{T}_x \partial_1 \mathcal{M}_V^\perp)} \alpha(\nu) \mathcal{H}_1(d\nu)$ for Voxel Manifolds. In order to compute $\Theta(x)$ we need to introduce the normal Morse index $\alpha(\nu)$. We specialize here to the case of \mathcal{M}_V being a voxel manifold embedded into \mathbb{R}^3 , yet the exact same concept is defined for any WS manifold, compare [Adler and Taylor, 2009, Scn 9.2.1].

For any $x \in \mathcal{M}_V$ and any direction $\nu \in \mathbb{S}(\mathcal{T}_x \mathcal{M}_V)$ the normal Morse index is one minus the local Euler characteristic (EC) of the intersection of \mathcal{M}_V , the δ -ball centered at x and the affine plane $\{\lambda \in \mathbb{R}^3 : \lambda^T \nu + x + \epsilon = 0\}$ for $\epsilon > 0$. If δ is sufficiently small, this EC does not depend on ϵ provided that ϵ is small enough. Although this definition sounds complicated at first, it can be easily computed for all x and ν for a voxel manifold. Note that \mathcal{M}_V or more precisely an open neighbourhood of it might be endowed with a different Riemannian metric than the standard Riemannian metric on \mathbb{R}^3 , which in our case is the induced Riemannian metric $\mathbf{\Lambda}$ by a unit-variance random field f . In this case $\nu \in \mathbb{S}(\mathcal{T}_x \mathbb{R}^3)$ are vectors $\nu \in \mathbb{R}^3$ such that $\nu^T \mathbf{\Lambda}(x) \nu = 1$.

In the case that $x \in \partial_3 \mathcal{M}_V$ and $\nu \in \mathbb{S}(\mathcal{T}_x \mathbb{R}^3)$ it is obvious that $\alpha(\nu) = 0$ because the intersection of the affine plain defined by ν and the δ -ball is always homeomorphic to a filled disk, which has EC 1. Similarly, if $x \in \partial_2 \mathcal{M}_V$, then $\alpha(\nu) = 0$ for all $\nu \in \mathbb{S}(\mathcal{T}_x \mathbb{R}^3) \setminus \{\nu_{out}\}$. Here ν_{out} is the unique outside pointing normal (w.r.t. the $\mathbf{\Lambda}$ metric) at $x \in \partial_2 \mathcal{M}_V$ and it holds that $\alpha(\nu_{out}) = 0$ as intersection of the affine plain defined by ν_{out} for a small enough δ -ball is again homeomorphic to a filled disk. The interesting cases happen at the edges of the voxel manifold, i.e., for $x \in \partial_1 \mathcal{M}_V$. Here the behavior of $\alpha(\nu)$ can be classified by the three types of possible edges: the convex, the double convex and the concave edge. These cases are shown in Figure 22 in Appendix B.2.

The behavior of α for directions $\nu \in \mathbb{S}(\mathcal{T}_x \partial_1 \mathcal{M}_V^\perp)$ is demonstrated in Figure 23 within the hyperplane $x + \mathcal{T}_x \partial_1 \mathcal{M}_V^\perp$ with \mathcal{M}_V . Here we show the two possible intersection scenarios of the hyperplane (bold green line) orthogonal to the direction $-\nu \in \mathbb{S}(\mathcal{T}_x \partial_1 \mathcal{M}_V^\perp)$ (green arrow) with a small δ -ball (dotted black line) and the voxel manifold \mathcal{M}_V from the definition of α . In particular, it can be seen that $\alpha(\nu)$ is constant, if $-\nu$ is inside the normal cone $\mathcal{N}_x \mathcal{M}_V$ (for a definition see [Adler and Taylor, 2009, p.189]) and constant on $\mathbb{S}(\mathcal{T}_x \partial_1 \mathcal{M}_V^\perp) \setminus \mathcal{N}_x \mathcal{M}_V$ independent on the type of edge to which x belongs. The geometric embedding of the the intersection of the (geometric) normal cone $x + \mathcal{N}_x \mathcal{M}_V$ with the hyperplane $x + \mathcal{T}_x \partial_1 \mathcal{M}_V^\perp$ is represented by the red shaded areas. From this we deduce that on a convex edge the EC of the intersection of the green hyperplane with the δ -ball and \mathcal{M}_V is 0, if $-\nu \in \mathbb{S}(\mathcal{T}_x \partial_1 \mathcal{M}_V^\perp)$, as the intersection is empty and 1 otherwise because the intersection is homeomorphic to a disk. Similar, it holds that the EC of the intersection is 2 for x on a double convex or concave edge, if $-\nu \in \mathbb{S}(\mathcal{T}_x \partial_1 \mathcal{M}_V^\perp)$, as the intersection is homeomorphic to the disjoint union of two disks and 1 else because the intersection is homeomorphic to a disk. Therefore we obtain that $\alpha(\nu)$ for $\nu \in \mathbb{S}(\mathcal{T}_x \partial_1 \mathcal{M}_V^\perp)$ is given by

$$\alpha(\nu) = \begin{cases} 1, & \text{if } x \text{ on convex edge and } -\nu \in (\mathcal{N}_x \mathcal{M}_V)^\circ \\ -1, & \text{if } x \text{ on a double convex edge and } -\nu \in (\mathcal{N}_x \mathcal{M}_V)^\circ \\ -1, & \text{if } x \text{ on concave edge and } -\nu \in (\mathcal{N}_x \mathcal{M}_V)^\circ \\ 0, & \text{else} \end{cases} . \quad (53)$$

Using this we can compute the function $\Theta(x)$.

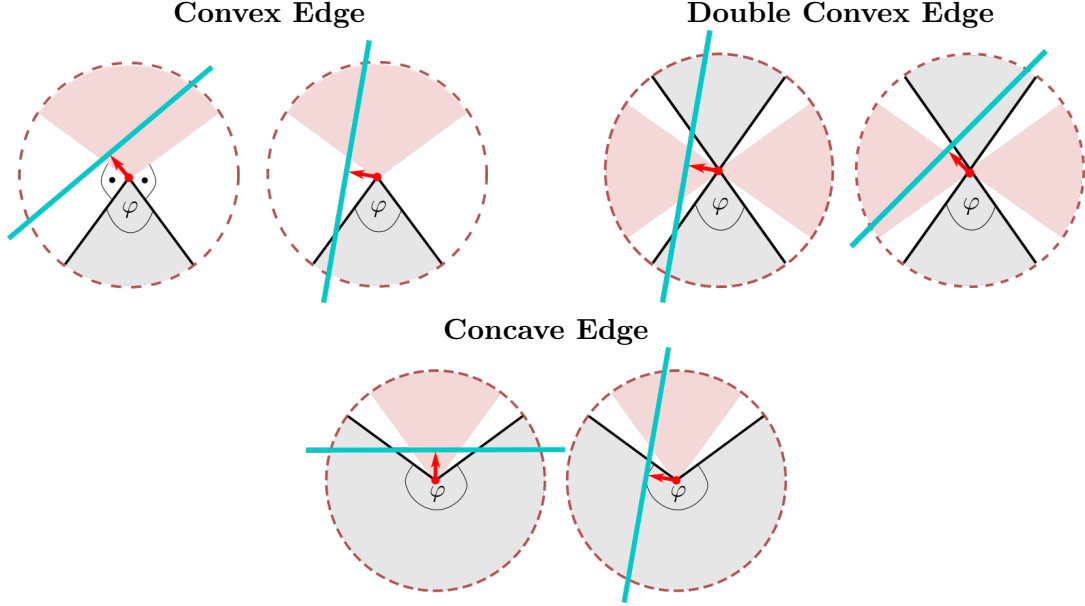


Figure 23: The two different scenarios of intersections of the hyperplane at the three different types of edges appearing in a voxel manifold \mathcal{M}_V illustrated within the hyperplane $x + \mathcal{T}_x \partial_1 \mathcal{M}_V^\perp$. The dashed red line is the boundary of an δ -ball centered at x . The grey shaded area belongs to \mathcal{M}_V and the red shaded area is the (geometric) normal cone $x + \mathcal{N}_x \mathcal{M}_V$ which needs to be orthogonal to the boundary of \mathcal{M}_V in $x + \mathcal{T}_x \partial_1 \mathcal{M}_V^\perp$. The fact that the opening angles φ are not necessarily in $\{\pi/2, 3\pi/2\}$ appear as $x + \mathcal{T}_x \partial_1 \mathcal{M}_V^\perp$ is not orthogonal to the edge x belongs to. The red arrow is the unit direction $-\nu \in \mathbb{S}(\mathcal{T}_x \partial_1 \mathcal{M}_V^\perp)$ scaled by ϵ and the turquoise line is the hyperplane defined by $-\nu$.

Lemma 3. Let \mathcal{M}_V be a voxel manifold, $x \in \partial_1 \mathcal{M}_V$ and U_x, V_x, W_x denote an ON frame for $\mathcal{T}_x \overline{\mathcal{M}_V}$. Define $M = V_x \times W_x = (m_1(x), m_2(x), m_3(x))^T$. Define

$$\beta(x) = \arccos \left(\frac{m_2(x)m_3(x)}{\sqrt{m_2^2(x) + m_1^2(x)}\sqrt{m_3^2(x) + m_1^2(x)}} \right).$$

Then we obtain

$$\Theta(x) = \begin{cases} \pi - \beta(x), & \text{if } x \text{ belongs to a convex edge} \\ -2\beta(x), & \text{if } x \text{ belongs to a double convex edge} \\ \beta(x) - \pi, & \text{if } x \text{ belongs to a concave edge} \end{cases}.$$

Proof. Let $\beta(x)$ be the minimum of φ and $2\pi - \varphi$ where ϕ is the opening angle within \mathcal{M}_V from Figure 23. This yields

$$\begin{aligned} \int_{\mathbb{S}(\mathcal{T}_x \partial_1 \mathcal{M}_V^\perp)} \alpha(\nu_2) \mathcal{H}_1(d\nu_2) &= \int_0^{2\pi} \mathbb{1}_{-\sin(t)E_1 - \cos(t)E_2 \in (\mathcal{N}_x \mathcal{M}_V)^\circ} dt \\ &= \begin{cases} \pi - \beta(x), & \text{if } x \text{ on a convex edge} \\ -2\beta(x), & \text{if } x \text{ on a double convex edge} \\ \beta(x) - \pi, & \text{if } x \text{ on a concave edge} \end{cases}, \end{aligned}$$

because the characteristic function is only 1, if $-\nu$ belongs to the normal cone and hence the integral is equal to the opening angle of the normal cone (red shaded area in Fig. 23).

It remains to compute the angle $\beta(x)$ which is obtained by computing the angle between the intersection of the affine plane $x + \mathcal{T}_x \partial_1 \mathcal{M}_V^\perp$ and the boundary of \mathcal{M}_V at x . We only treat the case of $x \in \mathcal{M}_V$ lying on a convex edge. Double convex and concave edges follow analogously. Since the tangent space and \mathbb{R}^3 can be identified we assume w.l.o.g. that $x = 0$ and the voxel is given by the set $\{y \in \mathbb{R}^3 : y_3 \leq 0, y_2 \leq 0\}$. (note we extend the edge infinitely, which does not make a difference in this argument) Its boundary is given by the set $A \cup B = \{y \in \mathbb{R}^3 : y_3 = 0, y_2 \leq 0\} \cup \{y \in \mathbb{R}^3 : y_3 \leq 0, y_2 = 0\}$. The edge to which x belongs is given by $E = \{y \in \mathbb{R}^3 : y_3 = 0, y_2 = 0\}$. An orthonormal basis at x with U_x spanning $\mathcal{T}_x E$ is given in Proposition 14. The plane in which the unit circle $\mathbb{S}^1(\mathcal{T}_x E^\perp)$ lies is given by the linear span of V_x, W_x , which we denote by $\mathcal{F} = \{y \in \mathbb{R}^3 : m_1(x)y_1 + m_2(x)y_2 + m_3(x)y_3 = 0\}$ for some $m_1(x), m_2(x), m_3(x) \in \mathbb{R}$. The intersection $\mathcal{F} \cap A$ and $\mathcal{F} \cap B$ are given by

$$\begin{aligned} A \cap \mathcal{F} &= \{y \in \mathbb{R}^3 : m_1(x)y_1 + m_2(x)y_2 = 0 \wedge y_2 \leq 0 \wedge y_3 = 0\} \\ B \cap \mathcal{F} &= \{y \in \mathbb{R}^3 : m_1(x)y_1 + m_3(x)y_3 = 0 \wedge y_3 \leq 0 \wedge y_2 = 0\} \end{aligned} \quad (54)$$

By construction $m_1(x) \neq 0$, since otherwise $\mathcal{F} \cap A = \mathcal{F} \cap B = E$ and hence V, W cannot be both orthogonal to E which contradicts the assumption that U_x, V_x, W_x form an orthonormal basis for $\mathcal{T}_x \mathcal{M}_V$. Thus, if $m_1(x) \neq 0$ we have that $(m_2(x)/m_1(x), -1, 0)$ and $(m_3(x)/m_1(x), 0, -1)$ are vectors in the intersection, which we can identify with tangent directions along E . Thus,

$$\begin{aligned} \varphi &= \arccos \left(\frac{\frac{m_2(x)m_3(x)}{m_1^2(x)}}{\sqrt{\frac{m_2^2(x)}{m_1^2(x)} + 1} \sqrt{\frac{m_3^2(x)}{m_1^2(x)} + 1}} \right) \\ &= \arccos \left(\frac{m_2(x)m_3(x)}{\sqrt{m_2^2(x) + m_1^2(x)} \sqrt{m_3^2(x) + m_1^2(x)}} \right). \end{aligned} \quad (55)$$

The same formula holds true if $m_1(x) = 0$ and $m_2(x) \neq 0$ and $m_3(x) \neq 0$. \square

Computation of $\int_{\partial_2 M} \mathbf{\Lambda}_x (\bar{\nabla}_{U_x} U_x + \bar{\nabla}_{V_x} V_x, N_x) \mathcal{H}_2(dx)$ for Voxel Manifolds Assume w.l.o.g. that $\mathcal{T}_x \mathcal{M}_V$ for $x \in \partial_2 \mathcal{M}_V$ is contained in the x_1 - x_2 -plane. An orthonormal frame is given by U_x, V_x, W_x from (14) and by construction $N_x = \pm W_x$, where the sign depends on whether W_x is inward or outward pointing. Using the coordinate representations $U_x = \sum_{d=1}^3 U_d(x) \partial_d$ and $V_x = \sum_{d=1}^3 V_d(x) \partial_d$, linearity and product rule for the covariant derivative and formula (34), we obtain

$$\begin{aligned} \mathbf{\Lambda}_x (\bar{\nabla}_{U_x} U_x, N_x) &= N_x^T \mathbf{\Lambda}(x) U_1(x) \begin{pmatrix} \partial_1 U_1(x) \\ 0 \\ 0 \end{pmatrix} + U_1^2(x) N_x^T \begin{pmatrix} \Gamma_{111}(x) \\ \Gamma_{112}(x) \\ \Gamma_{113}(x) \end{pmatrix} \\ &= U_1^2(x) N_x^T \begin{pmatrix} \Gamma_{111}(x) \\ \Gamma_{112}(x) \\ \Gamma_{113}(x) \end{pmatrix}. \end{aligned}$$

Here the second equality is due to the fact that $N_x \propto \mathbf{\Lambda}^{-1}E_3$, if represented as a vector. Similarly it holds that

$$\begin{aligned} \mathbf{\Lambda}_x(\bar{\nabla}_{V_x} V_x, N_x) &= V_1^2(x) N_x^T \begin{pmatrix} \Gamma_{111}(x) \\ \Gamma_{112}(x) \\ \Gamma_{113}(x) \end{pmatrix} + V_2^2(x) N_x^T \begin{pmatrix} \Gamma_{221}(x) \\ \Gamma_{222}(x) \\ \Gamma_{223}(x) \end{pmatrix} \\ &\quad + V_1(x) V_2(x) N_x^T \begin{pmatrix} \Gamma_{121}(x) \\ \Gamma_{122}(x) \\ \Gamma_{123}(x) \end{pmatrix} \end{aligned}$$

Summarizing this yields the following proposition about the trace of the shape operator along $\partial_2 \mathcal{M}_\mathcal{V}$, i.e., $\bar{g}(\bar{\nabla}_{U_x} U_x + \bar{\nabla}_{V_x} V_x, N_x)$.

Proposition 9. *Let $\mathcal{M}_\mathcal{V}$ be a voxel manifold and assume that $x \in \partial_2 \mathcal{M}_\mathcal{V}$ such that $\mathcal{T}_x \partial_2 \mathcal{M}_\mathcal{V}$ is spanned by E_k, E_l . Then*

$$\begin{aligned} \mathbf{\Lambda}_x(\bar{\nabla}_{U_x} U_x + \bar{\nabla}_{V_x} V_x, N_x) &= (U_k^2(x) + V_k^2) N_x^T \begin{pmatrix} \Gamma_{kk1}(x) \\ \Gamma_{kk2}(x) \\ \Gamma_{kk3}(x) \end{pmatrix} + V_l^2(x) N_x^T \begin{pmatrix} \Gamma_{ll1}(x) \\ \Gamma_{ll2}(x) \\ \Gamma_{ll3}(x) \end{pmatrix} \\ &\quad + V_k(x) V_l(x) N_x^T \begin{pmatrix} \Gamma_{kl1}(x) \\ \Gamma_{kl2}(x) \\ \Gamma_{kl3}(x) \end{pmatrix} \end{aligned}$$

D.8 Proof of Theorem 2

We prove this result in more generality as the restriction to SuRFs is not necessary. The proof extends that of [Taylor and Worsley \[2007\]](#) which established the result for the trivial linear model. To do so assume that $Y_1, \dots, Y_N \sim Y$ is an iid sample of Gaussian random fields on a voxel manifold $\mathcal{M}_\mathcal{V}$. We restrict here to voxel manifolds to avoid working in a chart, however, the proof easily generalizes. This sample we represent as the vector $\mathbf{Y} = (Y_1, \dots, Y_N)^T$ and therefore the corresponding estimator generalizing (15) is, for $x \in \mathcal{M}_\mathcal{V}$,

$$\begin{aligned} \hat{\Lambda}_{dd'}(x) &= \frac{\text{Cov}[\partial_d \mathbf{Y}(x), \partial_{d'} \mathbf{Y}(x)]}{\text{Var}[\mathbf{Y}(x)]} \\ &= \text{Cov} \left[\partial_d \left(\frac{\mathbf{Y}(x)}{\sqrt{\text{Var}[\mathbf{Y}(x)]}} \right), \partial_{d'} \left(\frac{\mathbf{Y}(x)}{\sqrt{\text{Var}[\mathbf{Y}(x)]}} \right) \right] \\ &\quad - \frac{\text{Cov}[\partial_d \mathbf{Y}(x), \mathbf{Y}(x)] \text{Cov}[\mathbf{Y}(x), \partial_{d'} \mathbf{Y}(x)]}{\text{Var}[\mathbf{Y}(x)]^2}. \end{aligned} \tag{56}$$

Here as in the main manuscript the operation $\text{Var}[\cdot]$ and $\text{Cov}[\cdot, \cdot]$ denote the sample variance and sample covariance respectively. We define the vector of normalized residuals to be $\mathbf{R}(x) = \frac{\mathbf{H}\mathbf{Y}(x)}{\|\mathbf{H}\mathbf{Y}(x)\|}$, $x \in \mathcal{M}_\mathcal{V}$, where $\|\cdot\|$ denotes the Euclidean norm and $\mathbf{H} = I_{N \times N} - \mathbf{1}\mathbf{1}^T$ with $\mathbf{1}^T = (1, \dots, 1) \in \mathbb{R}^N$, is the centering matrix. Note that \mathbf{R} does not depend on the (unknown) variance $\text{Var}[Y]$ as for the sample $\tilde{\mathbf{Y}} = \mathbf{Y}/\sqrt{\text{Var}[Y]}$ we have that $\tilde{\mathbf{R}}(x) = \mathbf{R}(x)$ for all $x \in \mathcal{M}_\mathcal{V}$. Thus, using

$$\nabla \mathbf{X}(x) = \begin{pmatrix} \frac{\partial X_1}{\partial x_1}(x) & \dots & \frac{\partial X_1}{\partial x_D}(x) \\ \vdots & \ddots & \vdots \\ \frac{\partial X_D}{\partial x_1}(x) & \dots & \frac{\partial X_D}{\partial x_D}(x) \end{pmatrix}$$

for $\mathbf{X} = (X_1, \dots, X_D)^T \in C(\mathcal{M}_\nu, \mathbb{R}^D)$, we can rewrite (56) in matrix terms as

$$\hat{\mathbf{\Lambda}} = (\nabla \mathbf{R})^T \nabla \mathbf{R}.$$

Recall that the true underlying $\mathbf{\Lambda}$ is given by

$$\mathbf{\Lambda} = \mathbb{E} \left[\left(\nabla \left(\frac{Y - \mathbb{E}[Y]}{\sqrt{\text{Var}[Y]}} \right) \right)^T \nabla \left(\frac{Y - \mathbb{E}[Y]}{\sqrt{\text{Var}[Y]}} \right) \right] = \mathbb{E} \left[(\nabla \tilde{Y}^T) \nabla \tilde{Y} \right],$$

where $\tilde{Y} = \frac{Y}{\sqrt{\text{Var}[Y]}}$. Using this we obtain the following lemma which the proof of which follows the corresponding proof in Taylor and Worsley [2007].

Lemma 4. *Under the assumption and notation described above, we have that*

$$\mathbb{E} \left[\sqrt{\det(\hat{\mathbf{\Lambda}}(x))} \right] = \sqrt{\det(\mathbf{\Lambda}(x))} \quad (57)$$

Proof. \mathbf{H} is a projection matrix and so $\mathbf{H}\mathbf{H} = \mathbf{H}$ and $\mathbf{H}^T = \mathbf{H}$. We can expand $\nabla \mathbf{R}$ in terms of $\tilde{\mathbf{Y}}$ as follows:

$$\nabla \mathbf{R} = \frac{\nabla \mathbf{H} \tilde{\mathbf{Y}}}{\|\mathbf{H} \tilde{\mathbf{Y}}\|} - \frac{\mathbf{H} \tilde{\mathbf{Y}} \nabla((\mathbf{H} \tilde{\mathbf{Y}})^T \mathbf{H} \tilde{\mathbf{Y}})}{2\|\mathbf{H} \tilde{\mathbf{Y}}\|^3} = \left(I_{N \times N} - \frac{\mathbf{H} \tilde{\mathbf{Y}} (\mathbf{H} \tilde{\mathbf{Y}})^T}{\|\mathbf{H} \tilde{\mathbf{Y}}\|^2} \right) \frac{\mathbf{H} \nabla \tilde{\mathbf{Y}}}{\|\mathbf{H} \tilde{\mathbf{Y}}\|}.$$

Now note that

$$\mathbf{H} \left(I_{N \times N} - \frac{\mathbf{H} \tilde{\mathbf{Y}} (\mathbf{H} \tilde{\mathbf{Y}})^T}{\|\mathbf{H} \tilde{\mathbf{Y}}\|^2} \right) \mathbf{H} = \mathbf{H} - \frac{\mathbf{H} \tilde{\mathbf{Y}} (\mathbf{H} \tilde{\mathbf{Y}})^T}{\|\mathbf{H} \tilde{\mathbf{Y}}\|^2}$$

and therefore it is idempotent with

$$\text{tr} \left(\mathbf{H} - \frac{\mathbf{H} \tilde{\mathbf{Y}} (\mathbf{H} \tilde{\mathbf{Y}})^T}{\|\mathbf{H} \tilde{\mathbf{Y}}\|^2} \right) = \text{tr}(\mathbf{H}) - 1$$

Thus, applying Cochran's Theorem [Mardia et al., 1979, Theorem 3.4.4], it follows that for all $x \in \mathcal{S}$,

$$(\nabla \mathbf{R}(x))^T \nabla \mathbf{R}(x) \mid \tilde{\mathbf{Y}}(x) \sim \text{Wish}_D(\mathbf{\Lambda} \|\mathbf{H} \tilde{\mathbf{Y}}\|^{-2}, \text{tr}(\mathbf{H}) - 1).$$

As such by [Mardia et al., 1979, Corollary 3.4.1.2]

$$\begin{aligned} \mathbf{W}(x) &\sim \|\mathbf{H} \tilde{\mathbf{Y}}\|^2 \mathbf{\Lambda}(x)^{-1/2} (\nabla \mathbf{R}(x))^T \nabla \mathbf{R}(x) \mathbf{\Lambda}(x)^{-1/2} \mid \tilde{\mathbf{Y}}(x) \\ &\sim \text{Wish}_D(I_{N \times N}, \text{tr}(\mathbf{H}) - 1) \end{aligned}$$

Taking determinants and rearranging it follows that, unconditionally,

$$\sqrt{\det((\nabla \mathbf{R}(x))^T \nabla \mathbf{R}(x))} \sim \sqrt{\det(\mathbf{\Lambda}(x)) \det(\mathbf{W}(x)) V(x)^{-D}},$$

where $\mathbf{W}(x)$ is independent of $V(x) = \|\mathbf{H} \tilde{\mathbf{Y}}\|^2 \sim \chi_{\text{tr}(\mathbf{H})}^2$. From the independence, the formula for the moments of χ^2 -distributions and Theorem 3.4.8 from Mardia et al. [1979] we obtain

$$\begin{aligned} \mathbb{E} \left[\sqrt{\det((\nabla \mathbf{R}(x))^T \nabla \mathbf{R}(x))} \right] &= \sqrt{\det(\mathbf{\Lambda}(x))} \mathbb{E} \left[\sqrt{\det(\mathbf{W}(x))} \right] \\ \mathbb{E} \left[V(x)^{-\frac{D}{2}} \right] &= \det(\mathbf{\Lambda}(x))^{1/2}. \end{aligned}$$

□

Remark 13. Lemma 4 also holds for estimates of $\mathbf{\Lambda}$ in a linear model, compare Taylor and Worsley [2007]. This follows by a similar proof as, in that setting, the residuals \mathbf{R} which are used to calculate $\hat{\mathbf{\Lambda}}$ are obtained by $\mathbf{R} = \mathbf{P}\mathbf{Y}$, where \mathbf{P} is idempotent.

Proof of Theorem 2. In what follows we establish the results for $\hat{\mathcal{L}}_D^{(r)}$. The proof for $\hat{\mathcal{L}}_{D-1}^{(r)}$ is identical as each $\mathbf{\Lambda}^I$ is a $(D-1) \times (D-1)$ -submatrix of $\mathbf{\Lambda}$.

Using Lemma 4 and the approximation of integrals of continuous functions by Riemann sums yields

$$\begin{aligned} \lim_{r \rightarrow \infty} \mathbb{E} \left[\hat{\mathcal{L}}_D^{(r)} \right] &= \lim_{r \rightarrow \infty} \mathbb{E} \left[\sum_{x \in \mathcal{M}_{\mathcal{V}}^{(r)}} \sqrt{\det(\hat{\mathbf{\Lambda}}(x))} \prod_{d=1}^D \frac{\delta_d}{r+1} \right] \\ &= \lim_{r \rightarrow \infty} \sum_{x \in \mathcal{M}_{\mathcal{V}}^{(r)}} \mathbb{E} \left[\sqrt{\det(\hat{\mathbf{\Lambda}}(x))} \right] \prod_{d=1}^D \frac{\delta_d}{r+1} \\ &= \lim_{r \rightarrow \infty} \sum_{x \in \mathcal{M}_{\mathcal{V}}^{(r)}} \sqrt{\det(\mathbf{\Lambda}(x))} \prod_{d=1}^D \frac{\delta_d}{r+1} \\ &= \int_{\mathcal{M}_{\mathcal{V}}} \sqrt{\det(\mathbf{\Lambda}(x))} dx = \mathcal{L}_D \end{aligned}$$

Similarly, using Fubini's theorem which is applicable as $\mathcal{M}_{\mathcal{V}}$ is compact, we obtain that

$$\begin{aligned} \mathbb{E} \left[\lim_{r \rightarrow \infty} \hat{\mathcal{L}}_D^{(r)} \right] &= \mathbb{E} \left[\int_{\mathcal{M}_{\mathcal{V}}} \sqrt{\det(\hat{\mathbf{\Lambda}}(x))} dx \right] \\ &= \int_{\mathcal{M}_{\mathcal{V}}} \mathbb{E} \left[\sqrt{\det(\hat{\mathbf{\Lambda}}(x))} \right] dx \\ &= \int_{\mathcal{M}_{\mathcal{V}}} \sqrt{\det(\mathbf{\Lambda}(x))} dx = \mathcal{L}_D \end{aligned}$$

□

D.9 Proof of Theorem 3

Proof. By the assumptions and Proposition 2 the SuRF has almost surely L^2 -Hölder continuous paths and therefore the assumptions of Lemma 11 from Telschow and Schwartzman [2022] are satisfied. This means that $\hat{\mathbf{\Lambda}}$ converges uniformly almost surely to $\mathbf{\Lambda}$ over all $x \in \overline{\mathcal{M}_{\mathcal{V}}}$. Since the Riemann sum converges to the integral the $\lim_{r \rightarrow \infty} \lim_{N \rightarrow \infty}$ statement follows immediately. On the other hand the $\lim_{N \rightarrow \infty} \lim_{r \rightarrow \infty}$ statement is a special case of Theorem 3 from Telschow et al. [2023] since for \mathcal{L}_2 and \mathcal{L}_3 from their condition **(R)** only the uniform almost sure convergence of $\hat{\mathbf{\Lambda}}$ to $\mathbf{\Lambda}$ is required. □